

COMPUTATIONAL FRAMEWORK FOR STUDYING SEISMICITY
INDUCED BY ROCK ENGINEERING ACTIVITIES

By

Zoheir Khademian

Copyright by Zoheir Khademian 2018

All Rights Reserved

A thesis submitted to the Faculty and the Board of Trustees of the Colorado School of Mines in partial fulfillment of the requirements for the degree of Doctor of Philosophy (Mining and Earth Systems Engineering)

Golden, Colorado

Date -----

Signed: _____

Zoheir Khademian

Signed: _____

Dr. Masami Nakagawa

Thesis Advisor

Signed: _____

Dr. Ugur Ozbay

Thesis Co-advisor

Golden, Colorado

Date -----

Signed: _____

Dr. Priscilla Nelson

Department Head of Mining Engineering

ABSTRACT

Rock Engineering Activities (REA), including tunneling, shaft-boring, mining, deep wastewater disposal, and geothermal energy extraction may result in unstable compressive failure of rock and unstable shear slip on pre-existing discontinuities within the affected zone. The unstable compressive failure is the violent crushing of rocks and unstable shear slip is rapid sliding on pre-existing discontinuity. Unstable failure may result in seismic events characterized by significant radiation of seismic energy. This dissertation presents a computational framework that includes methodologies, modeling approaches, and techniques for identifying the occurrence of unstable failures and estimating magnitudes of induced seismic events. The concept of failure instability, mostly developed in mining engineering, is advanced into numerical methodologies for studying seismicity in different REA. A Universal Distinct Element Code (UDEC) is used to develop the framework and exemplify its application in minimizing the intensity of potential seismic events induced by REA. For assessing the intensity of induced events, two methods are introduced for estimating radiated seismic energy: one compares the state of energy before and after an unstable failure; the other calculates energy that needs to be radiated for reaching static equilibrium.

Induced seismicity in tunneling and shaft-boring settings is explored by modeling circular excavations advancing next to a normal fault in a stressed brittle rock. A single pillar supporting a tabular excavation and a strike-slip fault are modeled to study mining-induced seismicity. The application of the developed framework for studying natural earthquakes is discussed by quantifying relationships between source parameters of an earthquake rupture and then checking results against analytical solutions and globally recorded seismic data. The framework is extended to study seismicity induced by injecting fluid onto deep fault planes, a simplified analogy to wastewater disposal and geothermal energy extraction activities. Effects of injection pressure increments on the intensity of induced seismic events are analyzed to show the framework application in finding strategies to minimize seismic hazards. The calibrated framework and verified results allow for assessing potential seismicity induced by different REA in complex geological settings and adjusting design parameters to reduce the intensity of these events.

TABLE OF CONTENTS

ABSTRACT.....	iii
LIST OF FIGURES.	viii
LIST OF TABLES.....	xii
ACKNOWLEDGEMENT.	xiii
CHAPTER 1 INTRODUCTION.	1
1.1 Introduction.....	1
1.2 Background.....	1
1.2.1 Seismicity Induced by Mining.....	2
1.2.2 Seismicity Induced by Tunneling.	3
1.2.3 Seismicity Induced by Hydraulic Fracturing.	4
1.2.4 Seismicity Induced by Deep Wastewater Disposal.....	6
1.2.5 Seismicity Induced by Geothermal Systems.....	8
1.3 Mechanisms of Unstable Failures	9
1.3.1 Instability of Slip Failure	10
1.3.2 Instability of Compressive Failure	12
1.4 Modeling in UDEC	14
1.4.1 Continuously Yielding Joint Model	15
1.4.2 Mohr-Coloumb Strain Softening Constitutive Law	16
1.5 Thesis Organization	17
1.6 References	19
CHAPTER 2 MODELING UNSTABLE ROCK FAILURES IN TUNNELING AND SHAFT BORING BASED ON ENERGY BALANCE CALCULATIONS.....	23
2.1 Abstract.....	23
2.2 Introduction.....	24
2.3 Methodology.....	25
2.3.1 Circular Opening in an Infinite Medium.	26
2.3.2 Circular Opening in Finite Elastic Medium.....	28

2.3.3	Tabular Excavation.....	29
2.3.4	Effects of Excavation Speed.....	30
2.3.5	Introducing <i>Inelastic Energy Term</i>	31
2.4	Concept of Compressive-type Unstable Failure.....	31
2.5	Concept of Shear-type Unstable Failure.....	34
2.6	Circular Opening in a Brittle Rock.....	37
2.6.1	Compressive-type Unstable Failure and <i>k Ratio</i>	37
2.6.2	Compressive-type Unstable Failure and Loading System Stiffness.....	39
2.7	Circular Opening Advancing Next to a Slip-weakening Fault.....	40
2.7.1	Shear-type Unstable Failure and <i>k Ratio</i>	41
2.7.2	Shear-type Unstable Failure and Loading System Stiffness.....	43
2.8	Discussion.....	44
2.9	Conclusions.....	45
2.9	References.....	46
CHAPTER 3	MODELING ROCK BURST IN SHEAR AND COMPRESSION THROUGH SEISMIC ENERGY CALCULATION.....	48
3.1	Abstract.....	48
3.2	Introduction.....	48
3.2.1	Compressive-type Rock burst.....	49
3.2.2	Shear-type rock burst.....	50
3.3	Energy Balance.....	52
3.4	Violent Compressive Failures.....	53
3.4.1	Brittle, Semi-brittle, and Ductile Model Responses.....	54
3.4.2	Loading System Stiffness.....	56
3.5	Violent Shear Failures.....	58
3.5.1	Fault Slip Model.....	58
3.5.2	Modeling Rupture along Strike-Slip Fault.....	61
3.6	Discussion.....	66

3.7	Conclusions.....	67
3.8	References.....	68
CHAPTER 4	MODELING EARTHQUAKE RUPTURE PROPAGATION BASED ON CALCULATION OF ENERGY COMPONENTS.....	70
4.1	Abstract.....	70
4.2	Introduction.....	70
4.3	Rock Mass Energy Components.....	74
4.4	Physics of Rupture.....	76
4.4.1	Idealized Model of Rupture.....	76
4.4.1.1	Slip-Weakening Behaviors and Loading System Stiffness.....	78
4.4.2	Calibration of Dynamic Rupture Model.....	81
4.4.2.1	Calibrating Loading Conditions and Mesh Sizes.....	81
4.4.2.2	Calibrating Damping Constant.....	85
4.5	Parametric Studies.....	86
4.5.1	Characteristics Distance.....	87
4.5.2	Loading System Stiffness.....	89
4.6	Discussion.....	90
4.7	Conclusions.....	91
4.8	References.....	92
CHAPTER 5	MODELING INJECTION-INDUCED SEISMICITY THROUGH CALCULATION OF RADIATED SEISMIC ENERGY.....	95
5.1	Abstract.....	95
5.2	Introduction.....	96
5.3	Methodology.....	99
5.3.1	Balance of Energy Transfer.....	99
5.3.2	Calibrating Dynamic Rupture Model.....	100
5.3.3	Energetics of Rupture.....	104
5.4	Modeling Injection-Induced Rupture.....	105

5.4.1	Well-oriented Faults.	107
5.4.2	Misoriented Faults.	109
5.5	Seismic Moment and Radiated Seismic Energy.	111
5.6	Discussion.	112
5.7	Conclusions.	114
5.8	References.	114
CHAPTER 6	GENERAL CONCLUSION.	118
6.1	Research Originality.	118
6.2	Summary of Accomplishments.	119
6.3	Future Research.	120
APPENDIX A	SUPPLEMENTAL ELECTRONIC FILES FOR CHAPTER 2.	124
APPENDIX B	SUPPLEMENTAL ELECTRONIC FILES FOR CHAPTER 3.	127
APPENDIX C	EQUATIONS FOR MECHANICAL DAMPING IN UDEC.	131
APPENDIX D	SUPPLEMENTAL ELECTRONIC FILES FOR CHAPTER 4.	132
APPENDIX E	SUPPLEMENTAL ELECTRONIC FILES FOR CHAPTER 5.	136
APPENDIX F	PUBLISHER COPYRIGHT PERMISSION FOR CHAPTER 5.	142

LIST of FIGURES

Figure 1.1	Schematics of seismicity induced by wastewater disposal: a) wastewater injection in the vicinity of a pre-existing fault oriented in the favor of slip with respect to the tectonic loadings; b) reactivated fault as a result of the stress disturbance caused by injection process.	6
Figure 1.2	The mass-spring loading system where the mass is pulled by a spring over the surface. (a) The mass-spring system before starting the velocity loading and developing F within the spring. (b) The mass is loaded to the point of failure. The spring is elongated and frictional force F_s is developed on the interface. This figure corresponds to the state of loading system at point A in Figure 1.3a. (c) The slip is initiated and spring is once again unloaded, representative of the loading system at point B in Figure 1.3a.	10
Figure 1.3	Conceptual model of loading system and failure in compression. The specimen is loaded by a compressive force applied through a spring. (a) specimen and spring before loading. (b) Loaded specimen at the onset of failure. (c) failed specimen and elongated spring.	11
Figure 1.4	Conceptual model of loading system and failure in compression. The specimen is loaded by a compressive force applied through a spring. (a) Specimen and spring system before loading. (b) Loaded specimen at the onset of failure. (c) Failed specimen and elongated spring.	12
Figure 1.5	Concept of instability in compression (after Salamon (1970) with modification): (a) typical compressive force-displacement curve and the spring load line with stiffness k_1 . The blue dashed lines signify the force imbalance between points A and B; (b) the conceptual role of spring stiffness in instability of a compressive failure. The dashed black lines show spring with stiffness values of $k_1 < k_2 < k_3$. Points A and B on each figure correspond to Figures 1.3b and 1.3c, respectively.	13
Figure 1.6	Simplified softening parameters used in this study. Cohesion is reduced from 1.7 Mpa to zero. Friction angle is kept constant at 20 degree.	13
Figure 2.1	Model boundaries for simulating a circular opening in an infinite medium.	27
Figure 2.2	Circular opening in a finite elastic medium.	28
Figure 2.3	Modeling configuration of a tabular opening in an elastic medium.	29
Figure 2.4	Single pillar numerical model and loading conditions.	32
Figure 2.5	Pillar stress-displacement curves and Ground Reaction Curve.	33
Figure 2.6	Numerical model for the direct shear test.	35
Figure 2.7	Discontinuity shear stress-slip curves and GRCs.	35
Figure 2.8	Variations between radiated seismic energy, k ratio and dimension of excavation into semi-brittle rock.	38

Figure 2.9	Number of failed elements as function of k ratio and radius of excavations in semi-brittle rock.	38
Figure 2.10	Variations between loading system stiffness and radiated seismic energy in excavation in semi-brittle rock.	39
Figure 2.11	Failure zone expansions as function of loading system stiffness for excavations in semi-brittle rock.	40
Figure 2.12	Zoom-in view of the circular excavation of radius 2 m next to the fault.	41
Figure 2.13	Relation between the radiated seismic energy, excavation radius and K ratio for a tunnel next to a brittle fault.	42
Figure 2.14	Variation of the rupture length along the fault with the k ratio and excavation size.	42
Figure 2.15	Relationships between radiated seismic energy, excavation radius and Young's modulus when excavating an opening next to a slip-weakening fault.	43
Figure 2.16	Variations between loading system stiffness and the length of rupture triggered by a circular excavation.	44
Figure 3.1	Schematic view of the tabular excavation with the pillar and mining slices in UDEC. The radius of the circular external boundary is 200 m. The pillar is 0.2 m high and 0.2 m wide.	54
Figure 3.2	Stress-convergence or failure curves for ductile (red curve), semi-brittle (gray curve), and brittle (black curve) behaviors of the pillar. The dashed line is the GRC for the brittle and semi-brittle responses. The GRC for the ductile failure follows the ductile failure curve.	55
Figure 3.3	Graphical and numerical calculations of the seismic energy radiated due to three different pillar responses.	56
Figure 3.4	Parametric study on the effects of the loading system stiffness on the magnitude of the radiated seismic energy from the semi-brittle pillar failure.	57
Figure 3.5	Comparison between graphical and numerical calculations of the seismic energy radiated from compressive failures of the mining pillar under three different loading stiffness values.	58
Figure 3.6	Left: Numerical model of the direct shear test in UDEC. Right: Behavior of the discontinuity and loading systems during the slip in the direct shear test. The solid line is the contact shear stress-displacement response recorded at contact A, the dashed blue curve is the GRC of the stiff system with $E=40$ GPa, and the dashed black line is the soft GRC with $E= 10$ GPa.	59
Figure 3.7	2-D numerical model geometry and initial conditions on the schematic plan view of the fault.	62
Figure 3.8	Frictional properties assigned to each element along the fault for simulating the brittle response.	63

Figure 3.9	Comparison between the analytical and numerical solutions for: (a) driving ESS profile; (b) slip profile along a strike-slip fault with zero D_c ; (c) Continuous deformation parallel to the fault before slip; (d) Discontinuous horizontal displacement after slip.	64
Figure 4.1	Schematic of rupture mechanics: (a) Model geometry for the direct shear test; (b) Schematic representation of the block deformation just before rupture; (c) Post-rupture state and transfer of energy.....	78
Figure 4.2	Responses of discontinuity and block matrix to the loading process in four direct shear tests: (a) stress-slip curves and GRCs for responses with zero and infinite characteristic distances. The interface shear and normal stiffnesses are assumed 50 MPa/mm; (b) stress-slip curves and GRCs for the softer system with $G=4$ GPa and stiffer system with $G=16$ GPa. The interface roughness is 0.1 mm.....	80
Figure 4.3	Numerical model geometry and initial conditions in a plan view of the vertical strike-slip fault.	83
Figure 4.4	Comparison between analytical and numerical solutions for: (a) driving ESS profile; (b) Analytical and numerical solutions for slip.....	84
Figure 4.5	Spatial and temporal distribution of: (a) the rupture propagation; (b) energy radiation along the strike-slip fault for a fraction of the rupture duration.....	86
Figure 4.6	Sensitivity of radiated energy and maximum slip to the damping constant.	87
Figure 4.7	Role of D_c in rupture characteristics: (a) Shear stress versus slip curves recorded at the center of the rupture plane for responses with different D_c ; (b) Role of D_c in radiated seismic energy, slip, and rupture length.....	89
Figure 4.8	Role of rock rigidity in: (a) slip and GRC recorded at the fault center; (b) rupture length, average slip, seismic moment, and seismic energy.....	91
Figure 5.1	Maximum magnitudes of seismic events related to different fluid injection settings (BC Oil and Gas Commission, 2012; Cladouhos et al., 2010; Frohlich et al., 2008; Keranen et al., 2013; Ernest L. Majer et al., 2007; McClure and Horne, 2014; McGarr, 2014; Richards et al., 1994; Shapiro et al., 2007).....	97
Figure 5.2	Schematic plan view of the strike-slip fault model domain with initial and boundary conditions. Blue arrows represent the pressurized domain along the 200 m length of the fault.	103
Figure 5.3	Frictional properties assigned to each element along the fault.	103
Figure 5.4	Comparison between analytical and numerical solutions for: (a) ESS profile; (b) slip along the fault.	104
Figure 5.5	Average shear stress and slip showing the pre-slip and post-slip stress states. The shear stress and slip are averaged along the 54.5 m rupture length.	105
Figure 5.6	Average shear stress and slip along the well-oriented fault during the pressurization process.	108

Figure 5.7	Effects of pressure increments on the magnitude of the seismic energy radiated by the well-oriented fault activation.	109
Figure 5.8	Average shear stress and slip along the misoriented fault during the pressurization process.	110
Figure 5.9	Effects of pressure increments on the magnitude of the seismic energy radiated by the activation of the misoriented fault.	111
Figure 5.10	Slip distribution along the pressurization domain.....	112
Figure 5.11	Changes in radiated seismic energy and moment with pressure increment patterns and fault orientations.	113

LIST OF TABLES

Table 1.1	Unstable Failure and Seismicity Induced by Mining.....	2
Table 1.2	Unstable Failure and Seismicity Induced by Tunneling.	4
Table 1.3	Examples of Seismicity Induced by Hydraulic Fracturing.	5
Table 1.4	Recorded Cases of Induced Seismicity Associated with Deep Wastewater Disposal.	7
Table 1.5	Examples of Seismicity Triggered by Geothermal Systems.....	9
Table 2.1	Energy Components during Excavation of Circular Opening Encompassed by Infinite Elastic Media.	27
Table 2.2	Energy Components during Excavation of Circular Opening in a Thick Cylinder Setting.	28
Table 2.3	Analytic and Numerical Calculations of Energy Terms in the Tabular Excavation Setting.....	30
Table 2.4	Comparison of Radiated Seismic Energy Calculated by Equations 2.5 and 2.3 for Pillar Compressive Failures.	33
Table 2.5	Comparison of Radiated Seismic Energy Calculated by Equations 2.5 and 2.3 for Slip Failure.	36
Table 3.1	Geomechanical Properties of Materials and Constitutive Laws for Simulating the Single Pillar Model	55
Table 3.2	Continuously Yielding Frictional Properties of the Simulated Fault in the Direct Shear Test	60
Table 3.3	Comparison between Analytic and Numerical Methods of Calculating the Radiated Seismic Energy for Slip Failure Simulated in the Direct Shear Test	61
Table 3.4	Fault and Matrix Properties for Simulating Rupture along a Strike-Slip Fault	63
Table 3.5	Comparison between Results from UDEC and Analytical Functions by Ryder (1988) for the Simulated Fault	66
Table 4.1	Comparison of Graphical and Numerical Estimates of Seismic Energy Radiated by Shear Tests	81
Table 4.2	Comparison between Analytic and UDEC Results of Rupture Simulation	85
Table 5.1	Comparison between Analytic Calculations by Ryder (1988) and UDEC Results	105

ACKNOWLEDGEMENT

I would like to express my sincere gratitude to my advisors Dr. Masami Nakagawa and Dr. Ugur Ozbay for their continuous support of my PhD, their patience, and their immense knowledge while treating me as their friend. I would like to thank my committee members Dr. Graham Mustoe, Dr. Priscilla Nelson, Dr. Jennifer Miskimins, and Dr. Rennie Kaunda who provided me with constructive comments from different perspectives. My appreciation also extends to Dr. Ryan Garvey who helped me find my path in the PhD.

To Zahra for her love

To Esmat for her prayers

To Mohammad Mehdi for his support

CHAPTER 1

GENERAL INTRODUCTION

1.1 Introduction

Induced seismicity is shown to be a significant challenge during Rock Engineering Activities (REA), including coal mining (Dou et al., 2018), hard rock mining (Blake and Hedley, 2003), tunneling (Feng and Zhao, 2018), hydraulic fracturing, deep wastewater disposal (Ellsworth, 2013), and geothermal energy production (Zang et al., 2014). REA re-distribute *in-situ* stresses within the affected zone mainly due to underground excavations, pore pressure perturbation, or changes in the rock temperature. The stress re-distribution disturbs the mechanical equilibrium within the affected rock formations. The equilibrium can be regained mainly through compressive failure of rock or slip failure along pre-existing discontinuities. Compressive rock failure is mostly restricted to mining and tunneling activities. However, shear slip along preexisting discontinuities can occur during all REA due to either increasing the shear stress or decreasing the normal stress acting on the discontinuity. REA-induced compressive or shear slip failures may occur in an unstable or stable manner.

Compressive unstable failure is sudden crushing of rock and can be followed by seismic events with anomalous radiation of kinetic energy while stable failures occur gradually, resulting in little to zero seismic energy radiation (Cook, 1965; Salamon, 1970). The compressive unstable failure mostly occurs in close proximity to the underground excavation face or in mining pillars. The unstable slip failure is violent slip mostly along large weakness planes such as fault and dyke contacts with typical earthquake-like seismic signatures (Salamon, 1970; Van der Heever, 1984). In this general introduction, some reported cases of induced seismicity in coal mines, metal mines, tunnels, hydraulic fracturing activities, deep wastewater disposal, and geothermal systems are reviewed. The mechanisms of unstable failures in compression and shear slip are then discussed along with strategies introduced in this dissertation for studying induced seismicity.

1.2 Background

This section discusses some published history cases of seismicity associated with various REA. The aim is to state the significance and complexity of predicting unstable failures and induced seismic events.

1.2.1 Seismicity Induced by Mining

Mining-induced seismicity is referred to as rock burst and is a result of unstable compressive failure or unstable slip failure along a discontinuity. Compared to compressive unstable failures, unstable slip failures are usually more destructive and lead to larger-magnitude events (COMRO, 1988). Table 1.1 provides cases of unstable compressive and slip failures in coal and metal mines. The intensity of induced seismicity resulting from the unstable failures is shown for each case using the approximate moment magnitude (M_w) of the events.

Table 1.1 Unstable Failure and Seismicity Induced by Mining.

Mines	Unstable Failure Type	Overburden Depth	Induced Seismicity	Reference
Rustenburg platinum mining district (Mine C), South Africa	Widespread unstable failure of the mining panel	~1000 m	Greatest-magnitude event occurred in Aug 2013 with M_w 2.1	(Liu and Feng, 2018)
Rustenburg platinum mining district (Mine B), South Africa	Rupture on pre-existing faults in the vicinity of mine workings	~ 940 m	Greatest-magnitude event occurred in Sep 2006 with M_w 2.1	(Liu and Feng, 2018)
Kolar Gold Fields, India	Unstable compressive and slip failures caused directly by tectonic and indirectly by mining activities.	~ 756 m and 2700 m	Greatest-magnitude event with M_w 3 triggered a series of lower-magnitude seismic events over larger area leading to fatalities and extensive damage to the surface and underground structures	(Shivakumar et al., 1996)
Western Bushveld platinum mines, South Africa	Compressive type pillar failure was the general seismic source mechanism	~1000-1100 m	Greatest-magnitude event occurred in Nov 2008 with M_w 3 in an abandoned area	(Liu and Feng, 2018)
Piast coal mine, Upper Silesian coal basin, Poland	Interaction between mining and tectonic factors reactivated nearby faults resulting in unstable slip failures	~700-900 m	Greatest-magnitude event occurred in Feb 2010 with M_w 3.8	(Dou et al., 2018; Stec, 2007)
Crandall Canyon coal mine, USA	Widespread unstable failure of the mining panel	~610-670 m	Greatest-magnitude event in Aug 2007 with M_w 3.9 caused fatality	(Gates et al., 2008)

Mining-induced seismicity can be due to the unstable compressive failure of pillars or mining face as experienced by Western Bushveld platinum mines in South Africa and resulted in an M_w 3 seismic event (Table 1.1). Seismicity can be also induced by rupture, an unstable slip failure on preexisting faults as experience by Rustenburg platinum mining district in South Africa, leading to a seismic event with M_w 2.1. Table 1.1 indicates that seismicity may be also a result of the combination of both unstable compressive and slip failures as observed in Kolar Gold Fields in India with the greatest magnitude of M_w 3.

As can be also inferred from the cases in Table 1.1, deepening mining operations are known to contribute to the possibility of unstable failures and induced events. During the last two decades, the advancement in underground mining technologies along with increasing demands for energy and mineral resources have cause underground mines to extract deeper deposits. Presently, coal mines that are not closed due to the environmental concerns continue extracting deeper coal seams and therefore, experience larger seismic events with magnitudes more than M_w 3. The M_w 3.8 event in Piast coal mine in Poland (Table 1.1) is an example of a seismic event induced by mining operations in deep coal mines. With the continued deepening of mines in the world, the challenge of induced seismicity is expected to exacerbate.

The mining-induced seismicity can interrupt the mining operations for months or lead to the definitive closure on a working face or mine scale. The fatality that can result from such events along with the risks associated with the financial loss indicate that developing tools for overcoming this challenge is a top priority in designing prospective mines or re-engineering currently active mines. However, understanding mechanisms of unstable failures and defining measures representative of mining-induced seismic potentials have remained as a challenge in the field of rock mechanics. Complex mining layouts and geological structures in the vicinity of mines introduce further complications to this challenge. For example, depth of mining cannot be the representative measure because as Table 1.1 shows there is not always a direct relationship between the mining depth and the occurrence and intensity of induced seismic events.

1.2.2 Seismicity Induced by Tunneling

Unstable failures during tunneling and shaft-boring operations cause a dynamic hazard posing a significant threat to the safety of workers and operation performance. Table 1.2 indicates three examples of seismic events induced by tunneling excavations, comparing overburden depths and excavation methods. It was previously believed that sudden removal of materials by blasting operations is the main reason for the occurrence of unstable failures and, therefore, gradual excavation of a tunnel by Tunnel

Boring Machines (TBM) can prevent unstable failures. However, as shown in Table 1.2, recent evidence suggests that under the same rock geomechanical properties, unstable failure may occur during both machine and drill-and-blast excavations (Ortlepp and Stacey, 1994).

Table 1.2 Unstable Failure and Seismicity Induced by Tunneling.

Project	Excavation Method	Induced Seismicity	Overburden Depth	Reference
Jinping II Hydropower Station, China	TBM	An event with magnitude M_w 2 in Nov 2009 broke TBM main beam and resulted in fatality	2333 m	(Zhang et al., 2012)
	Drill-and-blast	Seismic event in Feb 2010 destructed support in headrace tunnel #2 and resulted in injury	1900 m	
Parbati II hydroelectric station, India	TBM	Excavation of Adit 2 by TBM induced events caused insignificant failure along the spring line	775 m	(Panthi, 2012)
	Drill-and-blast	Great-magnitude events caused fatality during the drill-and-blast excavation in Adit 1	810 m	
Tianshengqiao II hydropower station, China	Roadheaders	24 events during the excavation of headrace tunnels by roadheaders	800 m	(Feng and Zhao, 2018)
	Drill-and-blast	six events during excavation by drill-and-blast techniques	800 m	

The underlying mechanisms of unstable failure in tunneling are not fully understood but depths of tunnels are shown to play an important role (Dammyr, 2016; Gong et al., 2012; Grandori et al., 2011; Myrvang et al., 1998; Myrvang and Grimstad, 1983; Panthi, 2012). Recently increasing demands for the underground transportation in the US implies the necessity of deeper tunneling and shaft-sinking activities in more challenging ground conditions. Therefore, more cases of unstable failures leading to greater-magnitude seismic events can be expected in prospective projects.

1.2.3 Seismicity Induced by Hydraulic Fracturing

Hydraulic fracturing is a reservoir-stimulation technique where low permeability rocks are fractured by a pressurized injection fluid. During hydraulic stimulation, low-magnitude, microseismic events emerge due to the formation of tensile or shear fractures or slip failure along pre-existing discontinuities. However, high-magnitude seismic events may also occur during the long-term operation

of hydraulic fracturing. Some of the reported events attributed to the long-term hydraulic fracturing are listed in Table 1.3.

The Marcellus Shale of the Appalachian Basin in Pennsylvania, West Virginia, Ohio, and New York is one of the major shale plays in the US, located within a region featured by low levels of natural seismic activity. Since 2005, the beginning of the major development of the field by hydraulic fracturing techniques, to 2009 six seismic events of magnitude greater than M_w 2 were reported within this area, the largest of which was M_w 2.3. An abnormal sequence of earthquakes in this area was reported beginning in 2009, including 21 tremors of greater than M_w 3.0 with the largest of M_w 3.6 in the Horn River Basin, British Columbia (Table 1.3). The fluid injection during hydraulic fracturing was shown to cause these seismic events by triggering slip on pre-existing faults outside of the stimulation area (BC Oil and Gas Commission, 2012).

Table 1.3 Examples of Seismicity Induced by Hydraulic Fracturing.

Location	ΔV^* (m ³)	Intensity of Largest Induced Event		Reference
		Seismic Moment (J)	Magnitude	
Bowland shale, UK	4.2×10^3	3.2×10^{12}	M_w 2.3 event in 2011	(De Pater and Baisch, 2011)
Youngstown, OH	-	-	M_w 2.3 event in March 2011, possibly due to hydraulic fracturing operations in Pennsylvania	(BC Oil and Gas Commission, 2012)
Garvin County, OK	1.8×10^4	3.5×10^{13}	M_w 3.0 event in Jan 2011	(Holland, 2013)
Horn River Basin, British Columbia	-	-	M_w 3.6 event in Oct 2010	(BC Oil and Gas Commission, 2012)

ΔV^* : Volume of the fluid injected from the beginning of injection until the time of the event

However, amongst over millions of wells that have been hydraulically stimulated in the US in unconventional shale resources, there are only a handful of confirmed occurrences of induced seismicity felt at the surface (McClure & Horne, 2014). Thus, more studies are required to understand the contribution of the long-term hydraulic fracturing to the reported induced seismicity.

1.2.4 Seismicity Induced by Deep Wastewater Disposal

Disposal of wastewater into deep strata or basement formations is believed to contribute the most to injection-induced seismic hazards through activating pre-existing faults (Ellsworth, 2013; Zang et al., 2014). Deep disposal wells can take wastewater, the fluid that naturally coexists with oil and gas within reservoirs and fluid generated after hydraulic fracturing operations, into such porous rock formations as sandstone or limestone. Figure 1.1a shows typical rock formations where wastewater is disposed and altered stress patterns mainly by changing pore pressure within the formation.

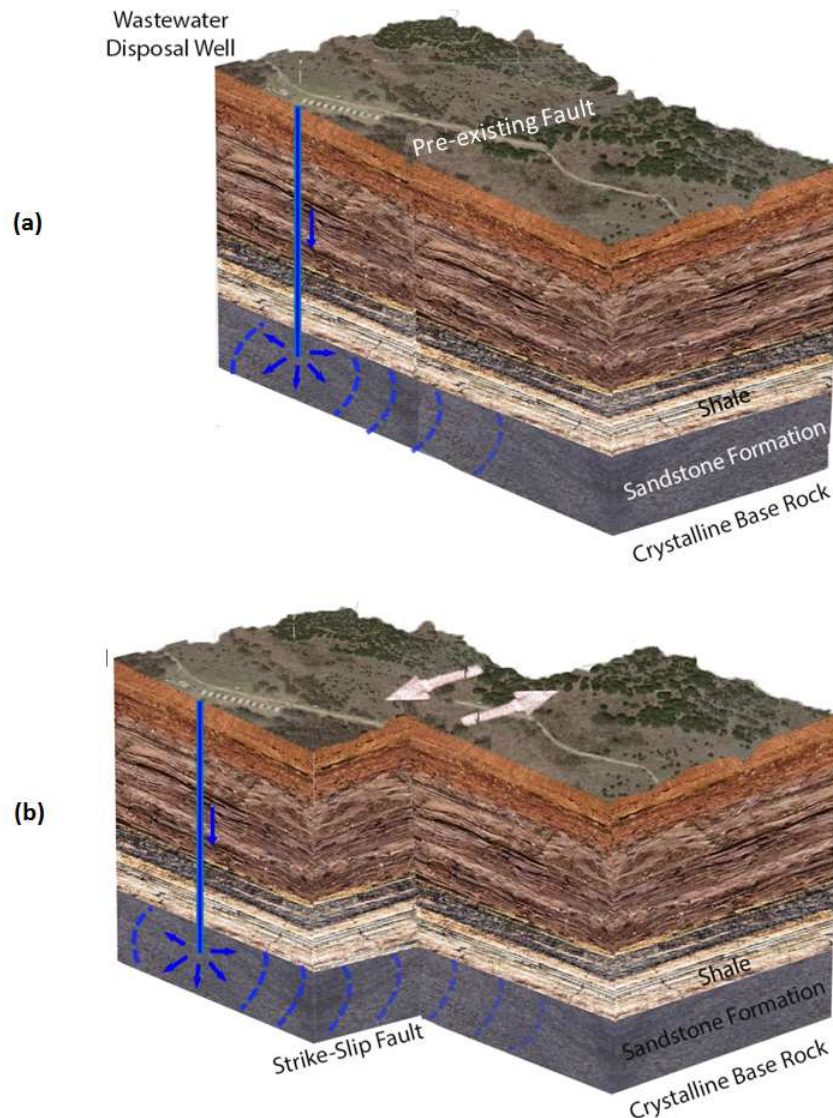


Figure 1.1 Schematics of seismicity induced by wastewater disposal: a) wastewater injection in the vicinity of a pre-existing fault oriented in the favor of slip with respect to the tectonic loadings; b) reactivated fault as a result of the stress disturbance caused by the injection process.

Large seismic events may be triggered by altering stress patterns around a pre-existing fault, leading to an unstable slip on the fault. Figure 1.1b gives an example of a pre-existing fault triggered by the wastewater disposal. Table 1.4 provides reported cases of seismicity associated with deep wastewater disposal. The M_w 4.9 event that struck northeast Denver, Colorado in 1967 was at the time the largest earthquakes believed to be induced by wastewater injection (Herrmann et al., 1981). In 2011, wastewater disposal into a depleted oil field triggered the M_w 5.7 event in Prague, Oklahoma. The source for this event was on a fault within 200 meters of two injection wells that had operated for 18 years with no unusual seismicity until an M_w 4.1 earthquake in 2010 followed by the M_w 5.7 event in 2011 (Keränen et al., 2011). The largest recorded earthquake associated with wastewater disposal occurred in Pawnee, OK in Sep 2016 with M_w 5.8.

Table 1.4 Recorded Cases of Induced Seismicity Associated with Deep Wastewater Disposal.

Projects	ΔV^* (m ³)	Intensity of Largest Induced Event		Reference
		Seismic Moment (J)	Moment Magnitude	
Dallas-Fort Worth Airport, TX	2.8×10^5	8.9×10^{13}	M_w 3.3 event in May 2009	(Frohlich et al., 2011)
Ashtabula, OH	6.2×10^4	2.8×10^{14}	M_w 3.6 event in Jul 1997	(Nicholson and Wesson, 1990; Seeber et al., 2004)
Ashtabula, OH	3.4×10^5	8.0×10^{14}	M_w 3.9 event in Jan 2001	(Nicholson and Wesson, 1990; Seeber et al., 2004)
Youngstown, OH	8.4×10^4	8.3×10^{14}	M_w 4 event in Dec 2011	(Ohio Department of Natural Resources, 2012)
Prague, OK	-	-	M_w 4.1 event in Feb 2011	(Keränen et al., 2013)
Paradox Valley, CO	3.3×10^6	3.2×10^{15}	M_w 4.3 event in May 2000	(Ake and J., 2005)
Raton Basin, CO	4.3×10^5	4.5×10^{15}	M_w 4.4 event in Sep 2011	(Meremonte et al., 2002)
Guy, AR	6.3×10^5	1.2×10^{16}	M_w 4.7 event in Sep 2010	(Horton, 2012)
Painesville, OH	1.2×10^6	2.0×10^{16}	M_w event 4.8 in Jan 1986	(Nicholson et al., 1988)
Timpson, TX	9.9×10^5	2.2×10^{16}	M_w 4.8 event in May 2012	(Frohlich et al., 2014)
Rocky Mountain Arsenal, Denver, CO	6.3×10^5	2.1×10^{16}	M_w 4.9 event in Aug 1967	(Herrmann et al., 1981)
Raton Basin, CO	7.8×10^6	1.0×10^{17}	M_w 5.3 event Aug 2011	(McGarr, 2014)
Prague, OK	1.2×10^7	3.9×10^{17}	M_w 5.7 event in Nov 2011	(Keränen et al., 2013)
Pawnee, OK	-	-	M_w 5.8 event in Sep 2016	(Yeck et al., 2017)

ΔV^* : Volume of the fluid injected from the beginning of injection until the time of the event

Research done in Rangely Oil Field in northwest Colorado (Raleigh et al., 1976) and the Paradox Valley, Colorado (Ake and J., 2005) showed that it may be possible to control induced seismicity by controlling the total volume of the injected fluid. However, Table 1.4 suggests evidence of recorded induced earthquakes where the proportionality between injection volume and intensity of induced

seismicity varies over orders of magnitude between different projects. Therefore, injection volume may not be reliably regarded as the only indicator for inducing seismicity. Observations on the unconventional hydrocarbon production in the US also confirms that only a few projects have shown notable seismicity out of millions of wells that may have injected the same or even more volume of water into the reservoir (McClure and Horne, 2014). Mechanisms leading to the fault reactivation and elements contributing to the stability of the triggered slip on the fault and the intensity of the induced seismicity require further investigations.

1.2.5 Seismicity Induced by Geothermal Systems

Enhanced Geothermal Systems (EGS) are human-made reservoirs characterized by the use of hydraulic fracturing stimulation to increase flow rate between injection and production wells in high temperature, low permeability rocks. Fluid circulation extracts heat from the reservoir (thermal drawdown) and provides the heat energy required by thermal power plants on the surface. The stimulation process using hydraulic fracturing mostly involves triggering slip on pre-existing fractures. Shear slip followed by dilation increases the discontinuity aperture, the gap between the two plates of a discontinuity. As such, the reservoir permeability is permanently enhanced resulting in an improvement in the well productivity (Tester et al., 2006). Water injection into the conventional geothermal systems has also become a common strategy for extended and sustained production of geothermal resources. For example, steam condensate, stream waters, and most recently treated wastewater are injected into The Geysers in California mainly for reducing the trend of declining reservoir pressures.

One of the challenges in the geothermal resource development and exploitation is dealing with noticeable seismic events that arise as a consequence of the induced slip and can be sometimes felt at the surface. Beside microseismicity noted during the stimulation process of EGS, long-term injection of water and extracting of geothermal energy can also cause high-magnitude induced seismic events away from the injection wells (Majer et al., 2007). Table 6.1 shows seven geothermal reservoirs and their associated seismicity with a highest recorded magnitude of Mw 4.6 in The Geysers, California.

In 1998 and 2003, the new supply pipelines were installed in the southeast Geysers to mitigate the production decline. The supply pipelines almost doubled the injection rates into the Southeast Geysers that was accompanied by a rise in the number of microseismic events with the largest magnitude of Mw 4.6 (Beall et al., 1999).

Table 1.5 Examples of Seismicity Triggered by Geothermal Systems.

Location	ΔV^* (m ³)	Temperature	Depth (km)	Intensity of Largest Induced Event		Reference
				Seismic Moment (J)	Magnitude	
Rosemanowes, United Kingdom	1.0×10^5	100 C°	2.6	-	M _w 0.16	(Richards et al., 1994)
Fjällbacka, Sweden	43.0×10^6	16 C°	0.5	-	M _w 0.20	(Jupe et al., 1992)
Ogachi, Japan	9.2×10^4	230 C°	1.0	-	M _w 2.00	(Shapiro et al., 2007)
Soulz, France	3.9×10^4	150-200 C°	3.4-5.0	2.5×10^{13}	M _w 2.90	(Majer et al., 2007)
Basel, Switzerland	1.2×10^4	190 C°	5.0	1.4×10^{14}	M _w 3.40	(Baisch et al., 2006)
Cooper Basin, Australia	2.0×10^4	250 C°	4.0	3.9×10^{14}	M _w 3.70	(Majer et al., 2007)
The Geysers, CA, USA	2.1×10^7	240 – 350 C°	3.5-5.5	-	M _w 4.60	(Cladouhos et al., 2010)

ΔV^* : Volume of the fluid injected from the beginning of injection until the time of the event

The lack of clear proportionality between magnitudes of events in Table 1.5 and depths of events, volumes of injected fluid, and reservoir temperatures shows the complexity of assessing seismic hazard potentials in prospective geothermal systems. Next section discusses the mechanics of unstable failures in different settings.

1.3 Mechanisms of Unstable Failures

Examples of induced seismic events in different REA in Tables 1.1-1.5 showed the significance of studying mechanisms of induced seismicity. These tables also reflected the complexity of these mechanisms since there is no dominant relationship between, for example, volume of the injected fluid and occurrence or intensity of injection-induced events. Seismic potentials in a rock engineering project may depend on site-specific features, including spatial variability of geological structures, rock fracture networks, rock mechanical properties, and *in-situ* stresses within the affected zone. Computational methods or numerical modeling are a useful tool for studying phenomena like induced seismicity that depend on site-specific features while cannot be subject to laboratory experiments on geological scales. The challenge is to develop methodologies and define a representative measure of a seismic event occurrence and intensity for studying elements contributing to seismic potentials associated with various REA. To address this challenge, the mechanisms of unstable failures that lead to seismicity need to be

first explored. Cook (1965) first discussed seismicity induced by mining activities and introduced the concept of failure stability. Later, Dieterich (1979) further studied the concept of unstable shear slip. The next section investigates this theoretical concept of failure instability by using mechanical mass-spring models.

1.3.1 Instability of Slip Failure

Dieterich (1979) discussed the notion of instability in shear slip using a mass-spring system (Figure 1.2). The specimen (a rigid mass) is connected to a point load through a spring that moves the specimen over a surface. The point load is a velocity loading so that a constant velocity develops the increasing load F inside the spring. The spring in this configuration resists against elongation and is regarded as the loading system. Figure 1.2a shows the specimen and spring with stiffness k_1 and length L_1 before loading. Figure 1.2b shows the spring elongated to L_2 by the increasing load F , developing F_s on the interface. The load F_s is the frictional force that acts in the opposite direction of F .

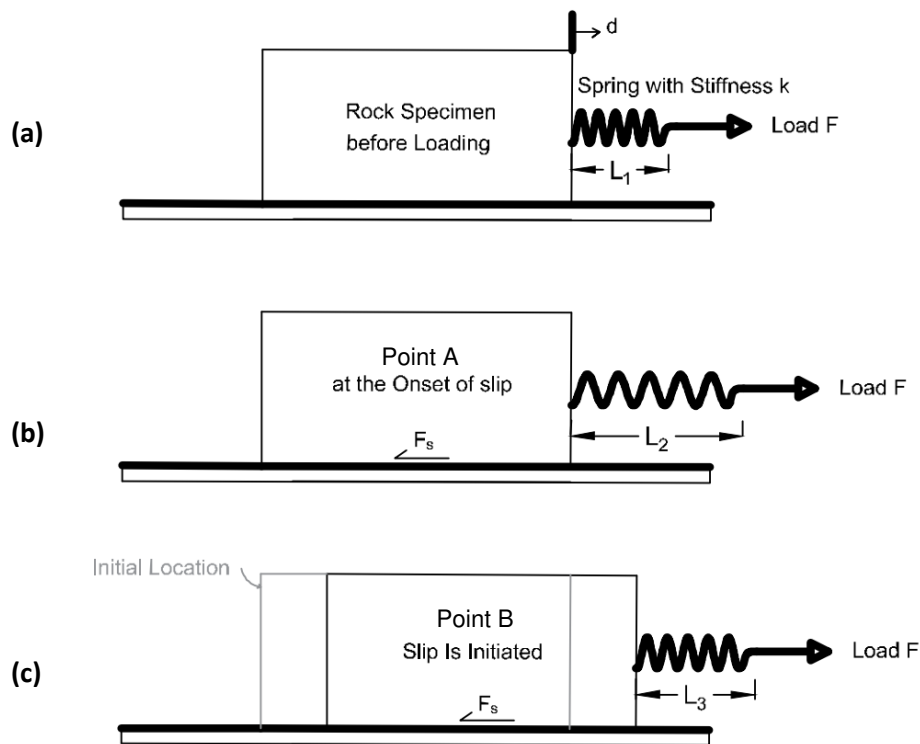


Figure 1.2 The mass-spring loading system where the mass is pulled by a spring over the surface. (a) The mass-spring system before starting the velocity loading and developing F within the spring. (b) The mass is loaded to the point of failure. The spring is elongated and frictional force F_s is developed on the interface. This figure corresponds to the state of loading system at point A in Figure 1.3a. (c) The slip is initiated and spring is once again unloaded, representative of the loading system at point B in Figure 1.3a.

Figure 1.2c shows the system once slip is arrested and irreversible shear displacement d is incurred. After the slip arrest, the spring rebounds but may not reach its initial length L_1 if the velocity loading is still applied. Dieterich (1979) showed that the slip along the interface in Figure 1.2 is stable if the stiffness of the spring is greater than the post-peak slope of the frictional force-shear displacement curve. Figure 1.3a shows a typical frictional force-shear displacement curve indicating variations of the frictional force F_s with the shear displacement d . The spring load line is also plotted in Figure 1.3a with a slope that represents the spring stiffness k_1 . The spring load line is the line through which the spring is unloaded when slip occurs.

At any point before point A on the frictional force - shear displacement curve in Figure 1.3a, the force F inside the spring equals F_s and system is in equilibrium. Instability is the result of an imbalance between loads applied to a system and loads required for driving the slip. The dynamic process occurs starting from the limit equilibrium point A where the force F inside the spring exceeds the frictional force F_s on the interface and thus unstable slip initiates. The blue dashed lines in Figure 1.3a indicate the difference between the force F applied by the spring as it is unloaded and F_s , the force required to move the specimen. The system regains equilibrium once the spring force F and F_s are again equal at point B. After this point, slip continues in a stable mode. Figure 1.3b shows three different loading systems equivalent to springs with stiffness values of k_2 , k_2 , and k_3 while $k_1 < k_2 < k_3$. Loading under the spring with stiffness k_2 still introduces force imbalance but, compared to the loading with spring stiffness k_1 , less shear displacement is required before the system once again attains equilibrium.

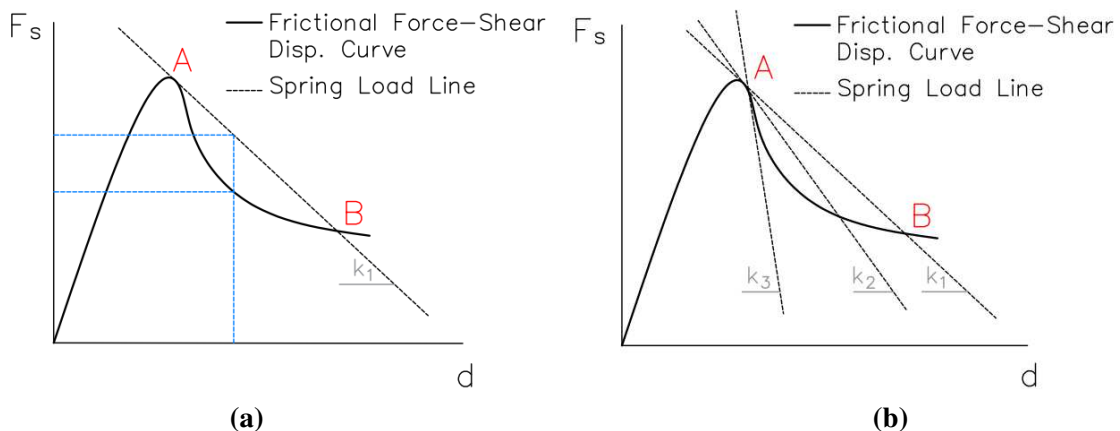


Figure 1.3 Typical frictional force-shear displacement curve and loading lines: (a) the load line with stiffness k_1 shows the concept of instability incurred between points A and B; (b) the conceptual role of spring stiffness values of $k_1 < k_2 < k_3$ in instability of slip.

The notion of instability disappears when the load F is applied through the spring with stiffness k_3 . This means slip is unstable if the post-peak slope of the frictional force-shear displacement curve is greater than the spring stiffness or the slope of the load line. Unstable shear slip leads to an oscillation in the spring or the loading system, resulting in a seismic event.

1.3.2 Instability of Compressive Failure

Initially Cook (1965) and then Salamon (1970) used a mass-spring system to explore the concept of failures instability. Figure 1.4 shows the concept of compressive unstable failure in a mass-spring system. The specimen (mass) is loaded in series where compressive loading is applied to the specimen by a point load connected to the spring. The point load is a velocity loading so that a constant velocity develops the increasing load F inside the spring. The spring in this configuration resists against contraction and is referred to as loading system. Figure 1.4a shows the specimen before loading while Figure 1.4b indicates the specimen at the onset of failure where the spring is contracted, inducing elastic deformation in the specimen. The spring length changes based on the spring stiffness and load F within the spring. As such, the highest spring contraction occurs in Figure 1.4b just before the failure. Figure 1.4c shows the schematically failed specimen where relatively large plastic deformation occurs.

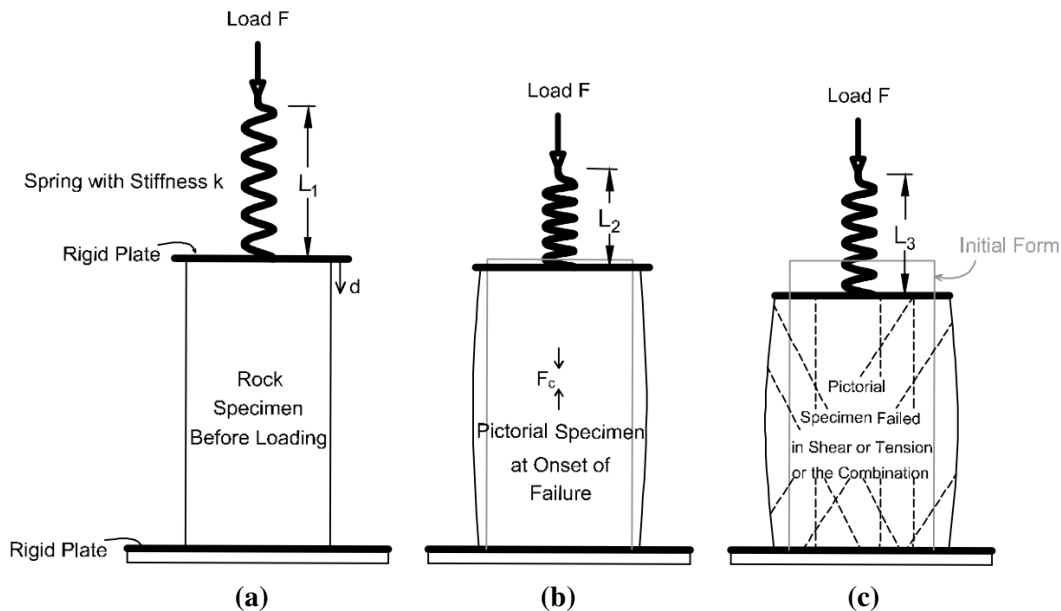


Figure 1.4 Conceptual model of loading system and failure in compression. The specimen is loaded by a compressive force applied through a spring. (a) Specimen and spring system before loading. (b) Specimen loaded by the contracted spring at the onset of failure. (c) Failed specimen and elongated spring.

After the failure, the spring rebounds but may not return to its initial value (L_1) if the velocity loading is still applied. Cook (1965) and Salamon (1970) showed that instability of the rock failure in Figure 1.4 depends on the stiffness of the spring. They argued that rock failure in compression is unstable if the spring stiffness is less than the post-peak slope of the compressive force-displacement curve recorded within the specimen during the test. Theoretical analyses (Cook, 1965) and laboratory experiments (Cook, 1966; Wiebols et al., 1968) showed that the relationship between compressive force F_c and displacement d in brittle rock is similar to that shown by the solid curve in Figure 1.5a. The compressive force-displacement curve represents the specimen compressive strength and is mainly a function of specimen mechanical properties.

Figure 1.5a also shows a spring load line that is the line through which the spring is unloaded after failure. The spring unloading occurs during the transition in spring lengths between Figures 1.4b and 1.4c. The slope of the spring load line indicates the spring stiffness value k_1 . Figure 1.5a indicates one spring load line at point A where failure is initiated. However, one can draw spring load lines with the same slope k_1 at each point on the force-displacement curve before point A because until the loading reaches this point, the load F in the spring equals F_c , the reaction force within the specimen. Rock deformation is stable during the unfailed state and also in the failing state up to point A at which the load line of the spring becomes tangent to the force-displacement curve (Figure 1.5a). A comparison between the specimen force-displacement curve and the spring load line shows that after point A the force F inside the spring becomes greater than the force F_c required for driving the failure, introducing an unbalanced force in the system.

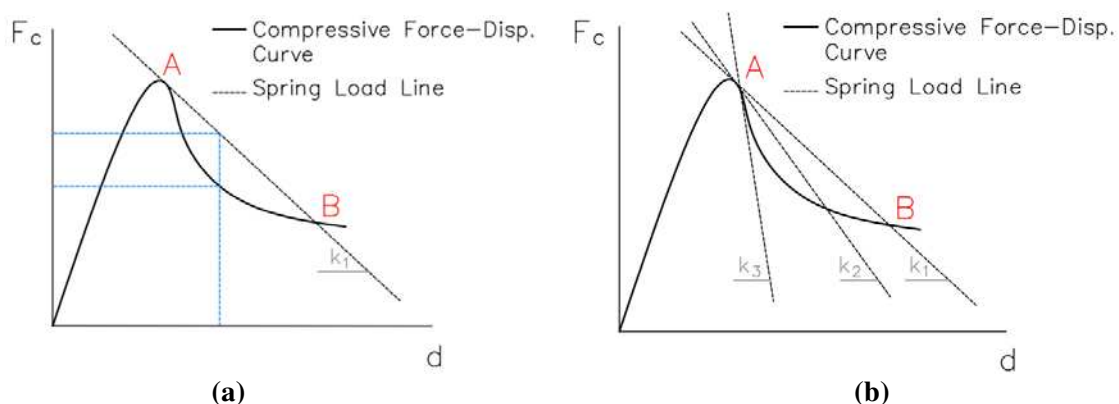


Figure 1.5 Concept of instability in compression (after Salamon (1970) with modification): (a) typical compressive force-displacement curve and the spring load line with stiffness k_1 . The blue dashed lines signify the force imbalance between points A and B; (b) the conceptual role of spring stiffness in instability of a compressive failure. The dashed black lines show spring with stiffness values of $k_1 < k_2 < k_3$. Points A and B on each figure correspond to Figures 1.4b and 1.4c, respectively.

That is, the action force becomes more than the reaction force, causing the transition from the static equilibrium to a dynamic system. The dashed blue lines in Figure 1.5a indicate the difference between the spring force F and F_c between points A and B. The dynamic system caused by the force imbalance between points A and B indicates instability of the compressive failure and leads to a seismic event characterized by an oscillation in the spring. The system regains equilibrium once the spring load line again meets the specimen force-displacement curve at point B. Figure 1.5b compares loading by springs with stiffness values of k_1 , k_2 , and k_3 so that $k_1 < k_2 < k_3$. The spring with stiffness k_3 eliminates the instability since points A and B coincide, the system maintains its equilibrium during the failure, resulting in a stable failure. This shows instability emerges when the spring stiffness is less than the post-peak slope of the force-displacement curve. The concept of failure instability using mechanical spring models was further advanced by Rice (1983), Linkov (1996), and Napier and Malan (1997) but since then it had not received much attention until 2011 when a research group at Colorado School of Mines started evaluating the possibility of applying the abovementioned instability concept to modeling seismicity in underground coal mines (Garvey and Ozbay, 2013; Gu and Ozbay, 2014; Kias et al., 2011; Poeck et al., 2016).

This dissertation adopts the concept of instability in section 1.3 and translates it into a computational framework capable of exploring elements contributing to the occurrence and magnitudes of seismic events not only in mining but in tunneling, deep wastewater disposal, and geothermal activities. This study introduces a framework for studying seismicity induced by each REA by developing methodologies, calibrating modeling approaches, and verifying results. Existing analytical solutions, theoretical approaches, and field data are used to check the results and calibrate the models. Given that the radiation of anomalous seismic energy can differentiate stable from unstable failures, the developed framework introduces the radiated seismic energy as a measure of occurrence and intensity of seismic events. Two methods for estimating radiated seismic energy is presented. One tracks the transfer of static energy terms during failure and thus estimates the magnitude of seismic energy radiated if conditions of instability emerge. The other estimates the radiated seismic energy by calculating the kinetic energy that has to be damped from a system to ensure re-gaining equilibrium. The Universal Distinct Element Code (UDEC) is used For the numerical study (Itasca, 2016) and method development. Section 1.4 describes the main features of UDEC and constitutive laws used in this dissertation.

1.4 Modeling in UDEC

UDEC falls under the category of discontinuous analysis techniques in which a rock mass is represented as assemblies of blocks divided by interfaces that are analogous to geological discontinuities.

Behaviors of discontinuities, responses of solid materials and their interactions under different loading are computed in these techniques. In UDEC, deformable blocks divided by discontinuities are discretized into finite difference elements while the interaction between blocks is calculated based on the distinct element techniques. Therefore, the calculation alternates between the application of a force-displacement law at all interfaces and Newton's second law at all blocks. Based on fixed or known displacements, forces are calculated on the interfaces. Using Newton's second law, the motion and deformation of the blocks are calculated from the calculated forces. Based on material constitutive laws, stresses within the block are updated. The application of discontinuity constitutive relations and the force-displacement law yields new forces and displacements on the interfaces. This calculation cycle continues for the next timestep.

UDEC uses an explicit time-marching approach to directly solve the equations of motion. The time-stepping algorithm in UDEC reduces timestep until the acceleration and velocities are constant within the timestep. As such, the timestep is sufficiently small that disturbances during the single timestep cannot grow between two neighboring discrete elements. The discontinuous analysis technique with the time-marching approach in UDEC allows studying dynamic and quasi-static problems in fractured rock. Modeling induced seismicity requires quasi-static and dynamic calculations; a quasi-static scheme for building up stresses before failure and a dynamic calculation scheme for simulating the unstable movement of materials after failure initiation until regaining equilibrium. Next sections discuss UDEC built-in joint and material constitutive laws that are used for simulations in this dissertation.

1.4.1 Continuously Yielding Joint Model

Empirical models for discontinuity behaviors under shear, including the Mohr-Coloumb joint model, only provide responses to simple loading conditions. Cundall and Hart (1984) introduced the Continuously Yielding (CY) constitutive relation to better fit laboratory tests and simulate the internal mechanism of progressive damage of discontinuities under shear forces. The CY model accounts for the nonlinear behavior observed in physical tests similar to the typical example in Figure 1.3. The CY model uses shear displacement on a discontinuity as a measure of the damage along the discontinuity and shows the irreversible damage behavior from the onset of shearing. The damage is simulated by defining a target shear strength that decreases continuously as a function of the accumulated shear displacement on the discontinuity. The peak of the frictional force-shear displacement curve is reached when the target strength equals the shear stress applied on the discontinuity. After the peak, the discontinuity enters the post-peak softening regime. The shear strength decreases with increasing the accumulated shear displacement until the shear strength reaches the residual strength of the discontinuity. This enables CY

models to simulate different softening behaviors, allowing for modeling different post-peak slopes required for studying slip instability.

1.4.2 Mohr-Coloumb Strain Softening Constitutive Law

As shown in Figure 1.5, unstable compressive failures require simulation of post-peak failure responses. To simulate compressive failures with different post-peak responses, this study assigns Mohr-Coloumb Strain Softening constitutive law (MCSS) to the failing rock materials. MCSS is based on the standard Mohr-Coloumb model but allows manipulating cohesion, friction angle, dilation angle, and tensile strength as a function of plastic strain. In MCSS, the force-displacement curve is linear to the point of failure, meaning that displacements are elastic before failure. After failure, the total displacement is composed of elastic and plastic parts. By defining different variations of the rock cohesion, friction angle, dilation angle, and tensile strength with the plastic strain of rock, different post-peak behavior can be simulated. This allows for simulating softening responses (Figure 1.5) as observed in laboratory tests or in site-specific conditions (Edelbro, 2009).

As shown in Figure 1.6, in this work, a softening behavior is accomplished by lowering the cohesion from 1.7 MPa to zero after an appropriate level of plastic strain. Dilation angle is assumed zero and friction angle is kept constant during the simulation at 20 degrees.

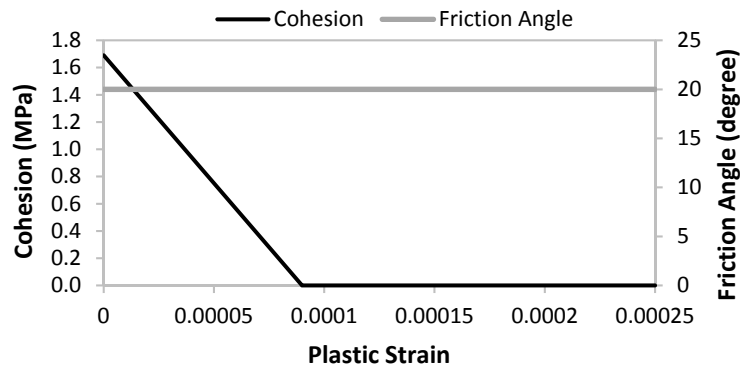


Figure 1.6 Simplified softening parameters used in this study. Cohesion is reduced from 1.7 Mpa to zero. Friction angle is kept constant at 20 degrees.

An important aspect of strain softening modeling is the model mesh size. Regardless of the parameters used, the mesh size dictates the failure band during a compressive failure of rock. If rock

failure is due to a compressive-induced shear failure, the shear band thickness depends on the size of the meshes in the model.

1.5 Thesis Organization

This section summarizes approaches adopted in this study for developing a framework for investigating induced seismicity in different REA. Chapter 2 investigates induced seismicity in tunneling and shaft-boring operations. Unstable failure of rock in tunneling and shaft sinking operations results in seismicity that introduces a significant challenge regarding the safety and performance of tunneling contracts. As the depths and locations of tunneling and shaft-sinking operations become increasingly challenging, more cases of unstable failures have been reported (Dammyr, 2016; Gong et al., 2012; Grandori et al., 2011; Myrvang et al., 1998; Myrvang and Grimstad, 1983; Panthi, 2012). The challenge is to understand conditions required for rock unstable failures and identify burst-prone areas as it is directly related to work safety, operation timing, rock support design, and finally functional requirements of underground facilities. The necessity of adopting mitigating strategies depends on an estimation of the unstable rock failure intensity in preliminary phases of underground facility projects. Unstable failure intensity is referred to as the magnitude of radiated seismic energy and is a function of the degree of failure instability and the extent of the damaged zone. By calculating the radiated seismic energy as a measure of intensity, effects of both damaged zone extent and failure instability on assessing failure intensity can be considered.

For calculating radiated seismic energy, chapter 2 first validates the energy calculation framework within UDEC. Energy terms calculated from UDEC models are compared to values obtained from available analytic solutions for the formation of a circular opening in a stressed elastic medium. A methodology and modeling approach are provided for mechanistically studying the induced seismicity in tunnels and shafts by calculating the seismic energy radiated from the failure once conditions for instability are met. Two cases of unstable failures are studied: compressive failure of rock surrounding the excavation; unstable slip on a normal fault next to the advancing excavation. Parametric studies are performed for exploring roles of elements such as in-situ stresses, excavation size, Young's modulus on the occurrence and intensity of unstable failures in tunnels and shafts. Given the verification examples provided in chapter 2, the developed framework can be used for identifying areas prone to high magnitude seismic events capable of restricting tunneling and shaft-boring operations.

Building upon the validated energy calculation in chapter 2, chapter 3 explores the concept of instability in compressive and shear slip failures in a mining configuration. A rectangular tabular

excavation supported by a single pillar is modeled. By advancing the excavation, the pillar failure is simulated and its instability is measured by the magnitude of the radiated seismic energy. The compressive failure instability is explored through parametric studies on the post-peak response of the pillar failure and the loading system stiffness. This chapter also briefly investigates the mechanism of rupture (unstable shear slip) along a discontinuity through a numerical direct shear test. The results of radiated seismic energy are verified against the instability magnitudes given by Salamon (1970). The same approach is extended to model a strike-slip fault where loading conditions, rupture area, stress drop, radiated seismic energy, and seismic moment are compared against the analytical solutions provided by Ryder (1988). Further investigating the rupture mechanism along the strike-slip fault is presented in chapter 4 where a modeling approach and methodology required for evaluating seismicity in deep wastewater disposal and geothermal reservoirs are developed.

Chapter 4 details rupture mechanics along a strike-slip fault and calibrates modeling approach for dynamic modeling of natural earthquake rupture propagation and arrest. Unlike the common approach in rupture simulators (Kaneko and Shearer, 2015; Madariaga et al., 1998), a procedure is developed for the quasi-static buildup of shear stresses over the strike-slip fault until rupture is initiated on a nucleation patch. Then, a dynamic model is calculated to complete the self-propagating rupture up to the point of the rupture arrest. This approach avoids prescribing rupture initiation patch, allowing for investigating relationships between the stress distribution, slip distribution, rupture arrest, and radiated seismic energy. For calibrating loading conditions and making results independent of the grid (or mesh) size and damping scheme in UDEC, we check modeling results against an analytical solution. Finally, one application of the developed methodology is exemplified by investigating variations of the radiated seismic energy, seismic moment, slip instability, rupture length, and maximum slip along fault models with different responses under various loading system stiffness values. The capability of the developed methodology in grasping pulse-like distribution of slip and radiated seismic energy over time are discussed. Results of each simulation are verified against globally recorded seismic field data.

Using the calibrated models introduced in chapter 4, chapter 5 explores seismicity induced by injection of fluid into the fractured ground. Fluid injection into deep underground formations can be followed by seismic events characterized by a significant release of strain energy stored in the rock. Enhanced geothermal systems (Majer et al., 2007) and deep wastewater injection fields (Zhang et al., 2013) have been shown to induce seismic events. Injection-induced events mainly occur due to rupture on pre-existing faults. This chapter extends the framework for utilizing mechanical modeling to study the evolution of injection-induced rupture and to adjust the operational parameters to minimize the intensity of the induced events. Chapter 5 exemplifies injection-induced rupture and investigates underlying

mechanisms of an induced event by relying on the estimation of radiated seismic energy as a measure of the rupture intensity. It is assumed that the elastic rock surrounding the single fault is impermeable and that different fluid injection patterns can be simulated by steady-state pressure increments within the fault plane. Simulating different injection patterns with these simplifying assumptions reduces the complexity of induced seismicity and allows better understanding the mechanics of the injection-induced rupture. Finally, chapter 6 provides a comprehensive conclusion from this study and discusses future research.

1.6 References

- Ake, J., J., 2005. Deep-injection and closely monitored induced seismicity at Paradox Valley, Colorado. *Bull. Seismol. Soc. Am.* 95, 664–683. <https://doi.org/10.1785/0120040072>
- Baisch, S., Weidler, R., Voros, R., Wyborn, D., de Graaf, L., 2006. Induced seismicity during the stimulation of a geothermal HFR reservoir in the Cooper Basin, Australia. *Bull. Seismol. Soc. Am.* 96, 2242–2256. <https://doi.org/10.1785/0120050255>
- BC Oil and Gas Commission, 2012. Investigation of observed seismicity in the Horn River Basin -August 2012.
- Beall, J.J., Stark, M.A., Smith, J.L.B., Kirkpatrick, A., 1999. Microearthquakes in The Southeast Geysers before and after SEGEP injection. *Geotherm. Resour. Coun. Trans.* 23, 253–257.
- Blake, W., Hedley, D.G.F., 2003. Rockbursts : case studies from North American hard-rock mines. Society for Mining, Metallurgy, and Exploration.
- COMRO, 1988. Chamber of Mines Research Organization-An industry guide to methods of ameliorating the hazards of rockfalls and rockburts. Chamber of Mines Research Organization.
- Cook, N.G.W., 1966. A rigid 50-ton compression and tension testing machine. *Jl S. Afr. Instn mech. Engrs* 16, 89–92.
- Cook, N.G.W., 1965. A note on rockbursts considered as a problem of stability. *J. South African Inst. Min. Metall.* 65, 437–446.
- Cundall, P.A., Hart, R.D., 1984. Analysis of block test no. 1 : inelastic rock mass behavior. Itasca Consulting Group, Minneapolis.
- Dammyr, Ø., 2016. Prediction of brittle failure for TBM tunnels in anisotropic rock: A case study from Northern Norway. *Rock Mech. Rock Eng.* 49, 2131–2153. <https://doi.org/10.1007/s00603-015-0910-z>
- De Pater, C.J., Baisch, S., 2011. Geomechanical study of Bowland Shale seismicity synthesis report.
- Dieterich, J.H., 1979. Modeling of rock friction: 1. Experimental results and constitutive equations. *J. Geophys. Res.* 84, 2161. <https://doi.org/10.1029/JB084iB05p02161>
- Dou, L., Lu, C., Li, Z.-H., 2018. Case Histories of rockburst at coal mines, in: *Rockburst Mechanisms, Monitoring, Warning, and Mitigation*. Elsevier, pp. 93–113. <https://doi.org/10.1016/B978-0-12-805054-5.00004-4>
- Edelbro, C., 2009. Numerical modelling of observed fallouts in hard rock masses using an instantaneous cohesion-softening friction-hardening model. *Tunn. Undergr. Sp. Technol.* 24, 398–409. <https://doi.org/10.1016/J.TUST.2008.11.004>
- Ellsworth, W.L., 2013. Injection-induced earthquakes. *Science* (80-.). 341.

- Feng, X.-T., Zhao, Z., 2018. Case Histories of Rockburst at Tunnels, in: *Rockburst Mechanisms, Monitoring, Warning, and Mitigation*. Elsevier, pp. 27–45. <https://doi.org/10.1016/B978-0-12-805054-5.00002-0>
- Frohlich, C., Ellsworth, W., Brown, W.A., Brunt, M., Luetgert, J., MacDonald, T., Walter, S., 2014. The 17 May 2012 M4.8 earthquake near Timpson, East Texas: An event possibly triggered by fluid injection. *J. Geophys. Res. Solid Earth* 119, 581–593. <https://doi.org/10.1002/2013JB010755>
- Garvey, R., Ozbay, U., 2013. Assessing coal bumps from excess energy in finite difference models, in: *11th International Conference on Ground Control in Mining*. [https://doi.org/10.1016/0886-7798\(92\)90134-4](https://doi.org/10.1016/0886-7798(92)90134-4)
- Gates, R.A., Michael, G., Morley, T.A., O'Donnell Jr, J.R., Smith, G.E., Watkins, T.R., Weaver, C.A., Zelanko, J.C., 2008. Report of investigation—fatal underground coal burst accidents, August 6 and 16, 2007, Crandall Canyon Mine, Genwal Resources Inc, Huntington, Emery County, Utah. <https://doi.org/ID 42-01715>
- Gong, Q.M., Yin, L.J., Wu, S.Y., Zhao, J., Ting, Y., 2012. Rock burst and slabbing failure and its influence on TBM excavation at headrace tunnels in Jinping II hydropower station. *Eng. Geol.* 124, 98–108. <https://doi.org/10.1016/J.ENGCEO.2011.10.007>
- Grandori, R., Bieniawski, Z.T., Vizzino, D., Romualdi, P., 2011. Hard rock extreme conditions in the first 10 km of TBM driven Brenner Exploratory Tunnel, in: *Rapid Excavation and Tunneling Conference*.
- Gu, R., Ozbay, U., 2014. Distinct element analysis of unstable shear failure of rock discontinuities in underground mining conditions. <https://doi.org/10.1016/j.ijrmms.2014.02.012>
- Herrmann, R.B., Park, S.-K., Wang, C.-Y., 1981. The Denver earthquakes of 1967-1968. *Bull. Seismol. Soc. Am.* 71, 731–745.
- Holland, A.A., 2013. Earthquakes triggered by hydraulic fracturing in South-Central Oklahoma. *Bull. Seismol. Soc. Am.* 103, 1784–1792. <https://doi.org/10.1785/0120120109>
- Horton, S., 2012. Disposal of hydrofracking waste fluid by injection into subsurface aquifers triggers earthquake swarm in central Arkansas with potential for damaging earthquake. *Seismol. Res. Lett.* 83, 250–260. <https://doi.org/10.1785/gssrl.83.2.250>
- Itasca, 2016. Background - The 2D Distinct Element Method, UDEC Manual.
- Jupe, A.J., Green, A.S.P., Wallroth, T., 1992. Induced microseismicity and reservoir growth at the Fjällbacka hot dry rocks project, Sweden. *Int. J. Rock Mech. Min. Sci. Geomech. Abstr.* 29, 343–354. [https://doi.org/10.1016/0148-9062\(92\)90511-W](https://doi.org/10.1016/0148-9062(92)90511-W)
- Kaneko, Y., Shearer, P.M., 2015. Variability of seismic source spectra, estimated stress drop, and radiated energy, derived from cohesive-zone models of symmetrical and asymmetrical circular and elliptical ruptures. *J. Geophys. Res. Solid Earth* 120, 1053–1079. <https://doi.org/10.1002/2014JB011642>
- Keranen, K.M., Savage, H.M., Abers, G.A., Cochran, E.S., 2013. Potentially induced earthquakes in Oklahoma, USA: Links between wastewater injection and the 2011 Mw 5.7 earthquake sequence. *Geology* 41, 699–702. <https://doi.org/10.1130/G34045.1>
- Khademian, Z., Nakagawa, M., Garvey, R., Ozbay, U., 2017. Role of fluid injection pressure in inducing seismicity, in: *Proceedings of the 42nd Workshop on Geothermal Reservoir Engineering*. p. 10.
- Khademian, Z., Nakagawa, M., Ozbay, U., 2018. Modeling earthquake rupture propagation based on calculations of energy components. *Manuscr. Submitt. Publ.*
- Khademian, Z., Poeck, E., Garvey, R., Ozbay, U., 2016. Studies of seismicity generated by unstable

- failures around circular excavations, in: 50th U.S. Rock Mechanics/Geomechanics Symposium. American Rock Mechanics Association, Houston, Texas.
- Kias, E.M.C., Gu, R., Garvey, R., Ozbay, U., 2011. Modeling unstable rock failure during a uniaxial compressive strength test, in: 45th U.S. Rock Mechanics / Geomechanics Symposium. American Rock Mechanics Association, San Francisco, California.
- Linkov, A.M., 1996. Rockbursts and the instability of rock masses. *Int. J. Rock Mech. Min. Sci. Geomech. Abstr.* 33, 727–732. [https://doi.org/10.1016/0148-9062\(96\)00021-6](https://doi.org/10.1016/0148-9062(96)00021-6)
- Liu, J.-P., Feng, X.-T., 2018. Case histories of rockbursts at metal mines, in: *Rockburst Mechanisms, Monitoring, Warning, and Mitigation*. Elsevier, pp. 47–92. <https://doi.org/10.1016/B978-0-12-805054-5.00003-2>
- Madariaga, R., Olsen, K., Archuleta, R., 1998. Modeling dynamic rupture in a 3D earthquake fault model. *Bull. Seismol. Soc. Am.* 88, 1182–1197.
- Majer, E.L., Baria, R., Stark, M., Oates, S., Bommer, J., Smith, B., Asanuma, H., 2007. Induced seismicity associated with Enhanced Geothermal Systems. *Geothermics* 36, 185–222. <https://doi.org/10.1016/J.GEOTHERMICS.2007.03.003>
- McClure, M.W., Horne, R.N., 2014. Correlations between formation properties and induced seismicity during high pressure injection into granitic rock. *Eng. Geol.* 175, 74–80. <https://doi.org/10.1016/J.ENGCEO.2014.03.015>
- Meremonte, M.E., Lahr, J.C., Frankel, A. d., Dewey, J.W., Crone, A.J., Overturf, D.E., Carver, D.L., Bice, W.T., 2002. Investigation of an earthquake swarm near Trinidad, Colorado, August-October 2001.
- Myrvang, A., Blindheim, O., Johansen, E., 1998. Rock stress problems in bored tunnels, in: Bruland A et Al (Ed) *Norwegian TBM tunneling—30 Years of Experience with TBMs in Norwegian Tunneling* (Publication No. 11). Norwegian soil and rock engineering association, Oslo, pp. 71–78.
- Myrvang, A., Grimstad, E., 1983. Rockburst problems in Norwegian Highway tunnels, recent case histories., in: *Rockbursts--Prediction and Control*. Institute of Mines and Metallurgy, London, pp. 133–139.
- Napier, J.A.L., Malan, D.F., 1997. A viscoplastic discontinuum model of time-dependent fracture and seismicity effects in brittle rock. *Int. J. Rock Mech. Min. Sci.* 34, 1075–1089. [https://doi.org/10.1016/S1365-1609\(97\)90201-X](https://doi.org/10.1016/S1365-1609(97)90201-X)
- Nicholson, C., Roeloffs, E., Wesson, R.L., 1988. The northeastern Ohio earthquake of 31 January 1986: Was it induced? *Bull. Seismol. Soc. Am.* 78, 188–217.
- Nicholson, C., Wesson, R.L., 1990. Earthquake hazard associated with deep well injection: a report to the U.S. Environmental Protection Agency. *Bulletin*.
- Ohio Department of Natural Resources, 2012. Preliminary report on the Northstar 1 class II injection well and the seismic events in the Youngstown, Ohio, area. Ohio.
- Ortlepp, W.D., Stacey, T.R., 1994. Rockburst mechanisms in tunnels and shafts. *Tunneling Undergr. Sp. Technol.* 9, 59–65.
- Panthi, K.K., 2012. Evaluation of rock bursting phenomena in a tunnel in the Himalayas. *Bull. Eng. Geol. Environ.* 71, 761–769. <https://doi.org/10.1007/s10064-012-0444-5>
- Poeck, E., Khademian, Z., Garvey, R., Ozbay, U., 2016. Modeling unstable rock failures in underground excavations, in: 2016 ISRM International Symposium, 2016 (Ed.), *Rock Mechanics and Rock Engineering: From the Past to the Future*. CRC Press, Ürgüp-Nevşehir, Turkey, pp. 505–509.

<https://doi.org/10.1201/9781315388502-86>

- Raleigh, C.B., Healy, J.H., Bredehoeft, J.D., 1976. An Experiment in earthquake control at Rangely, Colorado. *Science* (80-.). 191, 1230–1237.
- Rice, J.R., 1983. Constitutive relations for fault slip and earthquake instabilities. *Pure Appl. Geophys.* 121, 443–475. <https://doi.org/10.1007/BF02590151>
- Ryder, J. a., 1988. Excess shear stress in the assessment of geologically hazardous situations. *J. South African Inst. Min. Metall.* 88, 27–39.
- Salamon, M.D.G., 1970. Stability, instability and design of pillar workings. *Int. J. Rock Mech. Min. Sci.* 7, 613–631. [https://doi.org/10.1016/0148-9062\(70\)90022-7](https://doi.org/10.1016/0148-9062(70)90022-7)
- Seeber, L., Armbruster, J.G., Kim, W.-Y., 2004. A fluid-injection-triggered earthquake sequence in Ashtabula, Ohio: implications for seismogenesis in stable continental regions. *Bull. Seismol. Soc. Am.* 94, 76–87. <https://doi.org/10.1785/0120020091>
- Shivakumar, K., Rao, M.V.M.S., Srinivasan, C., Kusunose, K., 1996. Multifractal analysis of the spatial distribution of area rockbursts at Kolar Gold Mines. *Int. J. Rock Mech. Min. Sci. Geomech. Abstr.* 33, 167–172. [https://doi.org/10.1016/0148-9062\(95\)00066-6](https://doi.org/10.1016/0148-9062(95)00066-6)
- Stec, K., 2007. Characteristics of seismic activity of the Upper Silesian Coal Basin in Poland. *Geophys. J. Int.* 757–768. <https://doi.org/10.1111/j.1365-246X.2006.03227.x>
- Van der Heever, P.K., 1984. Some technical and research aspects of the Klerksdrop seismic network, in: *1st International Congress on Rockbursts and Seismicity in Mines*. pp. 349–350.
- Wiebols, G.A., Jaeger, J.C., Cook, N.G.W., 1968. Rock property tests in a stiff testing machine, in: *The 10th U.S. Symposium on Rock Mechanics (USRMS)*. Austin, Texas, pp. 297–329.
- Yeck, W.L., Hayes, G.P., McNamara, D.E., Rubinstein, J.L., Barnhart, W.D., Earle, P.S., Benz, H.M., 2017. Oklahoma experiences largest earthquake during ongoing regional wastewater injection hazard mitigation efforts. *Geophys. Res. Lett.* 44, 711–717. <https://doi.org/10.1002/2016GL071685>
- Zang, A., Oye, V., Jousset, P., Deichmann, N., Gritto, R., MCGarr, A., Majer, E., Bruhn, D., 2014. Analysis of induced seismicity in geothermal reservoirs – An overview. *Geothermics* 52, 6–21.
- Zhang, C., Feng, X.-T., Zhou, H., Qiu, S., Wu, W., 2012. Case histories of four extremely intense rockbursts in deep tunnels. *Rock Mech Rock Eng* 45, 275–288. <https://doi.org/10.1007/s00603-011-0218-6>
- Zhang, Y., Person, M., Rupp, J., Ellett, K., Celia, M.A., Gable, C.W., Bowen, B., Evans, J., Bandilla, K., Mozley, P., Dewers, T., Elliot, T., 2013. Hydrogeologic controls on induced seismicity in crystalline basement rocks due to fluid injection into Basal reservoirs. *Groundwater* 51, 525–538.

CHAPTER 2

MODELING UNSTABLE ROCK FAILURES IN TUNNELING AND SHAFT BORING BASED ON ENERGY BALANCE CALCULATIONS

A paper submitted to the journal of *Tunneling and Underground Spaces*

Zoheir Khademian and Ugur Ozbay

2.1 Abstract

Excavation in the highly stressed ground may lead to unstable compressive failures of rock or unstable shear slip along discontinuities in the vicinity of the underground excavation, resulting in induced seismic events. This chapter investigates the theory that unstable and stable failures can be differentiated based on the magnitude of seismic energy radiated during failure. A computational framework is introduced by developing a methodology and modeling approach for studying the intensity of induced events by calculating the seismic energy radiated by their occurrence. A Universal Distinct Element Code (UDEC) is used to demonstrate compressive- and shear-type unstable failure events in several cases of circular openings (representing tunnels and shafts). Energy components calculated by the models are first validated from analytical solutions. Then, we explore effects of different elements on the intensity of unstable failure events in circular openings surrounded by brittle rocks and advanced next to a normal fault with slip-weakening behaviors. The radiated seismic energy is calculated for each model in UDEC and is used to assess the relative failure intensity for the given conditions and to identify the circumstances under which high magnitude-events can be expected. The results demonstrate that different combinations of the rock brittle behavior, slip-weakening response of discontinuity, rock mechanical properties, excavation size, and in-situ stresses can result in an unstable failure that can be followed by a significant radiation of seismic energy. Once this condition of an unstable failure emerges, larger excavation under higher in-situ stresses further increases the intensity of unstable failures through expanding the failure zone. Therefore, commonly used measures of damaged zone extent and magnitude of in-situ stresses may not help estimate the intensity unless conditions for the unstable failure are first met. The energy-based methods of analysis outlined in this chapter provide a rational means of studying unstable failures in potentially complex combinations of rock mass properties, excavation geometries, and failure characteristics of faults or bedding plane discontinuities.

2.2 Introduction

Unstable failure of rock in tunneling and shaft-sinking operations represents a significant challenge regarding the safety and performance on tunneling contracts. The challenge is to understand conditions required for unstable failures and identify burst-prone areas as it is directly related to the work safety, operation timing, rock support design, and finally functional requirements of underground facilities.

Unstable failures (aka rock burst) are mostly referred to the sudden crushing and ejection of rock under compressive loading (aka strain burst) or rapid slip due to shear loading along preexisting discontinuities (rupture). Excavating an underground opening re-distributes pre-existing stresses around the excavation. Re-distributed stresses can cause compression rock failure or shear slip along preexisting discontinuities. Compressive failures occur due to the high stresses exceeding the strength of the rock or due to a drop of confinement of the rock surrounding the opening. Slip along preexisting discontinuities occurs due to either increasing the shear stress or decreasing the normal stress acting on the discontinuity within the affected stress field. Compressive and shear slip failures may occur in an unstable or stable manner. Unstable failures can be followed by radiating significant seismic energy while stable failures occur gradually causing little to zero radiation of seismic energy (Salamon, 1974).

The necessity of adopting mitigating strategies depends on an estimation of the unstable rock failure intensity in preliminary phases of underground facility projects. Unstable failure intensity is referred to as the magnitude of radiated seismic energy and is a function of the degree of failure instability and the extent of the damaged zone. Cook (1965) and Rice (1983) established theoretical grounds for the unstable failure mechanism as a problem of failure instability in compression and shear, respectively. Once rock failure is unstable, the extent of the damaged zone can also contribute to the magnitude of radiated seismic energy.

Researchers have developed empirical criteria relating the damaged zone extent (as representative of the seismic event intensity) to the rock brittleness, rock mass compressional strength, and in-situ stresses (Diederichs, 2007; Martin et al., 1999; Martin and Christiansson, 2009). However, there is not enough study on the role of both failure instability and damaged zone in the intensity of a seismic event. This chapter provides a computational framework for studying the intensity of induced seismic event by calculating the seismic energy radiated from the failure once conditions for instability are met. By calculating the radiated seismic energy as a measure of intensity, we account for effects of both damaged zone extent and failure instability on assessing the induced event intensity.

In order to validate the energy calculation, this chapter first compares the energy calculated from UDEC models to values obtained by available analytic solutions for the formation of an underground opening in an elastic medium. Idealized models are then constructed in UDEC for exploring the concept of instability in compressive and shear slip modes, as two main unstable failure mechanisms in a tunneling or shaft-sinking configuration. The significance of these two mechanisms is that for the former, the source and damage locations are coincident, which means the rock involved in the seismic source is also part of the damaged zone. In contrast, the latter mechanism represents shear slip along a preexisting discontinuity that is the source of the seismic event while the damaged zone can be around the excavation surface. As an example of the methodology application, we construct parametric studies and show that variations of the rock elastic modulus, deviatoric stresses, failure brittleness, rock strength, and in-situ stresses can play a critical role in seismic event instability. Given verification examples provided in this chapter, the developed framework can be used for identifying areas prone to high-magnitude seismic events capable of restricting tunneling and shaft-boring operations.

2.3 Methodology

External loadings of rockmass as tectonic and gravitational stresses accumulate strain energy in rock formations underground. Excavating an underground opening causes a disturbance in pre-existing stresses and induces convergence of excavation boundaries, resulting in emerging two sources of energy: the strain energy that was previously stored in the excavated material and the work done by the external forces acting in the direction of the convergence. Assuming the rock is elastic, the available energy can be stored in the form of elastic strain energy within the surrounding rock with no sign of failure. If the material is excavated at once, the available energy can be also partly released in the form of elastic oscillations along excavation boundaries (Salamon, 1974). This oscillation is representative of radiated seismic energy and is analogous to a box-spring system in which the mass is suddenly released leading to a fluctuation in the system. Dissipative processes ultimately damp out the radiated seismic energy and the system reaches equilibrium. An energy balance can be used to describe the transfer of energy, given as:

$$W + U_m = W_k + U_c \quad (2.1)$$

where W stands for the change in external work, U_m is the energy stored in the mined out material and W_k is the radiated seismic energy. U_c denotes the difference between the total stored strain energy before and after the excavation and internally includes U_m . By defining $\Delta U = U_c - U_m$, Equation 2.1 can be rearranged for directly calculating radiated seismic energy as:

$$W_k = W - \Delta U \quad (2.2)$$

where ΔU is the change in the strain energy stored in the material surrounding the excavation. ΔU remains positive as long as materials are elastic because more strain energy can be always stored in the elastic rock after the excavation.

UDEC reaches a solution of static equilibrium for each model by a dynamic approach where a damping force dissipates a fraction of system kinetic energy at each time step and leaves the remaining kinetic energy (U_k) for driving the simulation. The magnitude of the damping force depends on a damping constant and unbalanced force on a gridpoint while the direction of the damping force dictates energy dissipation (Cundall, 1987). This study uses a damping constant of 0.8. The calibration process for selecting this damping constant is included in chapter 4. UDEC cumulatively records the dissipated energy as damped work (W_d). Besides calculating radiated seismic energy from static energy components in Equation 2.2, the radiated seismic energy can be also obtained by summing the dynamic components of U_k and W_d , as:

$$W_k = W_d + U_k \quad (2.3)$$

Next sections show that results of the dynamic approach of Equation 2.3 match the radiated seismic energy obtained by static energy terms in Equation 2.2 and that of analytical solutions provided by Cook (1966), Duvall and Stephenson (1965), and Salamon (1984).

2.3.1 Circular Opening in an Infinite Medium

An analytical solution was derived by Duvall and Stephenson (1965) to study energy transfer when a circular excavation is instantaneously formed in an infinite elastic medium. We use a hybrid approach combining the Finite Difference Method (FDM) and Boundary Element Method (BEM) in UDEC to numerically meet the assumption of the infinite elastic medium. Figure 2.1 shows the model configuration and boundary elements on the outer boundary. We discretize inner and outer external boundaries of the model using FDM and BEM elements, respectively, so that the continuity of the induced displacements and stresses are satisfied at the interface (Itasca, 2016). In-situ stresses are developed by a pressure boundary condition to prevent inaccuracy produced by fixed boundary conditions. In general, the drawback in using pressure loading boundary condition is that the model must be large enough to prevent any overestimation, leading to a significant rise in the calculation time. In this case, the boundary integral equations in the BEM considers everything inside the outer boundary as a hole while everything outside of this boundary is treated as an infinite elastic medium. As a consequence, there is no necessity in using an extremely large model to avoid the adverse effects of pressure boundary conditions.

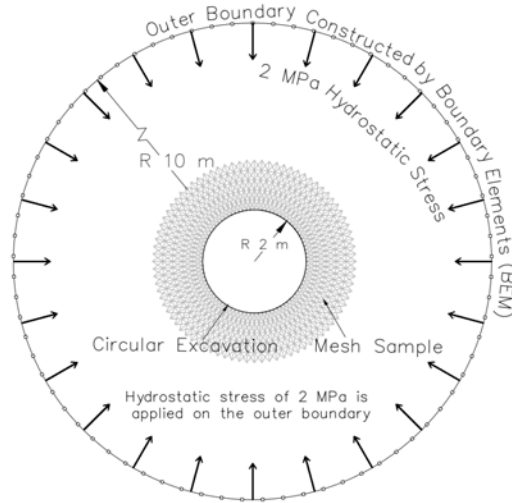


Figure 2.1 Model boundaries for simulating a circular opening in an infinite medium.

As shown in Figure 2.1, the external boundary in the FDM/BEM model has a radius (R) of 10 m. The circular opening with 2 m radius (c) is constructed at the center of the model. Young's modulus (E) and Poisson's ratio (ν) of rock are 10 GPa and 0.2, respectively. Table 2.1 summarizes equations provided by Duvall and Stephenson (1965) for external work, strain energy change, and radiated seismic energy.

Table 2.1 Energy Components during Excavation of Circular Opening Encompassed by Infinite Elastic Media.

Terms	Duvall and Stephenson (1965)	UDEC	Difference	
W	$2\pi(1+\nu)h p^2 c^2 / E$	12.06 kJ	11.94 kJ	0.99%
ΔU	$\pi(1+\nu)h p^2 c^2 / E$	6.03 kJ	5.92 kJ	1.82%
W_k	$\pi(1+\nu)h p^2 c^2 / E$	6.03 kJ	6.02 kJ	0.17%

In Table 2.1, h represents the in-plan extension of the excavation that equals one since the simulation is two dimensional. p denotes the boundary hydrostatic pressure that is 2 MPa for this case. The UDEC result of 6.02 kJ radiated seismic energy in Table 2.1 is obtained by the dynamic scheme of Equation 2.3. Based on Equation 2.2, radiated seismic energy can be also numerically obtained by subtracting the static energy term of W from ΔU , giving the same 6.02 kJ of radiated seismic energy. The comparison between UDEC and analytical results indicates that numerical results are within less than 2% of analytically obtained values.

2.3.2 Circular Opening in Finite Elastic Medium

Salamon (1984) calculated the change in energy terms during the sudden formation of a circular excavation where the surrounding rock mass is treated as a thick-walled cylinder rather than an infinite medium. The associated numerical model excludes boundary element boundaries; however, a pressure is still applied at the external boundary to represent a far-field stress. As mentioned before, the external boundary must be far away from the excavation to guarantee that the stress and displacement calculations are not under the adverse influence of the loading condition. As Figure 2.2 shows the model external radius is increased to 120 m which is 60 times bigger than the 2 m tunnel radius.

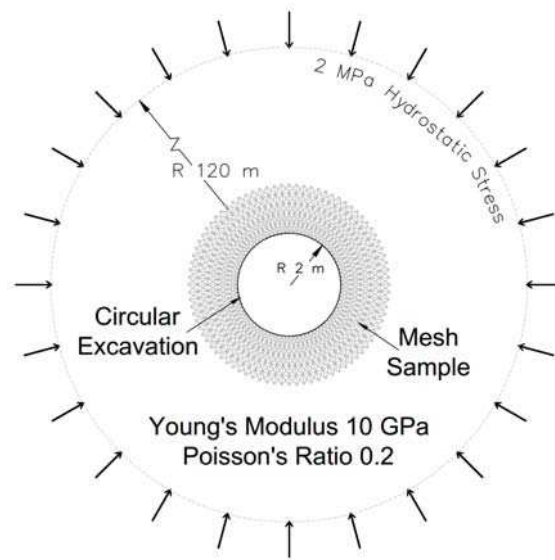


Figure 2.2 Circular opening in a finite elastic medium.

Material elastic properties and the model configuration are shown in Figure 2.2. Table 2.2 shows analytic equations by Salamon (1984) along with the comparison between UDEC and analytic results. The UDEC value of 9.62 kJ for radiated seismic energy is obtained from Equation 2.3.

Table 2.2 Energy Components during Excavation of Circular Opening in a Thick Cylinder Setting.

Terms	Salamon, 1984	UDEC	Difference	
W	$4\pi(1-\nu^2) h p^2 c^2 / E$	19.30 kJ	19.19 kJ	0.58%
ΔU	$2\pi(1-\nu^2) h p^2 c^2 / E$	9.65 kJ	9.62 kJ	0.32%
W_k	$2\pi(1-\nu^2) h p^2 c^2 / E$	9.65 kJ	9.62 kJ	0.32%
U_m	$\pi(1-2\nu)(1+\nu) h p^2 c^2 / E$	3.62 kJ	3.63 kJ	0.28%

Subtracting W from ΔU in Table 2.2 yields 9.57 kJ of radiated seismic energy, confirming the consistency between results in Equations 2.2 and 2.3. The agreement between numerical and analytical values confirms the numerical method capability to calculate applicable energy terms while excavating a circular excavation in a finite elastic medium.

2.3.3 Tabular Excavation

Cook (1966b) and then Salamon (1968) developed analytical solutions for transfer of energy when removing a thin slit from the elastic medium, analogous to the geometry of tabular excavations. We employed the pressure boundary condition shown in Figure 2.2 and constructed the thin slit by excavating an opening with a width of 10 m and height of 0.2 m. Figure 2.3 suggests the model geometry and boundary condition for the case of the tabular excavation.

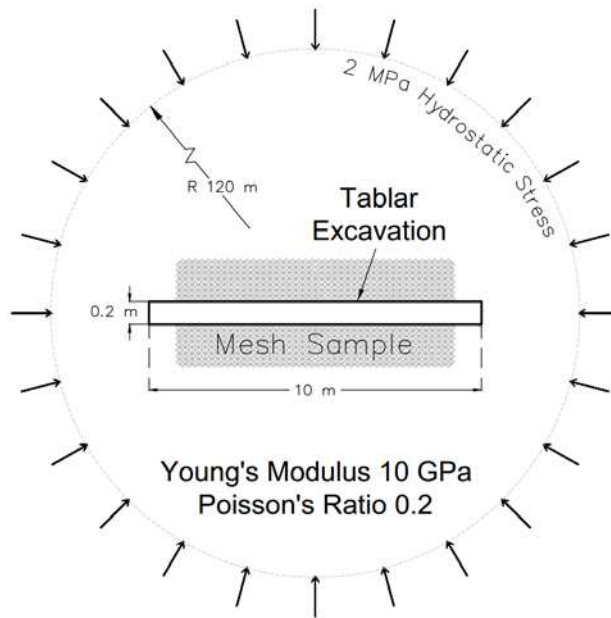


Figure 2.3 Modeling configuration of a tabular opening in an elastic medium.

Using the near-zero width to height ratio, effects of surfaces perpendicular to the roof and floor of the excavation are ignored so the assumption of slit geometry is satisfied. Table 2.3 shows the analytic equations for instantaneous excavation of the tabular opening along with UDEC results, suggesting that energy terms calculated by UDEC are consistent with the analytical values.

Table 2.3 Analytic and Numerical Calculations of Energy Terms in the Tabular Excavation Setting.

Terms	Cook (1966b) and Salamon (1968)	UDEC	Difference	
W	$2\pi(1-\nu^2)h L^2 p^2 / E$	60.32 kJ	61.13 kJ	1.3%
ΔU	$\pi(1-\nu^2)h L^2 p^2 / E$	30.16 kJ	30.40 kJ	0.80%
W_k	$\pi(1-\nu^2)h L^2 p^2 / E$	30.16 kJ	30.67 kJ	1.7%

Note that in Table 2.3, L denotes the excavation half span (5 m). The agreement between dynamic and static approaches of calculating radiated seismic energy can be again checked in Table 2.3. Results in Tables 2.1-3 suggest that the numerical methodology is capable of calculating energy components from Equations 2.1-3 once there is a transfer of energy in the system.

2.3.4 Effects of Excavation Speed

In previous sections, we showed that the sudden removal of materials from the elastic medium results in the oscillation of excavation boundary and releases radiated seismic energy. However, during a mining or tunneling operation, an underground opening is not excavated at once; rather, excavation machines or blasting techniques rather steadily advance the excavation. Compared to drill-and-blast techniques, excavation machines can provide even more gradual stress disturbance around the excavation. Gradual excavation can diminish the radiated seismic energy that could have otherwise released into the system after the sudden removal of stressed elastic materials. We can numerically simulate a gradual excavation by employing a controlled unloading procedure. That is, tractions along the newly formed excavation surface can be reduced in a slow manner. Thus, the oscillation caused by the excavation procedure is absorbed from the system and the radiated seismic energy decreases to approximately zero. This concept is demonstrated as:

$$W_k = W - \Delta U - W_i \quad (2.4)$$

where W_i is the work performed by a gradual reduction of tractions along the newly formed excavation face. Although mining and tunneling operations take place in a gradual manner, unstable failures still occur with a signature of radiating a significant magnitude of seismic energy (Cook, 1966a). Evidence also suggests that in some cases, under the same hard rock conditions, unstable failures occur with excavation machines but not with drill-and-blast operations (Dammyr, 2016; Ortlepp and Stacey, 1994). The next section discusses why the significant magnitude of seismic energy can be still radiated due to the expression of unstable failure while the excavation is advanced gradually.

2.3.5 Introducing Inelastic Energy Term

Removing the assumption of excavating in elastic materials, we introduce failure in the rock surrounding an opening. Failure consumes available energy through plastic work (W_p) caused by inelastic deformation of rock. Plastic work contributes to the energy balance of Equation 2.2 as:

$$W_k = W - \Delta U - W_i - W_p \quad (2.5)$$

Plastic work has also an inherent impact on the energy balance by affecting the energy storing capacity of the failure zone. Once rock fails, its capability for storing energy decreases such that ΔU reduces and becomes a negative term, providing more energy available for the crushing process. Note that Equation 2.5 serves as the energy balance in both compressive- and shear-type unstable failures; however, W_p in the former mostly refers to the inelastic deformation of rock mass while in the latter, W_p is mostly generated by the friction work between pre-existing weak planes. Note that dynamic calculations of radiated seismic energy can be still performed by Equation 2.3 without further modification. The concept of unstable compressive and shear failures with regards to Equations 2.3 and 2.5 are discussed in next sections.

2.4 Concept of Compressive-type Unstable Failure

Cook (1965) presented a theoretical derivation of energy terms during unstable rock failure using laboratory compression tests on cylindrical rock samples. These studies revealed that seismic energy radiated during failure depends profoundly on the loading system stiffness (stiffness of the loading machine platens) and the post-peak slope of stress-displacement curves (brittleness behavior of rock specimen). The loading stiffness is associated with Young's modulus and geometry of the loading system while post-peak slope is related to rock brittleness characteristics. If the stiffness of the loading system is less than the post-peak slope of the stress-displacement curve, the rock failure is unstable leading to radiating significant magnitude of seismic energy (Cook, 1965). To show the notion of compressive-type failure instability, a numerical model is constructed simulating a tabular excavation supported by a single brittle pillar, as shown in Figure 2.4.

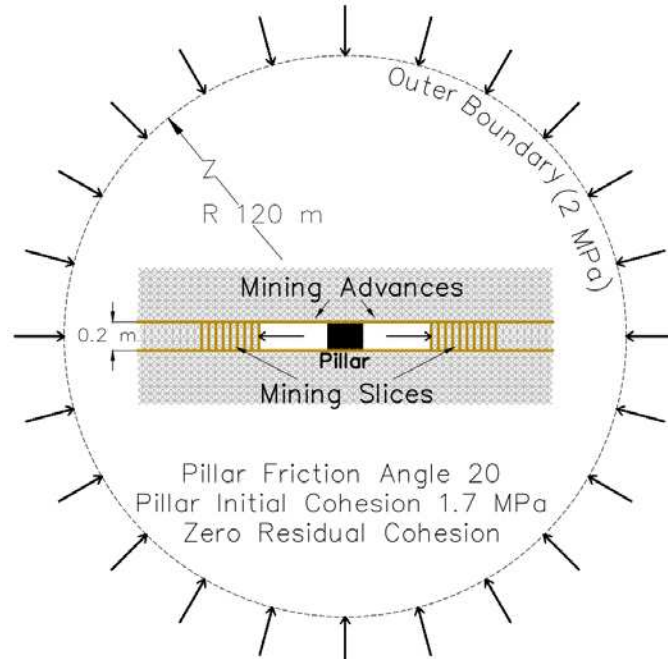


Figure 2.4 Single pillar numerical model and loading conditions.

The excavation is 0.2 m high and the pillar width is 0.2 m. The excavation is advanced steadily so oscillations caused by excavation process are minimal. One narrow mining slice, 0.05-m wide, from each entry is removed and the model is allowed to reach equilibrium at each interval. The pillar fails after excavating eighth slices from each side of the pillar. We simulate brittle and semi-brittle pillar responses for examining effects of the post-peak response of the pillar on the intensity of unstable failure. Mohr-Coulomb Strain-Softening (MCSS) constitutive law is employed to simulate semi-brittle pillar with mechanical properties provided in Figure 2.4. The vertical stress within the pillar and the convergence for the semi-brittle response are recorded during the excavation and are shown as the solid gray curve in Figure 2.5. The simulation of the brittle pillar, however, is independent of built-in constitutive laws. We assign elastic properties to the pillar and after excavating the eighth mining slices from each entry we remove the pillar, suddenly reducing the load-bearing capacity of the pillar to zero and simulating a brittle response. The solid black curve in Figure 2.5 suggests the brittle response of the pillar. In the tabular opening setting, the roof and floor of the pillar play the role of loading system. The curve of vertical stresses acting on the pillar (not inside the pillar) versus convergence represents Ground Reaction Curve (GRC). The dashed line in Figure 2.5 shows the recorded GRC as the excavation progresses and represents the reaction of the loading systems to the pillar failure. The slope of GRC indicates the loading system stiffness, which is a function of excavation dimensions and the elastic modulus of the surrounding rock.

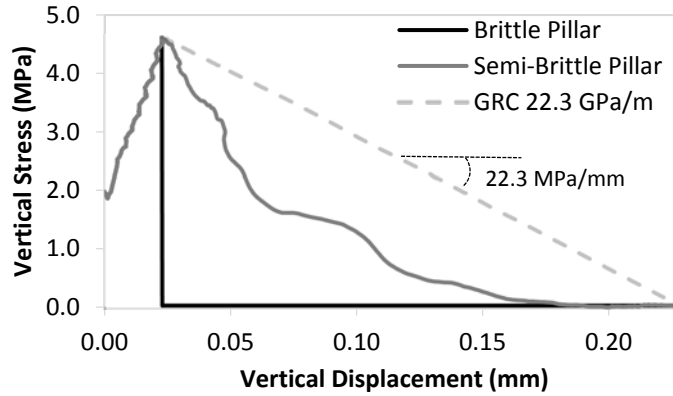


Figure 2.5 Pillar stress-displacement curves and Ground Reaction Curve.

According to the instability notion provided by Cook (1965) and Salamon (1984), the area below the GRC is the energy density available to the system for failure while the area below the pillar response signifies the amount of energy density consumed during the failure process. Finally, referring to Equation 2.5, the area between the GRC and pillar stress-convergence curve, multiplied by the pillar cross-section area yields W_k , the radiated seismic energy that follows the compression-type unstable failure.

Table 2.4 Comparison of Radiated Seismic Energy Calculated by Equations 2.5 and 2.3 for Pillar Compressive Failures.

Pillar response	Radiated seismic energy (J)		Difference
	Graphical solution - Equation 2.5	UDEC - Equation 2.3	
Semi-brittle	50.5	50.1	0.7%
Brittle	105.1	105.5	0.4%

We graphically obtained the radiated seismic energy by calculating the area between solid and dashed lines for each case and multiplying them by the 0.2 m^2 cross-section area of the pillar. The graphical estimates are based on Equation 2.5. Table 2.4 shows that the UDEC values for radiated seismic energy from Equations 2.3 and 2.5 differ by less than 0.7%. The insignificant difference originates from the numerical noise generated in the system. Consistent results of Table 2.4 give credence to the capability of the developed framework to capture the unstable failure caused by compressive rock failures.

2.5 Concept of Shear-type Unstable Failure

As discussed in chapter 1, Dieterich (1979) and then Rice (1983) used a box-spring system to explain the concept of slip instability. The contact between the box and surface was considered a discontinuity while the spring was the loading system. They showed that slip-weakening behavior of discontinuity during sliding is necessary for the energy conservation. In slip-weakening constitutive law, slip is zero until the total shear stress reaches a peak value. Once this stress has been attained, slip increases while shear strength decreases until reaching a constant residual stress (Andrews, 1976; Madariaga et al., 1998).

Dieterich (1979) showed that stable slip occurs along the contact between the box and surface if the spring stiffness (or loading system stiffness) remains greater than the post-peak slope of the contact shear stress-slip curve. A spring with a relatively lower stiffness leads to unstable slip (rupture) that causes radiating seismic energy mostly from the loading system. Other than being dependent on its material, spring stiffness is inversely related to the spring length. In the case of a geological discontinuity, blocks surrounding the discontinuity reflect the loading system whose stiffness depends on Young's modulus and ruptured length of the discontinuity. The loading system stiffness dictates the amount of strain energy that can be stored in the discontinuity wall rocks before the slip. As suggested by Equation 2.5, this stored strain energy may be partly consumed as plastic work during the slip and partly released in the form of seismic energy, resulting in seismicity.

For exploring the notion of unstable slip, we construct a numerical direct shear test comprised two rectangular blocks and each block is 0.15 m high. The direct shear test and loading configurations are shown in Figure 2.6. The top and bottom blocks have 0.2 m and 0.3 m widths, respectively, and represent a loading system comparable to the blocks surrounding a geological discontinuity.

A constant normal stress of 2 MPa is applied onto the top of the upper block and a constant horizontal velocity of 1 mm/s is applied over the left side of the upper block, as shown in Figure 2.6. Note that the upper block is not bound but free to move throughout the contact as long as the lateral loading generates the external work W . Therefore, the direct shear test configuration can be representative of an unbound fraction of a fault on geologic scales where the slip is not limited by unloaded fault segments or by segments with higher shear strengths. Along with the concept of shear-type unstable failure, this section discusses effects of loading system stiffness on the stability of a shear slip along a pre-existing discontinuity created by the interface between the two blocks in the direct shear test.

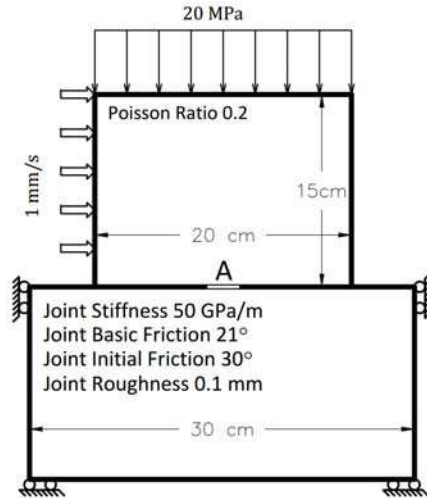


Figure 2.6 Numerical model for the direct shear test.

The Continuously Yielding (CY) joint model is used to simulate the seismological slip-weakening behavior of the discontinuity (Cundall and Lemos, 1990). Details on the CY constitutive law is included in chapter 1. Initial and residual friction coefficients are assumed 0.5 and 0.4, respectively. Figure 2.7 is the result of running two direct shear tests; one with stiff loading system and another with relatively low. Loading stiffness is varied by assigning Young's modulus of 1 GPa and 10 GPa to the upper block for simulating soft and stiff systems, respectively. A high Young's modulus of 200 GPa is assigned to the lower block for simplifying energy transfer by restricting energy storage to the upper block.

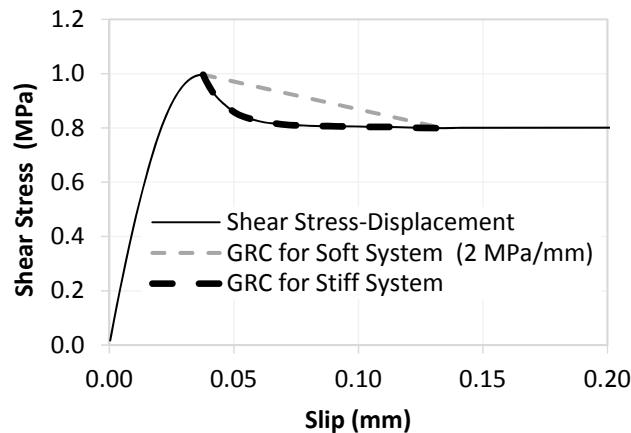


Figure 2.7 Discontinuity shear stress-slip curves and GRCs.

Dashed lines in Figure 2.7 show the GRCs for stiff and soft loading systems, obtained by recording the shear stress within the upper block (not along the contact) as the slip is initiated and

progressed. The solid line is the recorded shear stress versus slip at point A (Figure 2.6) during the loading process. The GRC for the soft loading system is linear with the slope of 2 MPa/mm while the GRC for the stiff system follows the contact shear stress-slip curve with a slope reducing from 4 to 0 MPa/mm. That is, the loading system stiffness is greater than the post-peak slope of the contact shear stress-slip for the stiff system. The area below the dashed lines theoretically represents $W - \Delta U$, the energy available for the slip failure, in each case and that of the solid line is W_p , the energy consumed throughout the slip. Based on Equation 2.5, the area between them is representative of W_k , which is radiated when the conditions for instability are met. Note that the lateral loading is performed so gradually that the only source of radiated seismic energy is the unstable slip. Thus, W_i should be excluded from the radiated seismic energy calculation in Equation 2.5.

We graphically, based on Equation 2.5, obtain the radiated seismic energy for each case and compare it with the radiated seismic energy calculated from Equation 2.3. For the stiff loading system, there is no gap between the solid and black dashed curves, meaning available energy is fully consumed by W_p and thus zero radiated seismic energy is expected. This is confirmed by the results in Table 2.5. For the soft loading system, the area between the post-peak shear stress-slip curve and the respective GRC, multiplied by the contact length of 0.2 m yields 1.43 J that relatively agrees with 1.4 J obtained from Equation 2.3. Note that for graphical calculations, we assumed the shear stress-slip at point A represents the slip behavior of the entire contact between the blocks. The 2.1% difference in Table 2.5 originates from this assumption because calculations in Equation 2.3 accounts for the behavior of the entire contact. The relative agreement between results denotes that dynamic and static calculations of radiated seismic energy in UDEC can be used to study unstable slip and induced seismicity.

Table 2.5 Comparison of Radiated Seismic Energy Calculated by Equations 2.5 and 2.3 for Slip Failure.

System Stiffness	Radiated seismic energy (J)		Difference
	Graphical solution - Equation 2.5	UDEC - Equation 2.3	
Soft system	1.43	1.4	2.1%
Stiff system	0	1.21×10^{-3}	N/A

Figures 2.5 and 2.7 showed the conditions required for occurrence of an unstable failure and intensity of induced seismic events. However, calculation of loading system stiffness and analyses of stresses for assessing failure stability are not straight forward in an underground project. With confidence gained through the analytical and theoretical studies of radiated seismic energy during failures, we can study the occurrence and intensity of an induced seismic event by calculating radiated seismic energy.

This allows for approaching more complex problems in terms of geology and excavation layouts. During the next two sections, instability in both compression and shear is triggered in a circular opening setting that can be viewed as a tunnel or shaft.

2.6 Circular Opening in a Brittle Rock

The aim is to show the capability of the numerical methodology in grasping the expression of unstable failure in tunneling or shaft-sinking settings. We simulate a circular opening excavated in a semi-brittle rock and calculate W_k as the excavation advances. There is no analytic solution at this stage for verifying modeling results, so we rely on the expected trend of variations of radiated seismic energy with excavation radius, loading system stiffness and k ratios, the ratio of *in-situ* horizontal to vertical stresses. The study of elements impacting the intensity of induced events can also help explain why some geological settings and excavation layouts are more prone to seismicity than others.

The same geometry and loading conditions as Figure 2.2 is employed with MCSS semi-brittle properties assigned to the rock surrounding the excavation. Elastic constants and mechanical properties of the simulated semi-brittle rock follow the single pillar case in Figure 2.4. Note that the MCSS constitutive law is sensitive to the mesh size such that the peak compressional strength of the material and their post-failure behavior vary as a function of mesh size. Consequently, we keep nearly the same mesh size as the single pillar case to have an insight into the material uniaxial strength. In order to simulate a steady excavation advance, we use a gradual removal of traction after removing the material. In this method, normal pressure is applied on to the internal surface just after deleting the excavation area in the model. This pressure is then slowly reduced to zero to simulate a gradual, quasi-static excavation process.

2.6.1 Compressive-type Unstable Failure and k Ratio

Effects of *in-situ* stresses on the expression of unstable failures can be studied by varying k ratio before excavating the opening. We reduce k ratio from 1 to 0.4 by increasing the vertical stresses from 2 to 5 MPa while the horizontal stress remains constant at 2 MPa. Referring to Equation 2.5, higher stresses result in higher external work W , leading to greater magnitude events if conditions for instability emerge. In addition, decreasing k ratio from 1 to 0.4 develops deviatoric stresses that can potentially expand failure zones, further decrease ΔU and result in a higher magnitude of radiated seismic energy.

Excavation size is also known to significantly impact induced tangential stresses around the excavation such that wider excavation span further expands the failure zone and thus decreases ΔU . Therefore, we expect to observe an increasing trend of radiated seismic energy as the k ratio decreases and excavation enlarges. Results of the parametric study on the excavation size and k ratio are plotted in

Figure 2.8 which shows the expected trend of variations between radiated seismic energy, k ratio, and excavation dimensions. The overall trend illustrates that instability increases with lower k ratio and larger excavations.

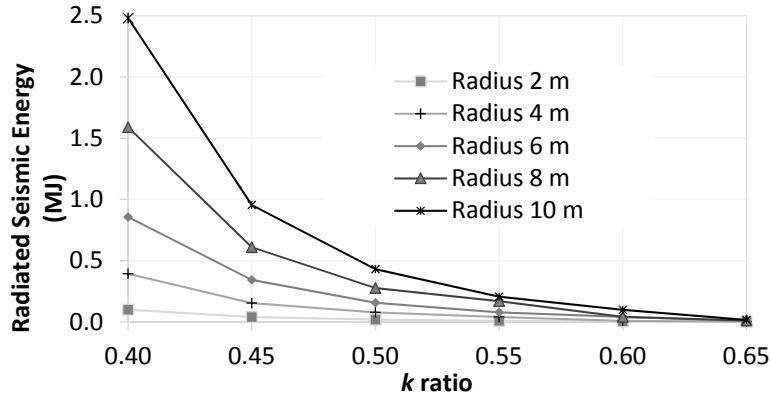


Figure 2.8 Variations between radiated seismic energy, k ratio and dimension of excavation into semi-brittle rock.

Furthermore, as excavation radius grows, instability occurs in a larger range of k ratios. For smaller excavations, more limited conditions have to exist to trigger an unstable failure. The reason for the increasing trend of the radiated seismic energy as the k ratio reduces is mostly the expansion of the failure zone as confirmed by Figure 2.9.

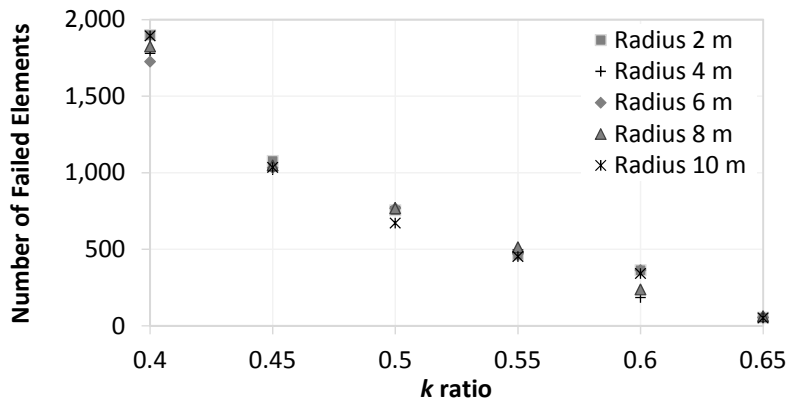


Figure 2.9 Number of failed elements as a function of k ratio and radius of excavations in semi-brittle rock.

Figure 2.9 shows the number of failed elements around the excavation for different k ratios and excavation dimensions while the total number of elements is kept constant between simulations. As mentioned before, we decrease the k ratio by increasing the vertical stresses. Higher initial stresses

expand failure zone further away from the excavation, resulting in the higher number of failed elements in the model. Expanded failure zones then generate higher radiated seismic energy as suggested by Figure 2.8. However, the question is if the extent of the failure zone is the only difference between unstable and stable brittle failures. This is discussed in the next section.

2.6.2 Compressive-type Unstable Failure and Loading System Stiffness

In section 2.4, we showed that loading system stiffness, the GRC slope, which is a function of the material Young's modulus and loading system dimensions, played role in the magnitude of seismic energy radiated by unstable failures. In a circular opening setting, rock mass surrounding the excavation is considered the loading system whose stiffness can be changed by varying Young's modulus of the rock. We conduct a parametric study on variations between the radiated seismic energy magnitude and loading system stiffness by increasing elastic modulus of the rock surrounding the excavation from 10 to 50 GPa. Figure 2.10 suggests impacts of loading system stiffness and excavation span on the magnitude of radiated seismic energy while the *k ratio* is kept constant at 0.45.

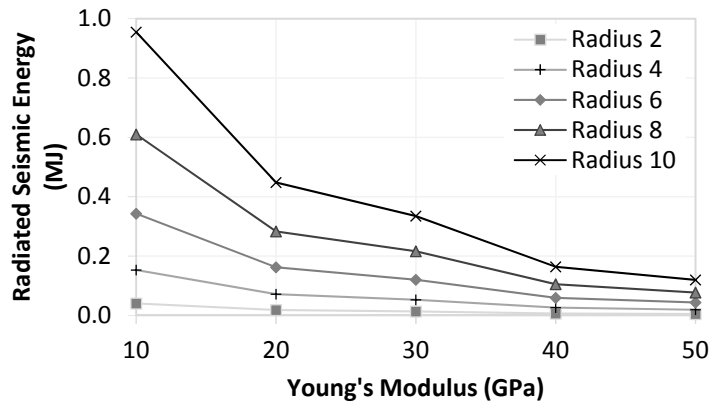


Figure 2.10 Variations between loading system stiffness and radiated seismic energy in the excavation into semi-brittle rock.

In the excavation with a radius of 10 m, increasing Young's modulus by 400% reduces radiated seismic energy by about 90% from 0.96 to 0.12 MJ. Effects of the loading system stiffness become less significant when reducing the excavation radius to 2 m, where radiated seismic energy reduces by only 50% from 0.04 to 0.02 kJ when Young's modulus increases from 10 to 50 GPa. Figure 2.10 indicates that with constant initial stresses the radiated seismic energy of induced events varies based on the loading system stiffness values. Therefore, rock strength, initial stresses, and rock brittleness are not the only indicators of unstable failures. Figure 2.11 indicates that varying Young's modulus has little to zero

impacts on the failure zone extent. This figure shows the number of failed elements in the models with increasing Young's modulus.

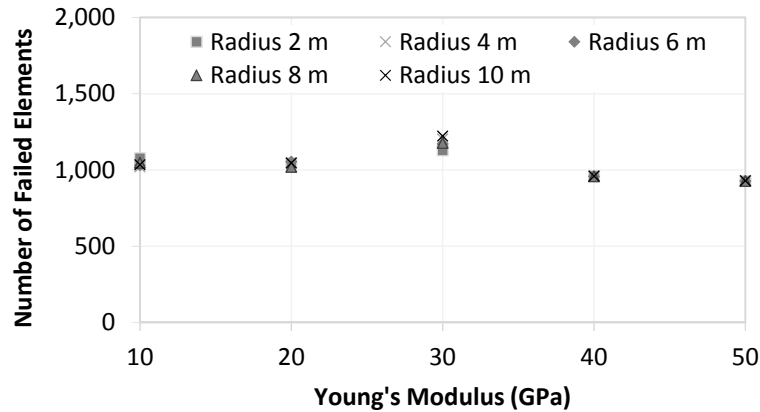


Figure 2.11 Failure zone expansions as a function of loading system stiffness for excavations in semi-brittle rock.

The number of failed zones remains almost constant while Young's modulus varies from 10 to 50 GPa. That is, the failure zone extent is not the reason behind the inverse relationship between Young's modulus of materials and the radiated seismic energy magnitude in Figure 2.10; rather, increasing Young's modulus stiffens the loading system and stabilizes the failure in each failed element. The stabilizing effects of loading system stiffness will be further discussed in chapter 3.

2.7 Circular Opening Advancing Next to a Normal Fault

In the direct shear test in Figure 2.6, the rupture propagated throughout the contact length since the upper block was free to move along the entire contact length. The lateral loading kept generating W that provided energy required for slip even after ΔU was fully exhausted. However, in geologic scales, the rupture propagation is mostly limited to the part of the fault affected by induced stresses. Once initiated, rupture is mostly driven by ΔU and is then arrested when ΔU is exhausted because W cannot provide enough energy to rupture fractions of the fault that are far away from the affected zone. The goal of this section is to trigger the rupture along a fraction of a fault so that the rupture is self-propagated and then is terminated once ΔU is fully consumed. We trigger the rupture along a normal fault with slip-weakening characteristics by excavating a circular opening with the configuration shown in Figure 2.12. This figure shows a cross-section across the 70-degree-dipped fault and the opening. The model is large enough that the rupture in the center does not trigger slip at the ends and thus ΔU mainly governs the rupture propagation.

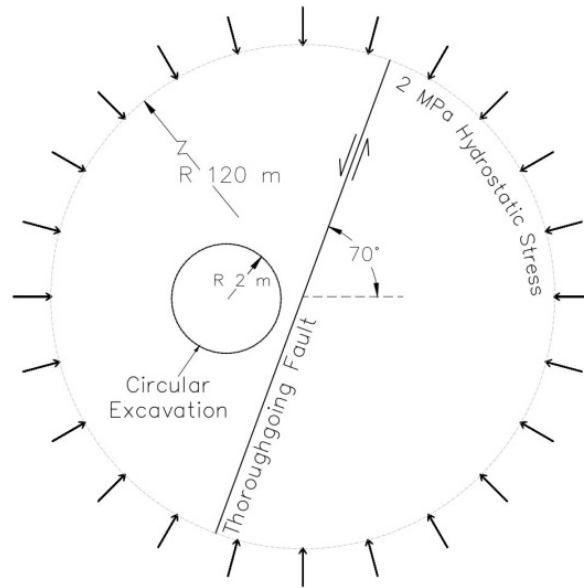


Figure 2.12 Zoom-in view of the circular excavation of radius 2 m next to the fault.

The external radius, loading conditions, and elastic material properties are the same as the model in Figure 2.2. The fault frictional properties follow the characteristics assigned to the contact in the direct shear test in Figure 2.6. We explore variations in the intensity of unstable slip failures, excavation radius, *k ratio*, and loading system stiffness. Excavation dimension is expected to have a direct relationship with radiated seismic energy while *k ratio* and loading system stiffness should be inversely related to the event intensity. During the parametric tests, the minimum distance between the fault and excavation, fault orientation, and fault characteristics remain constant. For simulating gradual excavation, the same controlled unloading procedure as discussed in 2.6 is adopted.

2.7.1 Shear-type Unstable Failure and *k Ratio*

Studying *k ratio* can help understand the mechanism of the elevated event intensity observed in deep excavations (Salamon, 1983). The fault in Figure 2.12 is activated under in-situ stresses with a *k ratio* ranging from 0.45 to 1. Figure 2.13 depicts changes in radiated seismic energy as a function of *k ratios* and excavation dimensions. The results are shown for *k ratios* between 0.45 and 0.65 since insignificant changes occur beyond 0.65. The trend for the 10 m radius excavation shows that radiated seismic energy reduces from 10 to 1.5 kJ by increasing *k ratio* from 0.45 to 0.65. As the excavation radius shrinks the seismic event intensity reduces over different values of *k ratio*. However, significant seismic energy release can still occur in small excavations if *k ratio* is low enough, creating high deviatoric stresses. Figure 2.14 can explain the reason behind the increase in the energy radiated from the fault with decreasing *k ratio* and increasing excavation radius.

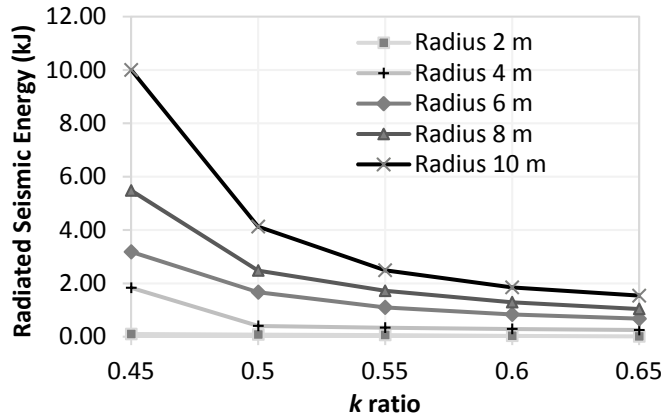


Figure 2.13 Relation between the radiated seismic energy, excavation radius and *K ratio* for a tunnel next to a brittle fault.

Figure 2.14 indicates relationships between excavation dimensions, *k ratios*, and rupture lengths. The length of a fault that experiences rupture is called rupture length. Given the orientation of the fault shown in Figure 2.12, excavation reduces the normal stresses acting on the fault. The reduction in the normal stress initiates a local rupture along the part of the fault that is located in the closest proximity to the excavation. The initial local rupture increases the shear stress on the neighboring unruptured parts and further propagates the rupture if the fault shear strength is less than the elevated shear stress.

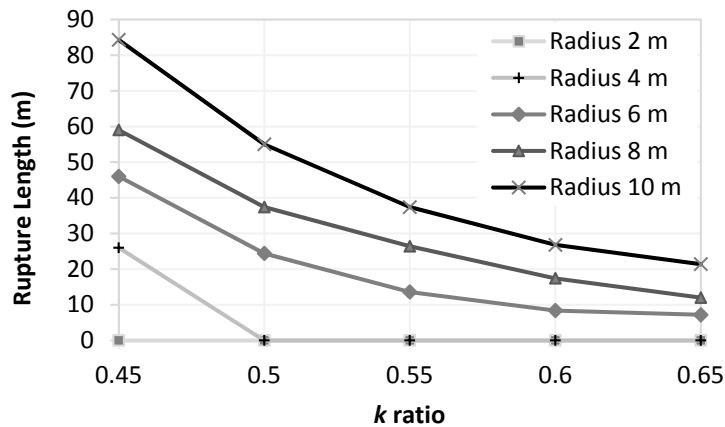


Figure 2.14 Variation of the rupture length along the fault with the *k ratio* and excavation size.

As shown in Figure 2.14, at a constant *k ratio* of 0.45, the rupture length decreases from 84 m to 0 when excavation radius decreases from 10 to 2 m. This is because a larger excavation causes a higher drop in the fault confinement, expands the affected zone on the fault, and propagates the rupture farther away from the initiation point. Comparing Figures 2.13 and 2.14, it can be inferred that the rupture length

expansion can be the root cause of the increase in radiated seismic energy in Figure 2.13. This is because lower k ratios provide higher deviatoric stresses, meaning initial shear stresses along the fault are higher, bringing more fraction of the fault close to the brink of failure. However, the question is if the rupture expansion is the only difference between unstable and stable slip events.

2.7.2 Shear-type Unstable Failure and Loading System Stiffness

In section 2.7.1, we showed that the k ratio is inversely related to radiated seismic energy because k ratio expands the rupture length along the fault. Another parametric study is performed to observe the dependence of radiated seismic energy on the stability of slip. For doing so, we keep the k ratio constant at 0.45 and change the loading system stiffness by varying Young's modulus of the rock surrounding the fault from 10 to 50 GPa.

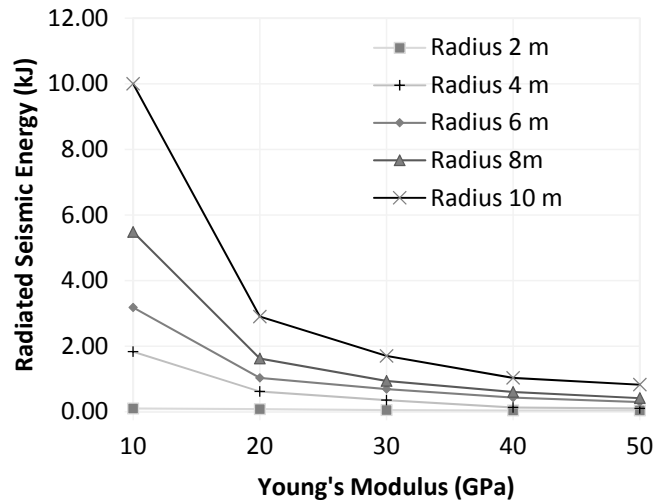


Figure 2.15 Relationships between radiated seismic energy, excavation radius, and Young's modulus when excavating the opening next to a slip-weakening fault.

Effects of loading system stiffness on the slip stability are shown in Figure 2.15 where radiated seismic energy drops to zero as the loading system stiffness increases. Consistent with the previous results, in the case of smaller excavations, the degree of instability decreases. Figure 2.16 implies the root cause of the increase in radiated seismic energy with increasing excavation size, and reducing loading system stiffnesses.

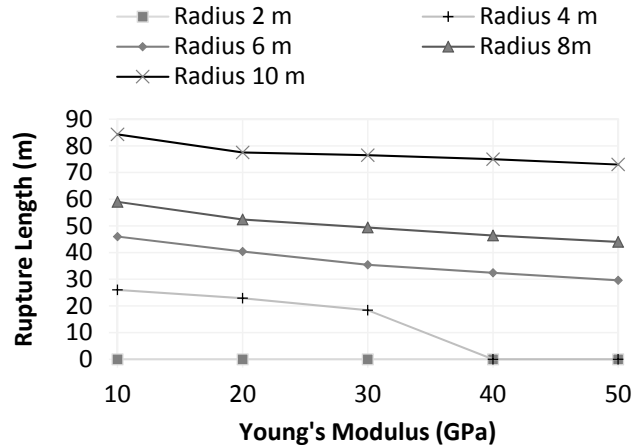


Figure 2.16 Variations between loading system stiffness and the length of rupture triggered by the circular excavation.

The rupture length in Figure 2.16 stays almost constant at about 80, 50, 20 m for excavations with radii 10, 8, 6, 4 m, respectively. This shows increasing Young's modulus has little to no effects on the rupture length and thus the variation of radiated seismic energy in Figure 2.15 is a result of the change in the stability of slip along a constant rupture length. Although the fault response is still slip-weakening, stable slip occurs with high Young's modulus since $W - \Delta U$ is not enough to exceed W_p and to cause significant radiation of seismic energy. This confirms that slip-weakening behaviors and high initial stresses on the fault cannot be the sole conditions required for a rupture but the loading system stiffness should be also taken into account.

2.8 Discussion

A computational framework is developed by presenting methodologies and modeling approaches. The framework is capable of identifying unstable failures when they occur and quantify the intensity of induced events. A series of validation tests are conducted using the distinct element software UDEC to compare static and dynamic energy components with analytical solutions during the formation of simple excavation geometries. Circular excavations in rock with semi-brittle strength characteristics are studied over a range of *in-situ* conditions. The results confirm that once conditions for instability emerge, larger excavations in the rock loaded by a lower *k ratio* lead to a larger damaged zone, yielding a higher value of radiated seismic energy. By varying elastic modulus of the rock in this case, we show that the loading system stiffness controls the stability of a compressive failure without affecting the damaged zone.

We simulated fault slip triggered by a tunnel being driven through elastic ground near the fault. A series of parametric tests explore the influence of excavation size, *k ratio*, and stiffness of the surrounding

rock on radiated seismic energy magnitudes. We show that larger excavations with lower k ratios expand the rupture length, resulting in radiating higher-magnitude seismic energy if conditions of instability emerge. Loading system stiffness controls the slip instability with no effects on the rupture length. That is, decreasing loading stiffness in a fault system increases the radiated seismic energy while the rupture length is still almost the same. In all tests, smaller excavations with stiffer rock require more extreme conditions to trigger an unstable failure.

Studying both compressive- and shear-type mechanisms of unstable failures, it was inferred that the maximum radiation of seismic energy in the former was 1 MJ while that of the latter was only 10 kJ. This implies that the compressive-type unstable failures may result in higher damage in a circular opening configuration. This is consistent with field observations as reported by many researchers (Martin et al., 1999; Ortlepp and Stacey, 1994). The framework presented here demonstrates the ability to directly calculate the seismic energy radiated in potentially complex failure processes. The energy calculation techniques can be applied to a variety of underground excavations to determine burst-prone segments and to approximate magnitudes of seismic energy radiated if unstable failure conditions emerge. Using the framework for calculating radiated seismic energy magnitude as a representative of seismic event intensity helps prevent overestimating or underestimating effects of unstable failures on the progress of an underground project. Estimating the seismic energy radiated due to possible unstable failures can also help design energy-absorbing support systems as a burst-mitigating strategy in an underground excavation (Ortlepp and Stacey, 1994).

2.9 Conclusions

We study notions of instability in compression and shear and applied them to developing a computational framework for investigating unstable failures. We show the complexity of the problem of instability and exemplify situations where using empirical criteria could result in unrealistic estimates of the failure intensity. For instance, we show that brittle failure of rock under high stresses may not necessarily lead to an unstable crushing of the rock around an excavation if the loading stiffness is high enough. Also, high in-situ stresses may not be also necessary for triggering an unstable failure if the stiffness of the loading system is low enough. This chapter suggests that the expression of unstable failures can be due to different combinations of rock brittleness, in-situ stresses, loading system stiffness, rock compressive strength, fault slip-weakening behaviors, the extent of the damaged zone, and excavation geometry. Although these combinations can vary between different excavation layouts, a significant radiation of seismic energy stays as a common signature for all unstable failures triggered by the different combinations. This is the main advantage of the developed framework as it does not rely on

only, for examples, the extent of the damaged zone or rock brittleness for assessing the possibility and magnitude of unstable failures. We show that stress analyses for examining the likelihood of unstable failures require a detailed interpretation of the result, causing unnecessary complications. We suggested calculations of seismic energy instead of analyzing stresses for assessing potential induced seismic events. Once more reliably estimated during exploration stage of an underground facility project, the expected event intensity can help adopt more cost-effective and safer strategies for reducing possible damages.

2.10 References

- Andrews, D.J., 1976. Rupture velocity of plane strain shear cracks. *J. Geophys. Res.* 81, 5679–5687. <https://doi.org/10.1029/JB081i032p05679>
- Bolghonabai, R., Hossaini, M.F., Mohammadi, M., Nazem, A., 2015. On the selection of an appropriate excavation pattern for urban tunnels with big cross-section: A case study. *Univ. Tehran Fac. Eng.* 49, 297–307. <https://doi.org/10.22059/IJMGE.2015.56116>
- Cook, N.G.W., 1966a. The design of underground excavations, in: Eighth Symposium on Rock Mechanics, University of Minnesota, in Failure and Breakage of Rock. pp. 167–193.
- Cook, N.G.W., 1966b. Rock mechanics applied to study of rockbursts. *J. South African Inst. Min. Metall.* 66, 435–528.
- Cook, N.G.W., 1965. A note on rockbursts considered as a problem of stability. *J. South African Inst. Min. Metall.* 65, 437–446.
- Cundall, A.P., 1987. Distinct element models of rock and soil structure. *Anal. Comput. Methods Eng. Rock Mech.* 129–163.
- Cundall, P.A., Lemos, J., 1990. Rockbursts and seismicity in mines, in: Numerical Simulation of Fault Instabilities with the Continuously-Yielding Joint Model. pp. 379–387.
- Dammyr, Ø., 2016. Prediction of brittle failure for TBM tunnels in anisotropic rock: A case study from Northern Norway. *Rock Mech. Rock Eng.* 49, 2131–2153. <https://doi.org/10.1007/s00603-015-0910-z>
- Diederichs, M.S., 2007. The 2003 Canadian Geotechnical Colloquium: Mechanistic interpretation and practical application of damage and spalling prediction criteria for deep tunnelling. *Can. Geotech. J.* 44, 1082–1116. <https://doi.org/10.1139/T07-033>
- Dieterich, J.H., 1979. Modeling of rock friction: 1. Experimental results and constitutive equations. *J. Geophys. Res.* 84, 2161. <https://doi.org/10.1029/JB084iB05p02161>
- Duvall, W.I., Stephenson, D.E., 1965. Seismic energy available from rockbursts and underground explosions. *Trans. Soc. Min. Eng.* 232, 235–240.
- Fang, Y., He, C., Nazem, A., Yao, Z., Grasmick, J., 2017. Surface settlement prediction for EPB shield tunneling in sandy ground. *KSCE J. Civ. Eng.* 21, 2908–2918. <https://doi.org/10.1007/s12205-017-0989-8>.
- Ghavidel, N.A., Nazem, A., Heidari-zadeh, M., Moosavi, M., Memarian, H., 2014. Identification of Rheological Behavior of Salt Rock at Elevated Temperature, Case Study: Gachsaran Evaporative Formation, Iran, in: ISRM Regional Symposium - EUROCK. International Society for Rock Mechanics and Rock Engineering, Vigo, Spain, pp. 26–28.
- Itasca, 2016. Background - The 2D Distinct Element Method, UDEC Manual.

- Madariaga, R., Olsen, K., Archuleta, R., 1998. Modeling dynamic rupture in a 3D earthquake fault model. *Bull. Seismol. Soc. Am.* 88, 1182–1197.
- Martin, C.D., Christiansson, R., 2009. Estimating the potential for spalling around a deep nuclear waste repository in crystalline rock. *Int. J. Rock Mech. Min. Sci.* 46, 219–228. <https://doi.org/10.1016/J.IJRMMS.2008.03.001>
- Martin, C.D., Kaiser, P.K., McCreath, D.R., 1999. Hoek–Brown parameters for predicting the depth of brittle failure around tunnels. *Can. Geotech. J.* 36, 136–151.
- Ortlepp, W.D., Stacey, T.R., 1994. Rockburst mechanisms in tunnels and shafts. *Tunneling Undergr. Sp. Technol.* 9, 59–65.
- Rice, J.R., 1983. Constitutive relations for fault slip and earthquake instabilities. *Pure Appl. Geophys.* 121, 443–475. <https://doi.org/10.1007/BF02590151>
- Salamon, M.D.G., 1984. Energy considerations in rock mechanics: fundamental results 84, 233–246.
- Salamon, M.D.G., 1974. Rock mechanics of underground excavations. *Advances in Rock Mechanics*, in: 3rd Cong Int Soc Rock Mech. pp. 951–1099.
- Salamon, M.D.G., 1970. Stability, instability and design of pillar workings. *Int. J. Rock Mech. Min. Sci.* 7, 613–631. [https://doi.org/10.1016/0148-9062\(70\)90022-7](https://doi.org/10.1016/0148-9062(70)90022-7)
- Salamon, M.D.G., 1968. Two-dimensional treatment of problems arising from mining tabular deposits in isotropic or transversely isotropic ground. *Int. J. Rock Mech. Min. Sci. Geomech. Abstr.* 5, 159–185. [https://doi.org/10.1016/0148-9062\(68\)90032-6](https://doi.org/10.1016/0148-9062(68)90032-6)
- Salamon M. D. G., 1983. Rockburst hazard and the fight for its alleviation in South African gold mines’, in: *Rockbursts Prediction and Control*. London, pp. 11–36.

CHAPTER 3

MODELING ROCK BURST IN SHEAR AND COMPRESSION THROUGH SEISMIC ENERGY CALCULATION

A paper submitted to the *International Journal of Rock Mechanics and Mining Science*

Zoheir Khademian and Ugur Ozbay

3.1 Abstract

This chapter presents results from a series of numerical modeling studies conducted with the objective of extending the developed framework to simulating rock burst events (aka unstable failures, violent rock failures) in underground mining. UDEC, a commercially available distinct element code with its explicit, yet quasi-static time-stepping scheme is adopted for the failure instability modeling studies. The radiated seismic energy is calculated to identify rock burst conditions as they emerge. A rectangular tabular excavation supported by a single pillar is modeled with ductile, semi-brittle, and brittle responses during failure of the pillar under compressive loading. The elastic modulus of the rock mass is varied between simulations to evaluate the effect of loading system stiffness on the level of instability experienced by the pillar during its loading. The brittle pillar response yields the most unstable failure, radiating seismic energy magnitudes within 0.7% of graphically obtained values. A shear-type rock burst (rupture) along a strike-slip fault is simulated by considering the average slip, rupture length, radiated seismic energy, and the seismic moment that are found within 6% error against the analytical results. For both compressive and shear slip cases of rock burst events, the study shows that elastic modulus of the rock, stress drop magnitudes, fault frictional properties, and rock brittleness govern the failure stability. The methodology and modeling approaches discussed here further improve the framework developed in chapter 2 for studying rock burst events generated in a variety of mining excavation settings.

3.2 Introduction

Rock burst events are unstable rock failures induced by excavation advances underground. In a stable failure, the process of failure is gradual allowing for arresting the failure by, for example, ceasing to enlarge the area of mining, therefore, the workings are essentially stable. Unstable failure takes place suddenly with or without prior warning (Salamon, 1970). Unstable failures are a risk to the miners, especially in pillar workings, and the productivity of the mining operation. Predicting unstable failures are

a challenge because of their complex mechanisms, variations in rock material properties and complexity in mining layouts. Commonly, unstable events are treated under two categories (Cook, 1966a), one is the crushing of the highly stressed volume of rock in compression, usually with anomalous seismic signatures, and the other is unstable shear slip along mostly through-running large weakness planes such as faults and dyke contacts with typical earthquake-like seismic signatures (Joughin, N C; Jager, 1983; Salamon, 1970; Stiller, H., Hurtig, E., Grosser, H., and Knoll, 1983; Van der Heever, 1984).

3.2.1 Compressive-type Rock burst

Cook (1965) first posed the problem of rock burst theoretically as an issue of equilibrium instability. In the laboratory, Wawersik and Fairhurst (1970) demonstrated that the failure instability depends on the descending post-peak behaviors and the stiffness of the compressive testing machine (loading system). The behavior of rock after exceeding its peak strength on the load-displacement curve is called post-peak behavior. Cook (1965) showed that once a brittle rock is under compressive loading, an increase in strain is associated with an increase in the resistance of the rock during the unfailed state. In the failing regime, after reaching the maximum stress values in compression, a further increase in compressive displacement is accompanied by a decrease in rock resistance. The post-peak behavior in brittle rocks is usually accompanied by a localized deformation along shear bands within the pillar (Zubelewicz and Morz, 1983). Laboratory experiments showed when the loading system stiffness is soft as compared to the rock's post-peak slope then the failure is unstable followed by the sudden release of energy stored in the loading system. This energy is mostly released in the form of kinetic energy and is called radiated seismic energy. When the loading system is stiff compared to the post-peak slope, failure remains stable as the failing rock is able to absorb the energy released from the loading system.

Salamon (1970) and then Petukhovt and Linkov (1979) discussed generalizing the simple mechanism of the laboratory test to the mining situation. Salamon (1970) showed that loading system stiffness in mining settings changes with increasing pillar panel length. Starfield and Fairhurst (1968) suggested that the system stiffness can be tested by hypothetically replacing the pillar with a jack. Salamon (1970) provided process for defining the varying loading system stiffness as a result of advancing mining and numerically modelled brittle pillar failure through substituting pillars by equivalent forces that decay as failure occurs, simulating post-peak behaviors. It was proved that the workings will remain stable, regardless of the magnitude of the convergence experienced by the pillars, if the post-peak slope of the pillar load-convergence relations is greater than the loading system stiffness.

More closely related to the approach used in this chapter, Zubelewicz and Morz (1983) numerically studied the instability conditions and the modes of failure of several pillars using dynamic approach in finite element discretization. Following the same approach, Garvey and Ozbay (2013) studied compressive-type instability in a pillar modeled by finite difference elements. The results from these tests indicate that radiated seismic energy may be used as a direct assessment of the seismic potential of simulated mine layouts. They estimated the radiated seismic energy by tracking energy terms during the failure process.

3.2.2 Shear-type rock burst

Elevation of the shear stresses on a pre-existing fracture can be a result of the stress re-distribution caused by mining operations. The re-distributed stress may exceed the shear strength of the weakness plane and induce a shear slip that can be unstable or stable. Pre-existing large fault structures around mine workings behave differently in response to the stress re-distribution and compared to compressive-type rock burst can generate larger scale damage to underground excavations (Napier and Malan, 1997).

Dieterich (1979) and then Rice (1983) used a mass-spring system with one degree of freedom and discussed unstable shear slip as a problem of equilibrium instability. They confirmed that, if the post-peak slope of the contact shear force-displacement curve stays greater than the spring stiffness, unstable slip occurs with a sign of significant oscillation in the spring. This means the seismological slip-weakening response of a fracture to shear loading is necessary for instability as it corresponds to the descending part of the load-shear displacement curve.

Salamon (1993) and then Linkov (2005) used the concept of shear failure instability in the mass-spring systems and proposed a procedure for assessing seismic potentials by generating fractures with random length around mine workings. They also provided solutions for calculating seismic energy radiated from an unstable shear failure. The stress drop on the fractures is calculated when the mine excavations are enlarged in progressive steps. The instability is based on possible slip along fractures in elastic rock and the instability criteria that depend on the stiffness of the loading system and post peak slope. Stiffness is calculated based on the joint length and shear modulus of elastic rock. Since joint length is defined as a special case of Weibull distribution, the loading system stiffness and thus instability of slip on each fracture depends on the prescribed distribution function. This limits the application of these methods in simulating slip on a limited part of a large fault activated partially by mining operations. In the case of partial slip on a fault, loading system stiffness depends on the slip length (rupture length)

that grows progressively from an initiation point and propagates along the fault until equilibrium is regained. Therefore, simulating shear-type rock burst on preexisting large plane of weakness remains as a challenge because they can be the source of great-magnitude events with an earthquake-like seismic signature. Gu and Ozbay (2014) discussed the possibility of using discontinuum numerical techniques in simulating mining-induced fault slip. They modeled a horizontal discontinuity above an advancing tabular excavation and simulated unstable slip identified by a significant radiation of seismic energy. However, calibrating the models and verifying the calculated seismic energy were left to future studies.

This chapter presents a calibrated computational framework and shows its capability in simulating both shear- and compressive-type rock burst and study their interactions. The modeling approach and methodology are developed for generalizing the concept of instability in compression and shear to mining configuration using the commercially available distinct element code UDEC (Itasca, 2016). UDEC is based on a discontinuum analysis technique where rock mass is an assembly of blocks divided by joints. The deformable blocks are discretized into finite difference elements and the interaction between blocks is calculated by distinct element techniques. This numerical configuration allows simulating non-linear behavior in shear along discontinuities and non-linear failure of rock in compression.

This chapter constructs idealized models to explore the concept, calibrates modeling approach, and verifies results against analytical solutions. A mining tabular excavation supported by a single mine pillar is modelled and stability of pillar failure is explored with three post-peak responses to stress, namely brittle, semi-brittle, and ductile behaviors under different loading system stiffness. The failure stability of the pillar in each case is discussed and the failure intensity is measured by the magnitude of radiated seismic energy. The rupture mechanism along a discontinuity is examined through a numerical direct shear test and the results are verified against the instability magnitudes given by Salamon (1970). The same approach is extended to model a strike-slip fault where loading conditions, rupture area, stress drop, kinetic energy, and seismic moment are compared against the analytical solutions provided by Ryder (1988). For the sake of framework development, the fault is activated by an increasing shear force on the fault. Given the verification process, mining excavation can be modelled for exploring mining-induced slip on the fault.

Numerical procedure for simulating compressive- and shear-type rock burst are divided into two main parts: quasi-static loading until the point of failure and dynamic approach for simulating unstable failures until the system regain equilibrium. Two methods for estimating the radiated seismic energy as a measure for occurrence and magnitudes of induced seismicity: dynamic calculation of kinetic energy that

needs to be damped for bringing back the unstable failure to equilibrium; Tracking the transfer of energy during a failure and estimating the energy that radiates if conditions for instability emerge. We compare radiated seismic energy calculated from these methods for both compressive-and shear type rock burst. Since there is no need for analytically calculating or prescribing the loading system stiffness, the developed framework is capable of simulating complex mining layouts in different geologic settings.

3.3 Energy Balance

Failure in rocks surrounding excavation results in the transfer of energy within the rock mass. The external work (W) done by the external forces and the initial strain energy (U_i) stored in the rock mainly drive a failure process. Gravitational forces, tectonic loadings, and stresses induced by an underground opening are examples of external forces acting on a rock mass. The strain energy is accumulated in the rock due to the steady deformation generated by the external loading. Once failure initiates, the release of the accumulated strain energy, as well as the work done by the active external forces, are the energy available for governing the failure that results in dissipative energy terms of plastic work (W_p) and radiated seismic energy (W_k).

Plastic work represents the inelastic deformation of rock and shear displacements along a pre-existing fault. Seismic energy radiates from the system once the available energy is not fully consumed by the plastic work (Salamon, 1984). Unstable failures do not necessarily lead to a full exhaustion of the strain energy stored in the system and, therefore, residual strain energy (U_r) may remain in the system (Brune, 1970). Equation 3.1 is an energy balance that summarizes the transfer of energy. The left- and right-hand sides of Equation 3.1 belong to the state of energy within the system before and after a failure, respectively.

$$W + U_i = W_p + U_r + W_k \quad (3.1)$$

Equation 3.1 can be rearranged to directly calculate seismic energy radiated during failure, W_k as:

$$W_k = W + \Delta U - W_p \quad (3.2)$$

where ΔU is the release of the strain energy of the rock ($U_i - U_r$) as the failure progresses. The distinct element method in UDEC uses a quasi-static scheme for reaching a solution of static equilibrium. The method damps a fraction of the kinetic energy of the system at each time step through the application of damping forces which depends on a damping constant and is proportion to the unbalanced forces exhibited at each grid point. A damping constant of 0.8 is selected based on a calibration process

performed in chapter 4. The cumulative damped work for all time steps is recorded as W_d . At each time step, the system keeps a portion of kinetic energy U_k that approaches zero as the model reaches equilibrium and is high during peak dynamic response (Poeck et al., 2016). The energy balance based on the seismic terms in the numerical solver is governed by the relation in Equation 3.3 (Itasca, 2016).

$$W_k = U_k + W_d \quad (3.3)$$

In Equation 3.3, U_k is the kinetic energy that remains in the system at the end of the simulation. In chapter 2, the static and dynamic calculations of radiated seismic energy in the developed framework were verified against analytic solutions provided by Duvall and Stephenson (1965), Salamon (1984), and Cook (1966b). It was also shown that Equations 3.2 and 3.3 yield the same results for the magnitude of radiated seismic energy. Here, the same approach is extended to include failure of a support pillar in compression and a shear slip along a pre-existing, strike-slip fault.

3.4 Unstable Compressive Failures

A single pillar model in a uniform loading condition is developed in UDEC to assess the ability of this developed framework in simulating brittleness as well as the role of brittleness and loading system stiffness in pillar failure stability. Figure 3.1 outlines a schematic view of the single pillar model and the loading condition. The model is loaded to 2 MPa hydrostatic stresses.

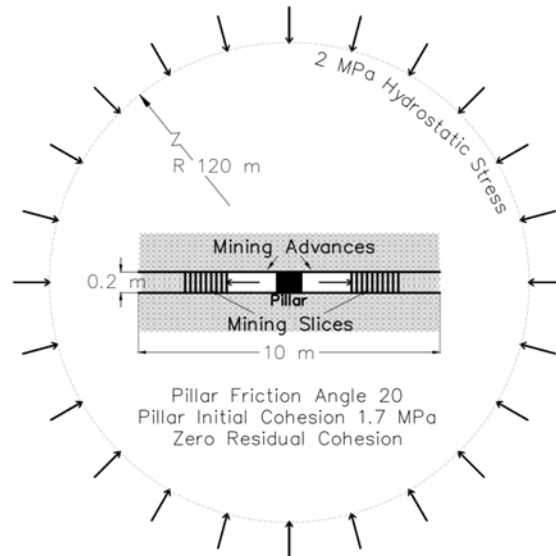


Figure 3.1 Schematic view of the tabular excavation with the pillar and mining slices in UDEC. The radius of the circular external boundary is 200 m. The pillar is 0.2 m high and 0.2 m wide.

One 5 cm mining slice from each entry is then removed and the model is allowed to reach equilibrium at each interval. As the excavation advances, the stress on the pillar increases until its peak compressive strength is reached once the Eighth slices are removed from both entries. The next section explains how the post-peak behavior of the pillar and the loading system stiffness control the stability of the pillar failure.

3.4.1 Brittle, Semi-brittle, and Ductile Model Responses

For verifying the numerical energy calculation, the brittle response is not explicitly simulated in UDEC; instead, the load bearing capability of the pillar is suddenly decreased to zero by removing the pillar once loaded to its peak strength. The stress drops vertically to zero, so no plastic work is consumed. The semi-brittle behavior is simulated by assigning the Mohr-Coulomb Strain-Softening (MCSS) constitutive model to the pillar while the fully ductile response is represented by an elastoplastic Mohr-Coulomb model. The principle of MCSS was detailed in chapter 1. Table 3.1 lists geomechanical properties for each case of the pillar failure. With excavating each slice, the roof and floor gradually converge and impose higher compressional loads on the pillar. In this configuration, the pillar’s roof and floor play the role of the loading system.

Table 3.1 Geomechanical Properties of Materials and Constitutive Laws for Simulating the Single Pillar Model.

Type	Constitutive Law	Young Modulus	Poisson’s Ratio	Peak Friction angle	Residual Friction angle	Initial Cohesion	Residual Cohesion
Pillar	Brittle	10 GPa	0.2	Sudden removal of the pillar			
	Semi Brittle	10 GPa	0.2	20 °	20 °	1.7 MPa	0.0
	Ductile	10 GPa	0.2	20 °	20 °	N/A	N/A
Surrounding Rock	Elastic	10 GPa	0.2	N/A	N/A	N/A	N/A

The average vertical stress within the pillar and the convergence (vertical closure) induced by the horizontally expanding excavation are recorded for brittle, semi-brittle, and ductile pillar behaviors. The red solid curve in Figure 3.2 shows the vertical stress-convergence curve (failure curve) for the ductile response of the pillar. The solid black and gray curves correspond to the brittle and semi-brittle failure curves, respectively.

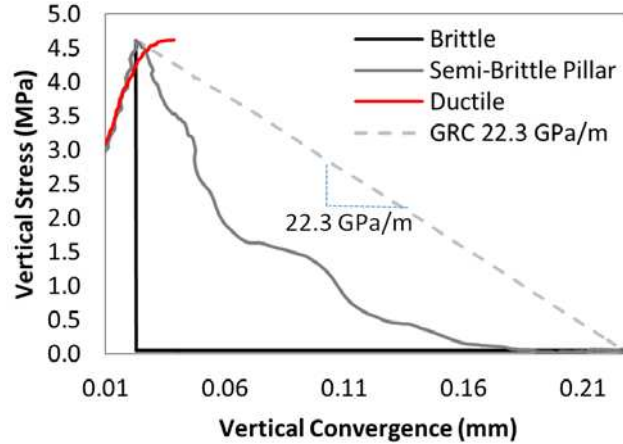


Figure 3.2 Stress-convergence or failure curves for ductile (red curve), semi-brittle (gray curve), and brittle (black curve) behaviors of the pillar. The dashed line is the GRC for the brittle and semi-brittle responses. The GRC for the ductile failure follows the ductile failure curve.

Stresses within the loading system change as the pillar failure progresses and causes the convergence. We define the relationship between the stresses within the loading system and the convergence as the Ground Reaction Curve (GRC). The GRC for each pillar response is obtained by recording the average vertical stresses acting on the pillar during the failure process. For the semi-brittle and brittle responses, the pillar strength reduces to zero after failure, suggesting the highest roof-floor convergence. The recorded ground reactions to the semi-brittle and brittle pillar failures are shown by the dashed line in Figure 3.2. The GRC for the ductile pillar failure matches the pillar failure curve. The ductile pillar offers much less convergence than brittle pillars. This is because once failed, the ductile pillar maintains the same load as it converges through the plastic deformation. When excavation is stopped, the plastic movement is prevented due to the constant load bearing capacity of the ductile pillar.

The area below the GRC is the energy density available for failure ($W + \Delta U$). Once failed, the area below the pillar failure curve represents the plastic work density W_p which is performed by the pillar during failure. Referring to Equation 3.2, the gap between the post-peak failure curves and GRC yields the radiated seismic energy per unit cross-sectional area of the pillar W_k . Figure 3.3 shows the radiated seismic energy magnitudes obtained from graphical (based on Equation 3.2) and dynamic calculations (based on Equation 3.3) for three post-peak behaviors. The largest event is attributed to the brittle response with a 105.5 J seismic energy radiation, which is within a 0.4% error of the graphical calculation of the gap between the pillar post-peak failure curve and the corresponding GRC, multiplied by the pillar cross section area of 0.2 m².

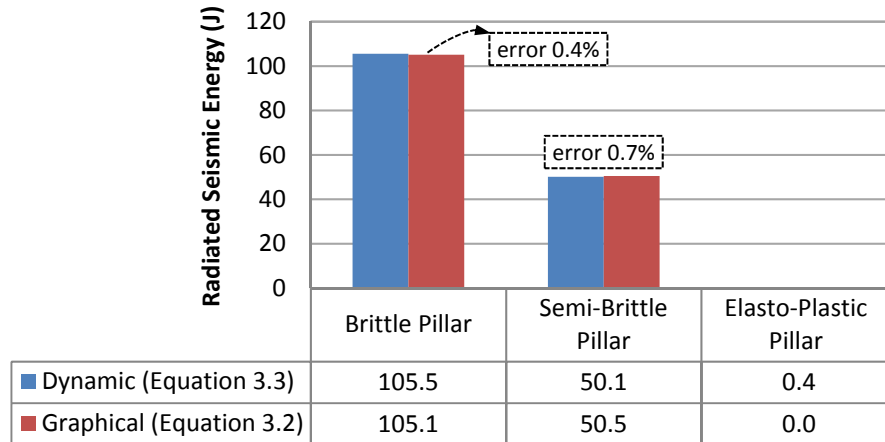


Figure 3.3 Graphical and numerical calculations of the seismic energy radiated due to three different pillar responses.

In Figure 3.2, the GRC for the ductile pillar response closely follows the ductile failure curve, thus near-zero seismic energy radiation is expected. Ductile failure radiates near-zero energy since the failure does not propagate autonomously and thus requires an external force in order to continue failing; however, it records 0.4 J of radiated seismic energy caused by the small dynamic effects introduced through the simulated excavation procedure. With 50.1 J and 50.5 J seismic energy radiation calculated by the dynamic and graphical methods, respectively, the result of the semi-brittle failure falls between the two extremes of the brittle behaviors. The main source of the error can be attributed to the dynamic effects caused by the removal of the mining slices.

3.4.2 Loading System Stiffness

Jaeger and Cook (1976) and Goodman and Sundaram (1978) argued that the slope of GRC is dictated by the loading system stiffness. In the case of a tabular excavation, the loading system stiffness is in inverse relation to the width of the excavation span and in direct relation to Young’s modulus of the material surrounding the pillar. In order to capture further insight on the GRCs and pillar failure curves, we conduct a series of parametric studies on the loading system stiffness through varying Young’s modulus of the rock surrounding the semi-brittle pillar. Figure 3.4 shows the pillar responses to loading through three different stiffness values.

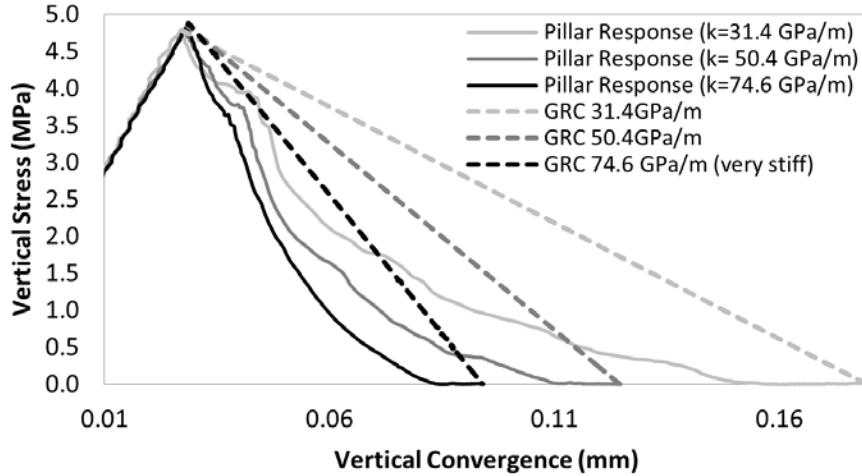


Figure 3.4 Parametric study on the effects of the loading system stiffness on the magnitude of the radiated seismic energy from the semi-brittle pillar failure.

Assigning Young’s moduli of 15 GPa, 25 GPa, and 35 GPa to the surrounding rock, while the pillar’s Young modulus is kept constant, yields GRCs with the slopes of 31.4, 50.4, and 74.6 GPa/m, respectively. For each case, the area between the post-failure curve and GRC, multiplied by the contact length is compared with the UDEC results of radiated seismic energy (Figure 3.5). The rock mass with the lowest Young’s modulus suggests the lowest slope of the GRC and should, therefore, result in the highest value of the radiated seismic energy.

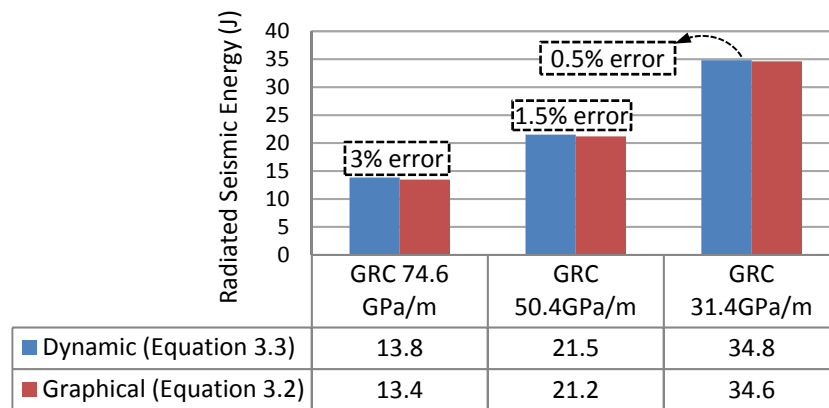


Figure 3.5 Comparison between graphical and numerical calculations of the seismic energy radiated from compressive failures of the mining pillar under three different loading stiffness values.

With a 0.5% error, the dynamic calculations yield 34.8 J of radiated seismic energy for the soft loading system stiffness. As expected, the stiffest loading system with Young’s modulus of 35 GPa and

GRC slope of 74.6 GPa/m corresponds to the lowest radiated seismic energy. The relative consistency between the graphical and numerical results gives credence to the capability of this numerical methodology in capturing the radiated seismic energy in more complex brittle compressional failures as demonstrated by Poeck et al. (2016).

3.5 Unstable Shear Failures

Elevation of the shear stresses on a pre-existing discontinuity can be a result of the stress redistribution caused by natural or human activities. The stress may exceed the shear strength of the weakness plane and induce a failure that can be unstable or stable. Dieterich (1979) and Rice (1983) showed that the seismic energy radiated during an unstable shear slip depends upon the slip-weakening behavior of the fault and stiffness of the loading systems. In slip-weakening constitutive law, slip is near zero until the total stress reaches a peak value where slip starts increasing. Simultaneously shear strength decreases until slip reaches a critical distance called characteristic distance (D_c). After D_c is reached, slip may still continue but under a constant residual stress that equals the residual strength of the fault. Rice (1983) confirmed that, in a box-spring system, if the spring stiffness stays greater than the post-peak slope of the shear force-displacement curve of the box contact, only stable slip can occur along the interface. In the case of a geological fault, the stiffness of the rock mass surrounding the fault plays a significant role in the fault system stiffness that, in return, dictates the magnitude of the strain energy stored and that can be released naturally or by human activities. The partial relaxation of the accumulated strain energy U_i drives a shear slip that can result partly in plastic work W_p and partly in radiated seismic energy W_k . We adopt the numerical direct shear test configuration for investigating the notion of slip instability in an energy framework and then extend the methodology to model rupture on a fault surrounded by elastic rocks.

3.5.1 Fault Slip Model

This section investigates the shear-induced rock burst phenomenon along a pre-existing fault through numerical direct shear test models. Figure 3.6 (left) shows the direct shear test model consisting of two rectangular blocks with each block being 0.15 m high. The upper and lower blocks are 0.2 m and 0.3 m wide, respectively and can be viewed as a simplified representation of the blocks surrounding a fault in a geological setting. Since the upper block can potentially move throughout the interface between the blocks, the interface simulates some fraction of a fault plane.

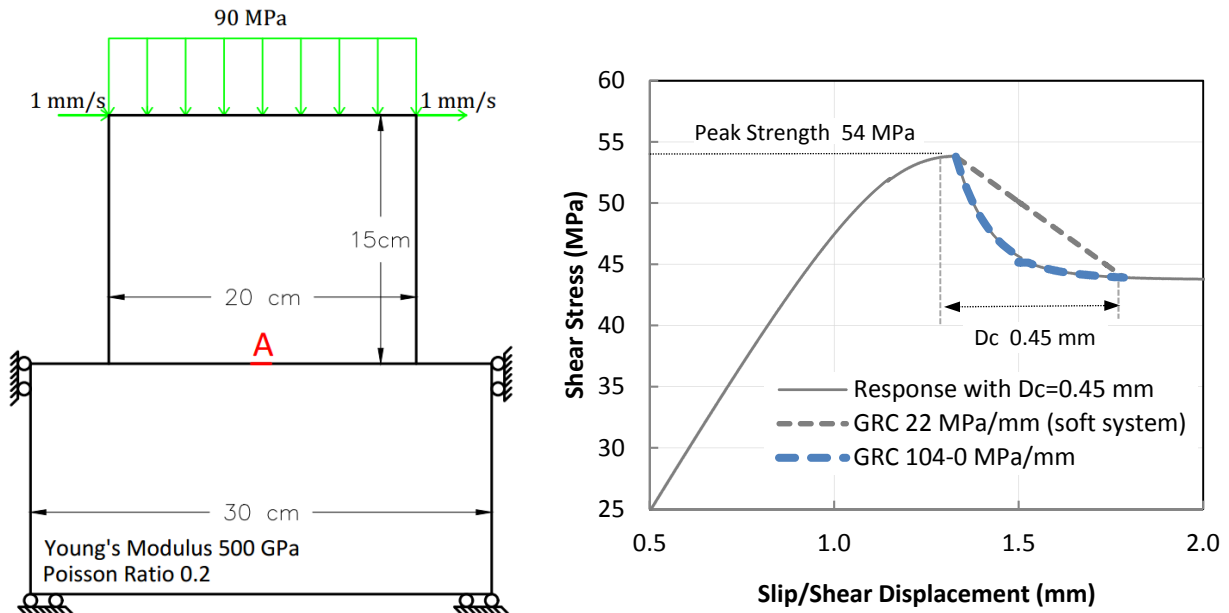


Figure 3.6 Left: Numerical model of the direct shear test in UDEC. Right: Behavior of the discontinuity and loading systems during the slip in the direct shear test. The solid line is the contact shear stress-displacement response recorded at contact A, the dashed blue curve is the GRC of the stiff system with E 40 GPa, and the dashed black line is the soft GRC with E 10 GPa.

Table 3.2 lists the characteristics of a slip-weakening behavior assigned to the interface. The Continuously Yielding (CY) joint model as defined in UDEC is adopted here to simulate the slip-weakening behavior. An initial friction coefficient of 0.6 is assigned to the fault referring to the lower-limit value within fractured rock masses (Barton, Zoback, and Moos, 1995). Due to the quasi-static scheme of the distinct element method in UDEC, both dynamic and residual friction coefficients are assumed identical and equal to 0.49, which falls within most ranges of the reported laboratory observations on residual and dynamic friction coefficients (Beeler, 2001; Lockner and Beeler, 1999; Wong, 2013). Over the upper block, we apply a normal stress of 90 MPa which is based on the assumption of a 3.6 km overburden and rock density of 2550 kg/m³.

Table 3.2 Continuously Yielding Frictional Properties of the Simulated Fault in the Direct Shear Test.

Parameter	Value	Parameter	Value
Joint normal stiffness	50 GPa/m	Joint initial friction coefficient	0.6
Joint shear stiffness	50 GPa/m	Joint roughness parameter	0.1 mm
Joint residual friction coefficient	0.49	Joint Cohesion	0.0 MPa

A constant horizontal velocity of 1 mm/s introduces lateral loading over the upper block and thus develops shear stress on the contact. We record the contact shear stress versus shear displacement (slip) during the shear slip. As shown in Figure 3.6 (left), the normal and lateral loadings develop the external work W that results in the accumulation of the strain energy ($W = U_i$). Once slip occurs, the frictional strength of the brittle contact drops and the upper block snaps back, partially releasing its internal shear stress and deformation, forming the GRC. The GRC is approximated from recording the shear stress within the upper block versus slip over the contact as the failure progresses. The slope of the GRC is dependent on the stiffness of the loading system. The upper block is considered the loading system whose stiffness is in an inverse relationship to the block dimensions and is directly related to Young's modulus of the block (Goodman and Sundaram, 1978; Jaeger and Cook, 1976). Rice (1983) argued that the magnitude of the radiated seismic energy can be quantified by comparing post-peak of fault shear stress-slip curve with GRC. Here, the mechanics of the slip instability proposed by Rice (1983) is examined through running two direct shear tests with two distinct values of Young's moduli assigned to the upper blocks while the lower block is assumed rigid.

The solid line in Figure 3.6 (right) is the shear stress-slip curve recorded along the contact at point A and remains unaffected in both simulations as we assign the same frictional properties to the contacts as listed in Table 3.2. The dashed black line shows a linear GRC with the slope of 22 GPa/m, representing the soft loading system that is modeled by assigning Young modulus of 10 GPa to the upper block. The blue dashed curve shows the GRC for the stiff loading system with Young's modulus of 40 GPa, suggesting a slope decaying exponentially from 104 to 0 GPa/m. This is because energy would be created if GRCs cross the contact stress-slip curve. Therefore, if the loading system stiffness is greater than the post-peak slope of the contact shear stress-slip curve, GRC follows this curve.

The area below the dashed lines in Figure 3.6 (right) denotes the available energy ($W + \Delta U$) which is generated by loading the simulated fault through the soft and stiff systems. The plastic work W_p or the energy consumed throughout the slip can be related to the area below the solid curve in Figure 3.6 (right) after the slip initiation. According to Equation 3.2 and the instability concept, the area between the solid and dashed lines is representative of W_k , the seismic energy which is radiated when the conditions for instability are satisfied. For the case of the stiff loading system, the block rebounds through the same path as the shear slip. The strain energy available from failure is fully consumed by the plastic work and thus, near-zero radiated seismic energy W_k is expected. This is confirmed by the results listed in Table 3.3.

Table 3.3 Comparison between Analytic and Numerical Methods of Calculating the Radiated Seismic Energy for Slip Failure Simulated in the Direct Shear Test.

Loading Stiffness	Radiated seismic energy		Difference %
	Graphical estimate (Equation 3.2)	Dynamic estimate (Equation 3.3)	
Soft system	262.4 J	246.7 J	6
Stiff system	0.0	0.3 J	n/a

For the case of the soft loading system, the GRC follows a path different from the contact shear stress-slip curve. The available strain energy outweighs the plastic work done by the friction, resulting in the radiation of seismic energy. The graphical estimates of the area between the GRC and the contact stress-slip curve, multiplied by the contact length shows a difference within 6% of the dynamic calculation of the radiated seismic energy calculated in UDEC simulations. Note that in order to avoid dealing with the shear failure localization, we assume the contact at point A is representative of the overall interface response to shear. This assumption can be the source of the relatively large difference of 6% since our previous findings (Khademian et al., 2017) showed that the shear and normal stresses are not uniformly distributed over the interface. The results in Table 3.3 allow some extension of the study of shear-type rock burst in more complex settings where there is no simple way to graphically estimate radiated seismic energy from an idealized loading system stiffness.

3.5.2 Modeling Rupture along Strike-Slip Fault

Direct shear test configuration in Figure 3.6 represented some fraction of a fault since the upper block was not bound but free to move throughout the contact when slip initiated. It means W kept driving the slip even when ΔU was fully exhausted. However, in geological settings, fault segments are mostly confined either by other intersecting discontinuities or by unfeathered volumes of rock with higher shear strength. Excavation-induced stresses serve the external loading work W and reactivate the fault but rupture is mainly controlled by ΔU . In this section, we simulate a fault (Figure 3.7) where rupture is restricted to the degree of the fault's slip-weakening behavior, loading system stiffness, and ΔU .

Boundary loading conditions and the mesh geometry are two crucial aspects of modeling rupture along a fault. The shear load distribution generated by loading conditions governs the onset of a rupture, rupture length, and the radiated seismic energy. Modeling a fault in UDEC requires a detailed study on the mesh geometry since mesh size affects the progression of the slip failure when a slip-weakening behavior is applied to the fault (Khademian et al., 2017). In order to find the effective mesh geometry and

loading conditions, we compare models with different loading conditions and mesh sizes against the analytical functions developed by Ryder (1988).

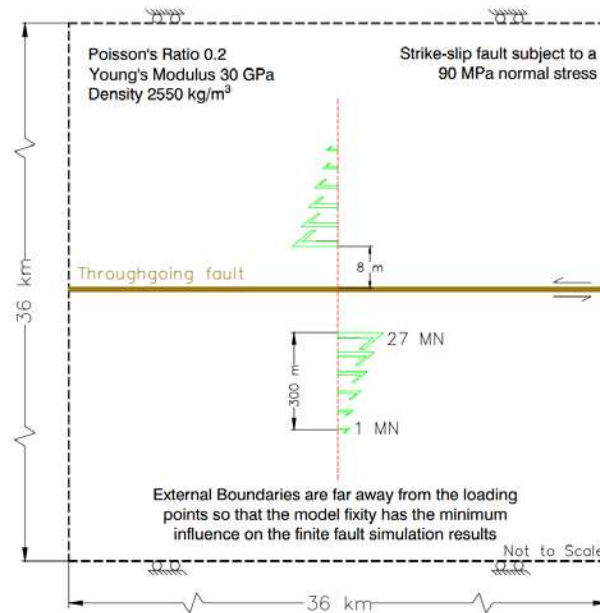


Figure 3.7 2-D numerical model geometry and initial conditions on the schematic plan view of the fault.

Ryder (1988) analyzed the possible shear stress distributions along a fault with the slip-weakening behavior of zero D_c and for each prototypical example calculated the slip distribution after the shear slip on the fault. Using a trial and error process, we simulated models constructed by different mesh geometries and loaded under different loading conditions, including applying force to the outer boundary of the model, shear stress on the fault plane, uniformly distributed force couples, and applying non-uniform force couples. We found the distributed, non-uniform force couples (Figure 3.7) to produce a symmetrical slip distribution event suggested by Ryder (1988). Symmetrical slip distribution is a relatively realistic distribution for general use in mining seismological calculations. The effective mesh size was also found to follow a 1:40 ratio of the maximum mesh size to rupture length. Figure 3.7 shows the conceptualized model configuration and loading conditions. The geomechanical properties of the matrix, fault properties, and constitutive laws are listed in Table 3.4.

Table 3.4 Fault and Matrix Properties for Simulating Rupture along a Strike-Slip Fault.

Matrix properties			Fault properties: Residual Mohr-Coulomb constitutive law			
Young's modulus	Poisson ratio	Density	Initial friction coefficient	Residual friction coefficient	Shear and normal stiffnesses	Cohesion
30 GPa	0.2	2550 kg/m ³	0.6	0.49	50 GPa/m	0

The frictional properties assigned to the fault are demonstrated in Figure 3.8. Initial and residual friction coefficients follow the direct shear test frictional properties although a response with zero D_c is assigned to the fault here.

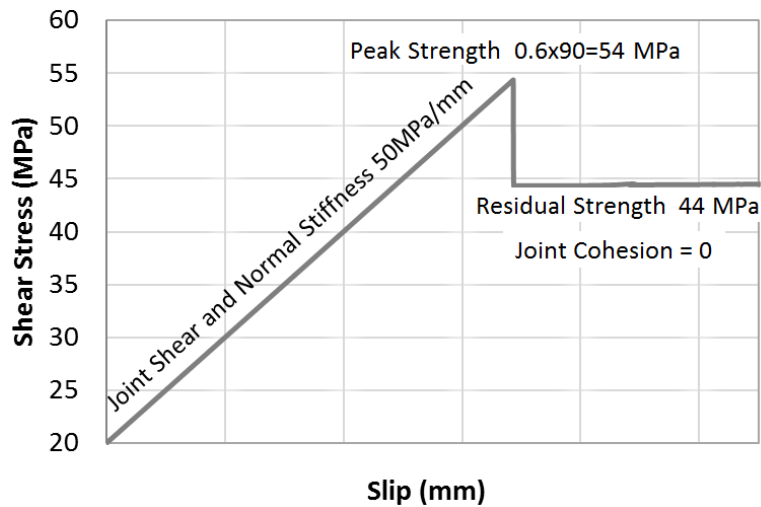


Figure 3.8 Frictional properties assigned to each element along the fault for simulating the brittle response.

Given the applied normal stress of 90 MPa, the initial shear strength of the fault is 54 MPa that drops to the 44 MPa residual shear strength once slip occurs (Figure 3.8). Shear force is developed along the fault by the non-uniformly distributed single couple that gradually increases from zero to 1 MN and 27 MN based on the pattern shown in Figure 3.7. Once slip initiates, the single couple remains constant yet rupture self-propagates if the initial release of the strain energy is enough to support the propagation.

We compare results of the fault stimulation in UDEC against analytical functions by using the concept of Excess Shear Stress (ESS) introduced by Ryder (1988). ESS is defined as the difference between the prevailing shear stress prior to slip and the dynamic strength of the fault. A symmetrical ESS distribution along a 2-D fault is given as a function of the peak \widehat{ESS} value by

$$ESS = \widehat{ESS} (1 - x^2) \quad (3.4)$$

where \widehat{ESS} and x denote the peak ESS and a dimensionless function variable changing from -1 to 1, respectively. ESS profile drives the rupture and results in a slip profile along the fault, given as

$$Slip = \widehat{ESS} (2 - x^2)^{1.5} a (4 - 4v^2) / 3E \quad (3.5)$$

where a stands for the half of the ESS profile length known as the potential rupture length. E and v are Young's modulus and Poisson's ratio of the matrix. In Figure 3.9a, dots show the symmetrical ESS profile calculated by Equation 3.4 while the solid line represents the ESS recorded along the simulated fault at the onset of the slip. Figure 3.9b provides the slip profile along the rupture plane for the numerical results (triangles) and Ryder's calculations (solid curve). Note that the potential slip length, or the area with positive ESS in Figure 3.9a, is 42 m that is 23% smaller than the actual rupture length of 54.5 m in Figure 3.9b. The reason behind the difference between the potential and actual rupture lengths is provided by Figures 3.9c and 3.9d.

Reid (1906) showed that an elastic rebound of the strain energy previously stored by the continuous deformation of rock yields a discontinuous displacement along faults resulting in seismic events. Figure 3.9c shows the horizontal, continuous rock deformation along a 4 km center line across the fault trace shown in Figure 3.7. The rock deformation before failure in Figure 3.9c is the result of the external work W that leads to the accumulation of the strain energy U_i which is partially released by a discontinuous rupture in Figure 3.9d. The potential slip length is driven by W while the actual rupture length is powered by the available energy $(W + \Delta U)$ for the slip which is higher than W . Therefore the actual rupture length exceeds its potential length as shown in Figures 3.9a and 3.9b. Ryder (1988) also approximated the seismic moment (Equation 3.6) and the radiated seismic energy (Equation 3.7) for the driving ESS profile shown in Figure 3.9a.

$$M_o = 2.6 \widehat{ESS} \times a^2 \times l \quad (3.6)$$

$$W_k = \frac{\overline{ESS} \times M_o}{2G} \quad (3.7)$$

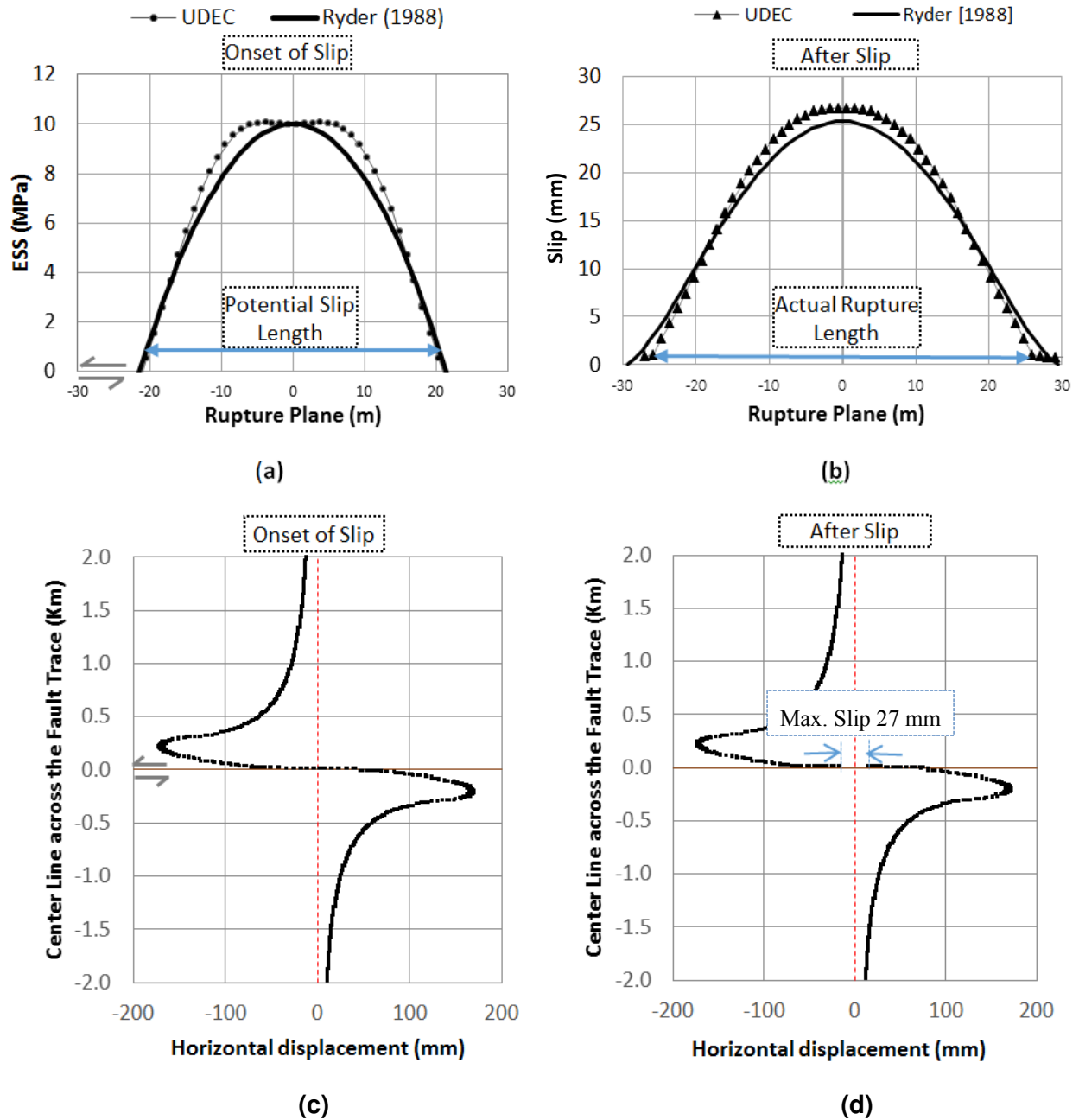


Figure 3.9 Comparison between the analytical and numerical solutions for: (a) driving ESS profile; (b) slip profile along a strike-slip fault with zero D_c ; (c) Continuous deformation parallel to the fault before slip; (d) Discontinuous horizontal displacement after slip.

In Equations 3.6 and 3.7, \overline{ESS} denotes the average ESS over its profile and l is the fault strike length that for the 2-D simulation is assumed 1 m. For calculating the seismic moment based on the numerical calculation of the slip (u) that is averaged over the rupture length (A_r), we use (Stain and Wyssession, 2003):

$$M_o = G \times A_r \times u, \quad (3.8)$$

where G is the shear modulus of the rock surrounding the fault and equals 12.5 GPa. Table 3.5 summarizes results of numerical model calculations and analytical functions.

Table 3.5 Comparison between Results from UDEC and Analytical Functions by Ryder (1988) for the Simulated Fault.

Method	\widehat{ESS}	\overline{ESS}	Average Slip (u)	half-width (a)	Rupture Length (A_r)	Seismic Moment (M_o)	Radiated seismic energy (W_k)
Ryder's method	9.9 MPa	7. MPa	15.4 mm	21. m	58. m	11.5 GJ	3.2 MJ
UDEC results	9.9 MPa	7.4 MPa	15.7 mm	20.4 m	54.5 m	11.4 GJ	3.4 MJ
error		6%	2%	3%	6%	1%	6%

Radiated seismic energy calculated from the UDEC is 3.4 MJ as compared to the analytical result of 3.2 MJ for an error of 6%. There are errors of 6% and 2% for rupture length and average slip calculations, respectively. Since the ESS profile mainly drives the resulting rupture parameters in Table 3.5, the errors mostly originate from mismatching between the numerical and analytical ESS profiles in Figure 3.9a. The relative consistency between the results emphasizes the potential capabilities of this methodology and the modeling approach in studying rock burst induced by a shear slip along pre-existing faults.

3.6 Discussion

The idealized example of compressive-type rock burst in sections 3.4.1 and 3.4.2 show the interaction between the loading system stiffness and the brittle response of the pillar. Figure 3.2 suggests that the ductile response of the pillar forces the GRC to follow the pillar failure curve, indicating effects of pillar failure curves on GRCs. Graphical estimates in Figure 3.3 imply that if the loading system stiffness remains greater than the slope of the pillar post-peak failure curve, GRC follows the pillar failure curve, resulting in near-zero radiated seismic energy. Figure 3.4 suggests that if the loading system stiffness remains lower than the post-peak slope of the pillar failure curves, the slope of the GRC is also influenced by the loading system stiffness. Figure 3.4 shows that the slope of GRCs also affects the brittleness behavior of the pillar such that the most brittle pillar failure corresponds to the stiffest system. This can be related to the dynamic loading effects of seismic energy radiation on the shear band within the failing pillar. Compressive loading fails the pillar through developing shear failure bands. Higher magnitudes of radiated seismic energy create dynamic effects that cause a wider shear band within the pillar during failure. Wider shear band consumes higher plastic work, resulting in a less brittle response

because plastic work is the area below the failure curve. Stiff loading system, however, radiates insignificant radiated seismic energy and causes the pillar to fail through a narrower shear band, leading to a less plastic work consumption and more brittle behavior. These results show the complexity of an unstable failure evolution but future studies are required to quantify interdependent relationships between loading stiffness, brittleness, and radiated seismic energy magnitude during an unstable failure.

The idealized model of a rupture along a discontinuity is performed by the use of a simple direct shear test in Section 3.5.1. GRCs for soft and stiff loading systems show that the ground reaction depends on the loading system stiffness. If the loading system stiffness is greater than the post-peak slope of shear stress-slip curves, the GRC matches with the shear stress-slip curve; otherwise, the loading system stiffness controls the slope of the GRC. Modeling shear-type rock burst due to an unstable slip along a pre-existing fault is checked against the analytical calculations by Ryder (1988). Note that following the assumptions made by Ryder (1988), we ignore the energy required for fracturing the matrix and assume that the fault is encompassed by elastic materials. The matrix fracturing energy could contribute to the radiated seismic energy magnitude through increasing the plastic work in the energy balance shown by Equations 3.1 and 3.2. The radiated seismic energy, average slip, and rupture length that are calculated within UDEC are within 3%, 6% and 3% errors of the analytical results. Models with finer meshes under different loading conditions may result in lower errors but require higher numerical processing power and more efficient simulation tools. Given the relative agreement between the analytical and numerical results, future studies can be conducted to quantitatively examine the scaling of the radiated seismic energy with the rupture length and average slip in more complex fault zones.

3.7 Conclusions

This chapter suggests a numerical methodology for modeling unstable rock failures, also known as rock burst, brought about by excavation activities in rock masses underground. The methodology tracks the energy stored, consumed, or ultimately released as radiated seismic energy when conditions of instability are met. Unstable failures due to loading in compression are exemplified by a tabular opening supported by a single pillar. Multiple material models are applied in UDEC to achieve a wide range of pillar post-failure stress-displacement responses and loading system stiffness values. Numerical calculations of seismic energy radiated from these models are shown to be within 3% error of expected graphical values. An idealized strike-slip fault is then modeled and numerical results of the rupture length, slip, and radiated seismic energy are found within 6% of the analytic solution. Given the verification examples provided in the present chapter, one can assess the shear- and compressive-type rock burst potentials in various mining layouts within complex fracture networks through relying on the proposed

seismic energy calculations. The methodology and modeling approach are shown to be valid for studying natural and induced seismic events in different geologic settings.

3.8 Reference

- Ahmad, F., Hosseini, A.M., Titi, H., Schwandt, S., 2018. Evaluation of WisDOT Quality Management Program (QMP) Activities and Impacts on Pavement Performance
- Barton, C.A., Zoback, M.D., Moos, D., 1995. Fluid flow along potentially active faults in crystalline rock. *Geology* 23, 683–686. [https://doi.org/10.1130/0091-7613\(1995\)023<0683:FFAPAF>2.3.CO](https://doi.org/10.1130/0091-7613(1995)023<0683:FFAPAF>2.3.CO)
- Beeler, N.M., 2001. Stress drop with constant, scale independent seismic efficiency and overshoot. *Geophys. Res. Lett.* 28, 3353–3356. <https://doi.org/10.1029/2001GL012906>
- Brune, J.N., 1970. Tectonic stress and the spectra of seismic shear waves from earthquakes. *J. Geophys. Res.* 75, 4997–5009. <https://doi.org/10.1029/JB075i026p04997>
- Cook, N.G.W., 1966a. Rock mechanics applied to study of rockbursts. *J. South African Inst. Min. Metall.* 66, 435–528.
- Cook, N.G.W., 1966b. The design of underground excavations, in: Eighth Symposium on Rock Mechanics, University of Minnesota, in Failure and Breakage of Rock. pp. 167–193.
- Cook, N.G.W., 1965. A note on rockbursts considered as a problem of stability. *J. South African Inst. Min. Metall.* 65, 437–446.
- Dieterich, J.H., 1979. Modeling of rock friction: 1. Experimental results and constitutive equations. *J. Geophys. Res.* 84, 2161. <https://doi.org/10.1029/JB084iB05p02161>
- Duvall, W.I., Stephenson, D.E., 1965. Seismic energy available from rockbursts and underground explosions. *Trans. Soc. Min. Eng.* 232, 235–240.
- Garvey, R., Ozbay, U., 2013. Assessing coal bumps from excess energy in finite difference models, in: 11th International Conference on Ground Control in Mining. [https://doi.org/10.1016/0886-7798\(92\)90134-4](https://doi.org/10.1016/0886-7798(92)90134-4)
- Goodman, R.E., Sundaram, P.N., 1978. Fault and system stiffness and stick-Slip phenomena. *Pure Appl. Geophys.* 116, 871–887.
- Gu, R., Ozbay, U., 2014. Distinct element analysis of unstable shear failure of rock discontinuities in underground mining conditions. <https://doi.org/10.1016/j.ijrmms.2014.02.012>
- Itasca, 2016. Background - The 2D Distinct Element Method, UDEC Manual.
- Jaeger, J.C., Cook, N.G.W., 1976. Fundamentals of rock mechanics. Chapman and Hall LTD.
- Joughin, N C; Jager, A.J.I., 1983. Fracture of rock at stope faces in South African Gold Mines, in: Rockbursts: Prediction and Control. pp. 53–66.
- Khademian, Z., Nakagawa, M., Garvey, R., Ozbay, U., 2017. Role of fluid injection pressure in inducing seismicity, in: Proceedings of the 42nd Workshop on Geothermal Reservoir Engineering. p. 10.
- Linkov, A.M., 2005. Numerical modeling of seismic and aseismic events in geomechanics. *J. Min. Sci.* 41, 14–26. <https://doi.org/10.1007/s10913-005-0059-3>
- Lockner, D.A., Beeler, N.M., 1999. Premonitory slip and tidal triggering of earthquakes. *J. Geophys. Res. Solid Earth* 104, 20133–20151. <https://doi.org/10.1029/1999JB900205>

- Napier, J.A.L., Malan, D.F., 1997. A viscoplastic discontinuum model of time-dependent fracture and seismicity effects in brittle rock. *Int. J. Rock Mech. Min. Sci.* 34, 1075–1089.
[https://doi.org/10.1016/S1365-1609\(97\)90201-X](https://doi.org/10.1016/S1365-1609(97)90201-X)
- Petukhovt, I. M., Linkov, A.M., 1979. The theory of post-failure deformations and the problem of stability in rock mechanics. *Int. J. Rock Mech. Min. Sci. Geomech. Abstr* 16, 57–76.
- Poeck, E., Khademian, Z., Garvey, R., Ozbay, U., 2016. Modeling unstable rock failures in underground excavations, in: 2016 ISRM International Symposium, 2016 (Ed.), *Rock Mechanics and Rock Engineering: From the Past to the Future*. CRC Press, Ürgüp-Nevşehir, Turkey, pp. 505–509.
<https://doi.org/10.1201/9781315388502-86>
- Reid, H.F., 1906. The mechanics of the earthquake, the California earthquake of April 18, 1906, report of the state investigation commission.
- Rice, J.R., 1983. Constitutive relations for fault slip and earthquake instabilities. *Pure Appl. Geophys.* 121, 443–475. <https://doi.org/10.1007/BF02590151>
- Ryder, J. a., 1988. Excess shear stress in the assessment of geologically hazardous situations. *J. South African Inst. Min. Metall.* 88, 27–39.
- Salamon, M.D.G., 1993. Keynote address: Some applications of geomechanical modelling in rockburst and related research, in: 3rd Int. Symp. Rockbursts and Seismicity in Mines. pp. 297–309.
- Salamon, M.D.G., 1984. Energy considerations in rock mechanics: fundamental results 84, 233–246.
- Salamon, M.D.G., 1970. Stability, instability and design of pillar workings. *Int. J. Rock Mech. Min. Sci.* 7, 613–631. [https://doi.org/10.1016/0148-9062\(70\)90022-7](https://doi.org/10.1016/0148-9062(70)90022-7)
- Stain, S., Wyssession, M., 2003. An introduction to seismology, earthquakes, and earth structure.
- Starfield, A.M., Fairhurst, C., 1968. How high-speed computers advance design of practical mine pillar systems. *Engng Min. J.* 169.
- Stiller, H., Hurtig, E., Grosser, H., and Knoll, P., 1983. On the nature of mining tremors. *J. of Earthq. Predict.* 61.
- Van der Heever, P.K., 1984. Some technical and research aspects of the Klerksdrop seismic network, in: 1st International Congress on Rockbursts and Seismicity in Mines. pp. 349–350.
- Wawersik, W.R., Fairhurst, C., 1970. A study of brittle rock fracture in laboratory compression experiments. *Int. J. Rock Mech. Min. Sci. Geomech. Abstr.* 7, 561–575.
[https://doi.org/10.1016/0148-9062\(70\)90007-0](https://doi.org/10.1016/0148-9062(70)90007-0)
- Wong, T.-F., 2013. On the normal stress dependence of the shear fracture energy. *American Geophysical Union*, pp. 1–11. <https://doi.org/10.1029/GM037p0001>
- Zubelewicz, A., Morz, Z., 1983. Numerical simulation of rock burst processes treated as problems of dynamic instability. *Rock Mech. Rock Eng.* 16, 253–274.

CHAPTER 4

MODELING EARTHQUAKE RUPTURE PROPAGATION BASED ON CALCULATION OF ENERGY COMPONENTS

A manuscript submitted to the *Journal of Geophysical Research*

Zoheir Khademian, Masami Nakagawa, and Ugur Ozbay

4.1 Abstract

This chapter presents the application of the developed framework for simulating earthquake rupture (unstable or seismic slip) and aseismic slip along a fault. The framework is built on the Universal Distinct Element Code (UDEC) using its explicit time-stepping scheme. Evaluation of rupture energetics is first demonstrated by a direct shear test that simulates some unbound fraction of a fault with slip-weakening behaviors. This same approach is extended to model rupture along a shallow, strike-slip, fault that is constrained by surrounding elastic rockmass. The model mesh geometry and loading conditions are calibrated by simulating idealized fault activation and then checking the calculated rupture area, slip (cumulative displacement discontinuity), seismic moment, and radiated seismic energy against available analytic solutions. Loading the idealized fault by non-uniformly distributed single couples and mesh geometry that follows the 1:40 ratio of the mesh size to rupture length are found to generate results within 5% error of the analytical solutions. As an example of the methodology application, relationships between rock rigidity (shear modulus), slip-weakening behavior, rupture length, slip, seismic moment, and radiated seismic energy are then discussed through a set of parametric studies. Globally recorded variations between seismic energy and the seismic moment for shallow strike-slip earthquakes are also used to verify seismic energy calculations in each case of parametric studies. Results show that the developed methodology and modeling approach provide a useful framework for mechanistically studying earthquake physics.

4.2 Introduction

Modeling earthquake rupture provides key elements for better understanding strong ground motion and the physics of earthquake initiation, propagation, and arrest. The most commonly used models include dislocation or kinematic models, quasi-dynamic models, dynamic models, and mechanical spring-and-box models. This chapter introduces a numerical modeling methodology for dynamic modeling of fault slip and for exploring its stability by adopting the concept of the spring-and-box models. By

calculating the slip energy balance, the methodology assesses elements contributing to the nucleation, propagation, arrest, and intensity of rupture.

Dislocation models are one of the most used models for interpreting the seismic radiation and studying the earthquake source (Madariaga and Olsen, 1997). They are based on the kinematic propagation of slip along a fault plane where slip starts suddenly at time zero and spreads at constant velocity (Haskell, 1964; Savage, 1966). Unrealistic features of kinematic models are the arbitrary specification of slip and dislocation motion instead of following stress relaxation processes. Archambeau (1968), Brune (1970), Sato and Hirasawa (1973), and Madariaga (1976) improved the arbitrariness in the dislocation models by introducing quasi-dynamic models.

Quasi-dynamic models relate slip and dislocation motion to the dynamic stress drop, which is defined as the difference between constant initial and dynamic shear strength values. The quasi-dynamic numerical solution assumes constant velocity but the model can be still considered dynamic as it is solved for the fault motion given the prescribed constant slip velocity and dynamic stress drop. In these models, rupture starts with an abrupt stress drop at the initiation point and grows at a constant velocity. The rupture stops by artificial unbreakable patches simulated by an abrupt jump in the fault strength. However, the abrupt drop and jump in fault strength cause singularity at the crack tip. For avoiding singularity and ensuring smoothness in the solution, Andrews (1985) adopted a frictional strength variable as a function of position and time. Inside the rupture initiation area, the fault strength equals the dynamic friction strength, which is prescribed at a constant level below the initial uniform shear stress. Outside the initiation area, the strength does not jump abruptly but rises linearly at a constant slope to arbitrarily large values. This linear increase in the strength ensures the rupture arrest while the solution is still smooth. Note that in quasi-dynamic models the rupture area is also a priori because rupture stops as it runs into the prescribed zone of high strength outside the initiation area. Dislocation and quasi-dynamic models have played a major role in the quantification of earthquakes and in the inversion of seismic data. For an instant, Kaneko and Shearer (2015) used a quasi-dynamic modeling approach and conducted parametric tests on rupture speed, rupture directivity, and source geometry, investigating the origin of variability in inferred stress drops and radiated energy. However, understanding the evolution, propagation and arrest of ruptures requires studying friction characteristics of faults and rupture propagation simulated by dynamic modeling approaches (Madariaga, Olsen, and Archuleta, 1998). The most important feature of dynamic models is that the rupture velocity is not a priori constraint but is determined from friction laws.

More closely related to the approach studied here is the dynamic model proposed by Ida (1972) and Andrews (1976) who introduced slip-weakening friction laws in dynamic modeling of 2D ruptures. In

slip-weakening constitutive law, slip is near zero until the total stress reaches a peak value. Once this stress is met, slip increases and shear strength decreases simultaneously until slip reaches a critical distance called length scale or characteristic distance (D_c). After D_c is reached, slip may still continue but under a constant residual stress that equals the dynamic strength of the fault. Andrews (1976) and Madariaga et al. (1998) showed that slip weakening at small slip is necessary for the friction law to be realizable in terms of energy conservation of a fault system. This is because D_c is the main ingredient of the fracture energy, the plastic work done at the rupture front in excess of the work done against the constant residual stress, that contributes to the energy balance (Andrews, 1976, 1985). Dieterich (1978, 1979) and Ruina (1983) introduced rate-weakening constitutive laws and showed that for large values of slip, fault strength is driven by slip rate. In this chapter, we could use the rate-dependent law but because the main focus is on the rupture energetics and phenomenology, we simplify the fault frictional behavior by using a slip-weakening friction law.

Other features that distinguish most dynamic models from quasi-dynamic and dislocation models are that the rupture is initiated from a finite patch by an initial push and the shear stress is not uniform along the fault. Andrews (1976,1985) showed that once the slip-weakening behaviors and thus the fracture energy (a function of D_c , peak, and residual strengths) are prescribed, a rupture cannot nucleate at a point but must start from a zone with a critical size. It means in order for rupture to expand, there must be a sudden and strong push that can be achieved by assigning high stress over a finite zone, sometimes referred to as the minimum rupture patch. For smaller values of the initial stress or the minimum patch size, the rupture would simply stop. However, the initial push is not needed when using the Dieterich-Ruina friction laws that comprise a time-dependent relaxation process or when adopting a numerical procedure that gradually builds up initial stresses over time. For avoiding a prescribed initial push, this chapter adopts the latter type of initiating a rupture by building up stresses along a fault. Regarding the initial stress distribution, Madariaga et al. (1998) argued that in uniform initial stress fields, rupture would occur instantaneously or grow at the maximum possible velocity from an arbitrary point on the fault which is not realistic and not supported by observations. Following suggestions from existing analytical solutions on initial stress distributions (Ryder, 1988), this chapter simulates non-uniform initial stresses on the fault to prevent unrealistic results of rupture characteristics.

In above-mentioned modeling approaches, it was assumed that once the shear stress on a fault exceeds its peak friction, a rupture (unstable or seismic slip) is initiated. However, laboratory analyses show that there must exist specific conditions for the slip to be unstable and lead to a significant radiation of seismic energy. That is, shear slip along a fault can occur in either stable (creep) or unstable (rupture) modes. Conditions leading to slip instability have been analyzed in a box-spring system in which the box

is connected to a loading point through a spring of stiffness k and is moved over a surface (Dieterich, 1979; Rice, 1983). The contact between the box and the surface is assumed to be a discontinuity and the spring stiffness is referred to as the loading system stiffness. For an unstable slip to occur, the loading system stiffness must be less than a critical value, which is the slope of the post-peak of the shear force-slip curve in a slip-weakening frictional behavior. Rice (1983) showed that radiated seismic energy can be estimated by comparing the spring reaction load curve and the post-peak curve of the discontinuity shear force-slip. The loading system stiffness mainly dictates the slope of the spring reaction load curve (defined as GRC later in this chapter). Following the mechanical models developed by Rice (1983), this chapter mechanistically translates the simple concept of instability into a numerical methodology and discusses two methods for estimating radiated seismic energy.

Haskell (1964) estimated seismic energy by examining the seismic radiation of body waves passing through a distant surface enclosing the simulated fault. This method calculates the radiated energy carried by the far-field body waves through a surface over the focal sphere and is commonly used in kinematic and quasi-dynamic models of rupture (Gheibi and Hedayat, 2018; Ide, 2002; Kaneko and Shearer, 2015). However, Kostrov (1974) used stress-slip relaxation to derive formulas for calculating radiated seismic energy on a simulated fault. In this method, mainly used in dynamic rupture models (Favreau and Archuleta, 2003; Ma and Archuleta, 2006), the total work done by external forces during slip, and the total energy loss during faulting were calculated and their difference was introduced as the radiated energy. This chapter suggests two approaches for estimating radiated seismic energy. Similar to the method used by Kostrov (1974), the first approach calculates radiated seismic energy by comparing the state of energy within the system before and after the rupture. The approach also argues a method to determine the amount of seismic energy separately radiated from each energy source along the fault. Similar to the method used by Haskell (1964), the second approach obtains radiated seismic energy by estimating the total kinetic energy that needs to be released during a rupture in order for the system to reach mechanical equilibrium.

This chapter presents a numerical methodology developed in the distinct element based numerical model UDEC for modeling rupture initiation, propagation, and arrest while directly calculating the magnitude of seismic energy that radiates if conditions for instability arise. A numerical direct shear test is used to show the concept of slip-weakening constitutive law and instability in the framework of energy. The proposed methodology is further advanced for understanding the rupture physics along a shallow strike-slip fault where rupture initiation area, rupture length, shear stress drop, initial shear stress, and slip velocity are not prescribed. We develop a procedure for the quasi-static buildup of shear stresses over the strike-slip fault until rupture is initiated on a nucleation patch. Then, a dynamic model is calculated to

complete the self-propagating rupture up to the point of the rupture arrest. For calibrating the loading conditions and making results independent of the grid (or mesh) size, we check modeling results against an analytical solution. Finally, one application of the developed methodology is exemplified by investigating variations of radiated seismic energy, seismic moment, slip instability, rupture length, and maximum slip along fault models with different D_c responses under various loading system stiffness values. This shows how radiated seismic energy and concept of instability help study elements differentiating a rupture from an aseismic slip or creep. We verify results of each simulation by calculating the scaled energy, the ratio of the radiated seismic energy to the seismic moment, and comparing it to existing seismic records for strike-slip earthquakes.

4.3 Rock Mass Energy Components

External forces in the earth's crust cause the steady deformation of rock mass resulting in an accumulation of strain energy (U_i) in them. Gravitational forces, tectonic loads, residual stress fields from previous seismic events, and stresses induced by human activities are major external forces that generate the steady deformation of rock mass. External forces that are active during the slip propagation can exclusively contribute to the transfer of energy by providing active external work (W) through continued deformations. The active external work in conjunction with the release of U_i govern a shear slip accompanied by dissipative energy terms of plastic work (W_p) and radiated seismic energy (W_k). W_p represents energy consumed during frictional heating generated by shear sliding, fracturing or inelastic deformation of rock matrix (Prieto et al., 2012). W_p can be also viewed as the sum of the fracture energy and the energy dissipated by the residual friction of a fault. Significant W_k radiates from the system if W and the release of U_i are not fully exhausted by W_p during the slip (Salamon 1984). Referring to the model presented by Brune (1970), slip does not necessarily lead to a complete exhaustion of U_i and, therefore, significant residual strain energy (U_r) may still remain in the fault system. Based on the descriptions given above, we use in this study the following relationship for describing the energy transfer during a rupture.

$$W + U_i = W_p + U_r + W_k \quad (4.1)$$

The left-hand side of this equation represents energy available prior to slip and the right-hand side is the state of energy after slip. Introducing a new term of ΔU , Equation 4.1 can be rearranged to:

$$W_k = W + \Delta U - W_p \quad (4.2)$$

where ΔU is the difference between U_i and U_r , representing the release of strain energy during the slip. The radiated seismic energy calculation based on the static energy terms in Equation 4.2 can be checked

against dynamic calculations of seismic energy based on the mechanical damping approach developed in UDEC.

The UDEC numerical model uses an explicit time marching scheme that alternates between applications of a force-displacement law at all contacts (discontinuities) and Newton's second law at all deformable blocks. Interactions between blocks divided by discontinuities are solved by the distinct element method while stresses and deformations inside the blocks are calculated by discretizing the blocks with finite difference elements. In this approach, the force-displacement law is used to calculate normal and shear forces on contracts between the blocks from known displacements. Newton's second law gives the motion at the gridpoints of finite difference elements within the blocks, originated from the known body forces and contact forces acting on the blocks. Then, stresses within the elements are updated through the application of the block material constitutive relations (Itasca, 2016). In order to reach an equilibrium solution, the explicit time-marching approach in UDEC uses a damping force and dissipates a fraction of the system kinetic energy at each time step. The magnitude of the damping force at a gridpoint is proportional to the magnitude of the unbalanced force. The damping force direction is such that energy is always dissipated. In this form of damping, known as local damping, the amount of damping varies from point to point and body forces vanish for steady-state conditions. The magnitude of damping constant is dimensionless and independent of properties or boundary conditions. For this study, choosing the damping constant is part of the calibration process explained in section 4.4.4. The damped kinetic energy at each timestep is cumulatively recorded as damped work (W_D). The remaining kinetic energy in the system at each timestep is termed current kinetic energy (U_K) that is a non-cumulative term. U_K approaches zero as the model reaches equilibrium and goes up during the simulation of a dynamic response. Equations for calculating W_D and U_K are included in Appendix C. The sum of W_D and U_K at the end of a simulation yields the seismic energy radiated from the system in the form:

$$W_k = U_K + W_D \quad (4.3)$$

Equation 4.3 provides the dynamic calculation of W_k . Chapter 2 of this study simulated tunneling-induced seismicity and showed that W_k calculated by Equation 4.2 matches results of Equation 4.3 and those of analytical solutions provided by Duvall and Stephenson (1965), Salamon (1984), and Cook (1966). The next section adopts a faulting configuration and shows that W_k calculated by Equation 4.3 is in agreement with that calculated by static energy components in Equation 4.2. Depending on the capability of employed numerical tools, one can use either of these equations for estimating seismic energy radiated from seismic events. The next section discusses how the transfer of energy depends on frictional behaviors of a fault and mechanical properties of the surrounding rock.

4.4 Physics of Rupture

Rice (1983) and Salamon (1984) showed that the magnitude of radiated seismic energy during a rupture depends on the fault slip-weakening behavior and the loading system stiffness. Slip-weakening response defines the fracture energy and depends on the characteristic distance D_c (Andrews, 1976; Rice, 1983); a lower D_c results in lower fracture energy. The loading system stiffness (k) relates to the magnitude and rigidity (shear modulus) of rock surrounding a fault (Goodman and Sundaram, 1978; Jaeger and Cook, 1976) as:

$$k \propto G \propto \frac{1}{l} \quad (4.4)$$

In Equation 4.4, l is part of a fault undergoing slip (rupture or slip length), and G is the rigidity of the surrounding rock. The loading stiffness dictates the strain energy magnitude U_i that can be stored in the rock while slip-weakening behavior controls W_p through affecting the fracture energy. According to Equation 4.1, a high magnitude U_i and low magnitude W_p result in a significant release of W_k , leading to a rupture. An idealized model of slip in a direct shear test configuration is used here to explain the concept of rupture and aseismic slip events.

4.4.1 Idealized Model of Rupture

Figure 4.1 conceptualizes the slip mechanics in a direct shear test consisting of two blocks, each being 15 cm high. The upper and lower blocks are 20 and 30 cm wide, respectively. The faulting is simulated through the movement of the upper block. Given the upper block can slide throughout the interface between the blocks, the direct shear test is a simplified representation of some fraction of a fault segment on a geologic scale. That is, the simulated faulting is not constrained by the unloaded segments. Figure 4.1a shows the blocks before loading when the average shear stress within the upper block (τ) and slip (d) at point A are zero. Figure 4.1b relates to the onset of the slip where the external work W imposes deformation on the upper block and develops U_i prior to the slip propagation. We simulate a shallow slip at a depth of 3.6 km by applying a normal stress of 90 MPa, assuming rock density is 2550 kg/m³. W is imposed by the constant normal stress and a horizontal velocity loading of 1 mm/s over the upper block. The peak average shear stress within the upper block (τ_p) occurs at the onset of rupture in Figure 4.1b. Ignoring the pre-slip creep or elastic deformation along the contact, slip at point A can be considered zero in Figure 4.1b.

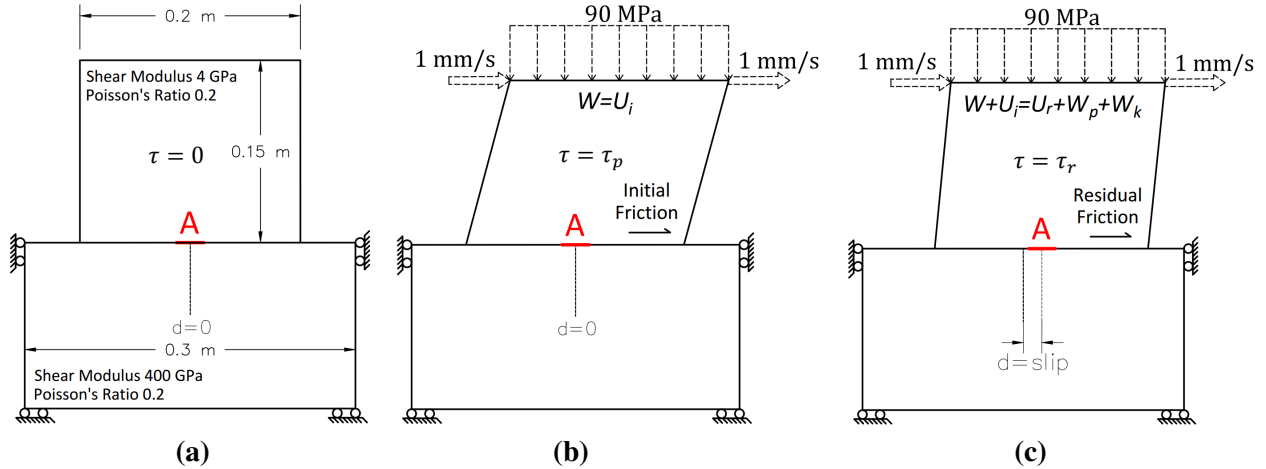


Figure 4.1 Schematic of rupture mechanics: (a) Model geometry for the direct shear test; (b) Schematic representation of the block deformation just before rupture; (c) Post-rupture state and transfer of energy

As the loading increases in the sheared direction, the asperities are gradually damaged until slip initiates (Figure 4.1c). Note that we simulate the asperities by assigning initial and residual friction coefficients to a plane interface. Once slip occurs in Figure 4.1c, the peak average shear stress within the upper block reduces to the residual value of τ_r .

The slip introduces W_p on the damaged contact while leaving residual strain energy U_r in the upper block. Based on Equation 4.1, we can obtain radiated seismic energy W_k as a measure for instability by directly calculating W , U_i , W_p , and U_r . However, for discussing the concept of instability, we graphically calculate each energy component using the loading system stiffness k and interface shear stress-slip curve. We plot τ (average shear stress within the upper block) against slip along the discontinuity at each timestep and provide a curve whose slope represents k . We term this curve the Ground Reaction Curve (GRC) since it indicates the reaction of the surrounding rock to the slip.

GRC is analogous to the spring reaction load curve as defined by Rice (1983) in his classical box-spring experiments. Outlining GRCs and interface stress-slip curves on one plot allows the graphical calculation of energy terms in Equation 2. The objective of the next section is to show the significance of the GRC as the curve that should be followed by the interface stress-slip curve if the slip is aseismic and near-zero seismic energy is radiated. By investigating different slip-weakening behaviors and loading system stiffness values, we show that any departure from the GRC indicates a radiated energy component accompanied by a rupture. We calculate radiated seismic energy graphically using Equation 4.2 and numerically using Equation 4.3 and show the agreement between results. For these analyses, a damping constant of 0.8 is adopted and the blocks are divided into meshes with the maximum width of 0.5 mm.

The choice of the mesh size and damping constant is based on a calibration process that will be later explained in section 4.2.

4.4.1.1 Slip-Weakening Behaviors and Loading System Stiffness

Four shear tests are modeled by assigning three characteristic distances to the interface and simulating two loading systems. Coulomb slip with a lower residual strength is used for modeling a shear behavior with $D_c=0$ while the ductile response ($D_c \sim \text{infinity}$) is simulated by the Coulomb elastoplastic constitutive law. The Continuously Yielding (CY) joint model (Cundall and Lemos, 1990) is employed to simulate the slip-weakening behavior with $D_c=0.45$ mm. Responses with zero and near-infinite D_c are used for exploring effects of slip-weakening behaviors on instability. The response with 0.45 mm characteristic distance is then used for running two shear tests investigating roles of loading system stiffness (or GRCs) in the slip instability. For each response, an initial friction coefficient of 0.6 is assigned to the interface that corresponds to a lower-limit initial friction within fractured rock masses (Barton et al., 1995). Ignoring overshoot in the rupture simulation, dynamic and residual friction coefficients are assumed equal to 0.49 that can be acceptable as both dynamic and residual friction coefficients based on laboratory observations (Beeler, 2001; Karner and Marone, 2000; Lockner and Beeler, 1999; Wong, 2013).

Solid curves in Figure 4.2 represent stress-slip curves recorded on the contact at point A (Figure 4.1) and dashed curves show respective GRCs. Figure 4.2a provides results of two shear tests with zero and near-infinite D_c under a soft loading system. As shown in Equation 4.4, the loading system stiffness k (slope of GRC) is proportional to the shear modulus of the surrounding rock. We simulate a relatively soft loading system by assigning a 4 GPa shear modulus to the upper block. In Figure 4.2a, the dashed black line is the reaction of the upper block to the abrupt drop of the stress and represents the GRC with the slope of 22 MPa/mm. The GRC for the ductile response follows the stress-slip curve, suggesting a near-zero GRC slope. Figure 4.2b gives results of two shear tests with constant D_c of 0.45 mm under soft and stiff loading systems. We simulate relatively soft and stiff loading systems where the upper blocks have shear moduli of 4 and 16 GPa, respectively. In Figure 4.2b, the black dashed line is the soft system GRC with a loading stiffness of 22 MPa/mm. The blue dashed line is the stiff system GRC whose slope exponentially decays from 104 MPa/mm to zero. For all tests, a high shear modulus of 400 GPa is assigned to the lower block to exclude the lower blocks from the energy transfer.

Note that in the ductile curve after the peak in Figure 4.2a, there is an unexpected decline in shear stress after the peak. This deviation results partly from the slight change in the normal stress acting on the interface as the slip progresses, and partly from the impacts of neighboring patches on the behavior of the

contact at point A. According to the instability notion by Rice (1983), and Salamon (1974, 1984), energy terms in Equation 4.2 can be quantified by comparing stress-slip curves with respective GRCs.

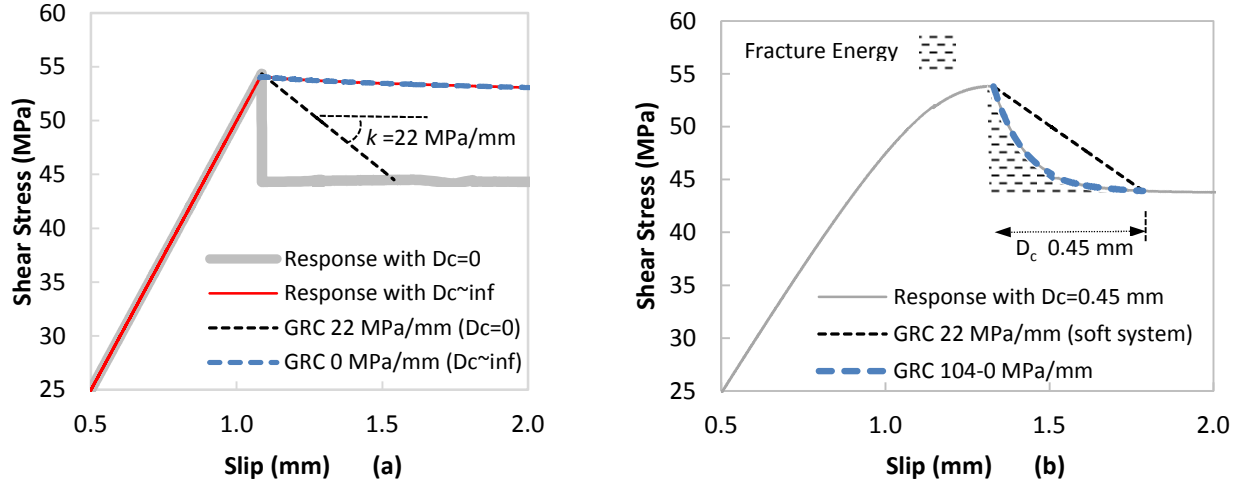


Figure 4.2 Responses of discontinuity and block matrix to the loading process in four direct shear tests: (a) stress-slip curves and GRCs for responses with zero and infinite characteristic distances. The interface shear and normal stiffnesses are assumed 50 MPa/mm; (b) stress-slip curves and GRCs for the softer system with $G=4$ GPa and stiffer system with $G=16$ GPa. The interface roughness is 0.1 mm.

The areas below the GRCs in Figure 4.2 are $W + \Delta U$ for each response and denote the energy density available for the slip failure. The blocks are elastic, so there is no energy consumption due to rock fracturing and thus W_p is a function of fracture energy (shown in Figure 4.2b) and residual friction work. Therefore, W_p can be quantified by calculating the area below the solid curves after their peaks, multiplied by the rupture length. The upper block slides throughout the interface, so the rupture length equals the interface length. According to Equation 4.2, areas between solid curves and respective GRCs are representative of W_k for each case. That is, the gap between GRCs and post-peak of stress-slip curves, multiplied by the rupture length yields a graphical estimate of the radiated seismic energy. Therefore, an aseismic slip characterized by near-zero seismic energy can be expected from the response with $D_c \sim \infty$ in Figure 4.2a and response under the stiff loading system in Figure 4.2b. This is because for these two cases interface stress-slip curves follow GRCs, $W + \Delta U$ is fully consumed by W_p , and the block rebounds through the same path as stress-slip curves. Therefore, the gap between GRCs and discontinuity stress-slip curves disappears and an aseismic slip with near-zero seismic energy is expected. By comparison, a rupture should result from the response with zero D_c in Figure 4.2a and the response under the soft system in Figure 4.2b. For these two responses, the area below the GRCs $W + \Delta U$ exceeds the area below solid

curves after peak W_p , resulting in gaps between GRCs and solid curves. As a result, we expect a rupture with relatively significant radiation of W_k . Note that in Figure 4.2b, W_p denotes the same areas for both stiff and soft systems. This is because W_p is a function of the fracture energy and the residual friction work, both of which are defined by the contact stress-slip curve that remains constant in both soft and stiff systems.

Based on Equation 4.3, we also obtain radiated seismic energy for the four shear tests. Table 4.1 compares the graphical estimates from Equation 4.2 and dynamic results from Equation 4.3. Note that for grasping the radiated seismic energy by Equation 4.3, we excluded the kinetic energy generated by the velocity loading over the upper block so that the isolated radiated energy exclusively represents the radiated seismic energy. Results of Equation 4.3 in Table 4.1 show that rupture events in Figures 4.2a and 4.2b generate 435.5 and 246.7 J seismic energy magnitudes, which are within 5.5 and 6% error of the graphical estimates, respectively. As expected, the aseismic slip events record an insignificant seismic energy magnitude of 0.3 J and 0.4 J, which are merely due to numerical noise introduced after the slip. Note that estimating graphical values of seismic energy is built upon the assumption that the stress-slip curve at point A represents the overall shear slip behavior of the entire interface. This assumption is the source of 6% and 5.5% errors in Table 4.1 because the shear stress distribution along the contact in the direct shear test is not uniform (Khademian et al., 2017).

Table 4.1 Comparison of Graphical and Numerical Estimates of Seismic Energy Radiated by Shear Tests.

Loading Stiffness	Slip Response	Seismic energy (J)		error
		Graphical -Equation 4.2	Dynamic -Equation 4.3	
Soft system G=4 GPa	D _c =0.45 mm	262.4 J (rupture)	246.7 J	6%
Stiff system G=10 GPa		0.0 (creep)	0.3 J	N/A
Soft system G=4 GPa	Abrupt drop in stress D _c =0	461.1 J (rupture)	435.5 J	5.5%
	Ductile behavior D _c ~infinity	0.0 J (creep)	0.4 J	N/A

Results in Table 4.1 illustrate significant roles of D_c and GRCs (or loading system stiffness) in distinguishing a rupture from an aseismic slip in a direct shear test. However, the direct shear test simulates a simplified infinite fault in which the upper block is not bound but free to move as the slip propagates. That is, the rupture is not arrested by the exhaustion of ΔU because W can still drive the slip even when ΔU is fully consumed. In geologic settings, however, fault segments are encompassed by rock

materials and are mostly restrained either by other intersecting discontinuities or by interlocking asperities of higher shear strength so that rupture is mainly powered by ΔU . The next section calibrates the dynamic simulation of rupture along a strike-slip fault surrounded by the elastic rock where the rupture is terminated once ΔU is fully consumed.

4.4.2 Calibration of Dynamic Rupture Model

Actual faults on geologic scales have complex features, like kinks or jogs, which form a fault zone having a certain thickness. However, many rupture simulators successfully approximate fault behaviors by regarding the source as the distribution of slip on a plane of weakness surrounded by an elastic medium (Ide and Takeo, 1997). We follow the same approach for modeling a fault but loading conditions, model mesh geometry, and damping constant need to be carefully calibrated. Using analytical functions derived by Ryder (1988), we optimized the mesh geometry and defined an effective loading condition through a trial and error process. The process is not shown here but we provide final results in the next section. Then, we discuss calibration of the damping constant through studying the sensitivity of radiated seismic energy and maximum slip to the damping constant.

4.4.2.1 Calibrating Loading Conditions and Mesh Sizes

Loading conditions influence the spatial distribution of initial shear stresses over a fault. Studying dynamic models of the 1992 Landers, 1994 Northridge, and 1995 Kobe earthquakes shows that the spatial distribution of the initial stress field controls the rupture propagation (Bouchon, 1997; Day, Yu, and Wald, 1998; Olsen, Matarese, and Archuleta, 1997; Peyrat, Olsen, and Madariaga, 2001). Madariaga et al. (1998) also showed the significance of loading conditions and initial stress distributions by arguing that initial stresses cannot be uniform along the rupture plane. As a result, calibrating loading conditions and resulting initial stress distributions is necessary for a successful rupture simulation. As explained by Madariaga et al. (1998), another essential requirement for an accurate numerical method is that the numerical solution becomes independent of mesh size. Mesh geometry affects the shear slip localization and therefore dictates the rupture initiation location (Khademian et al., 2017).

Ryder (1988) analyzed five families of possible initial shear stress distributions along a fault and derived analytic functions for the resulting slip profile, seismic moment, and radiated seismic energy. His calculation excluded the gradual slip-weakening behavior and assumed an abrupt stress drop with $D_c=0$. We constructed the fault model and simulated the abrupt stress drop response using frictional properties for zero D_c response in Figure 4.2a. We activated the fault by various loading conditions simulated in a quasi-static scheme: loading the outer boundary of the model, applying single force couple at the fault

center, applying uniformly distributed, and non-uniformly distributed force couples. We found that simulating a thick fault zone is necessary for grasping fault behaviors similar to the analytical functions. This approach of modeling a fault is similar to the thick fault zone devised by Madariaga et al. (1998), in which the fault zone was spread one-half grid cell to each side of the fault. We simulated a thick fault zone by applying the quasi-static loads at a distance b from the fault plane. We found that applying non-uniformly distributed force couples with the pattern shown in Figure 4.3 produces the 2-D symmetrical stress profile as shown in Figure 4.4. The effective mesh geometry also follows a 1:40 maximum mesh size to rupture length ratio. Note that for creating the 2-D symmetrical profile of Figure 4.4, b should be between 6 to 10 m. Other families of stress distribution can be simulated by varying distance b and applying non-uniform normal stress distributions on the fault but are out of the scope of this chapter.

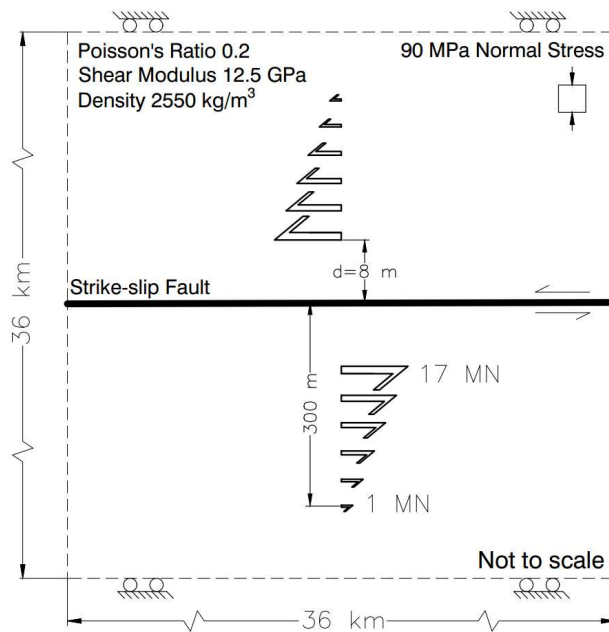


Figure 4.3 Numerical model geometry and initial conditions in a plan view of the vertical strike-slip fault.

The non-uniformly distributed force couples are applied in a quasi-static manner, meaning that they gradually increase from zero to one MN and 17 MN, following the pattern shown in Figure 4.3. This initial quasi-static loading develops W and can be viewed as the prestress field caused by a combination of internal tectonic plate deformation, plate motion, and the residual stress field remaining from previous seismic events (Madariaga and Olsen, 1997). The increase of initial quasi-static loading develops W and U_i prior to the rupture propagation and is then kept constant once rupture nucleates at the first patch on the fault. Then, we use dynamic calculations as the rupture self-propagates once ΔU and W are enough to drive the rupture progression. The rupture is arrested once ΔU is exhausted and W generated by the

constant initial loading can no longer overcome the shear strength of the neighboring unloaded segments. We compare shear stress profiles calculated by UDEC and Ryder (1988) in Figure 4.4a where the Excess Shear Stress (ESS) is defined as the difference between the shear stress on a fault prior to sliding and the dynamic strength of the fault. The main difference between ESS and the stress drop comes from the point that before rupture initiation, ESS on each patch can have positive or negative values, depending on the magnitude of initial stresses on the patch, but the stress drop stays zero because the rupture has not yet occurred. The ESS profile as a function of its peak value is:

$$ESS(x) = \widehat{ESS}(1 - x^2) \quad (4.5)$$

where \widehat{ESS} stands for the peak ESS and x is a nondimensional function variable changing from -1 to 1. The ESS profile drives the slip distribution along the fault, given as

$$Slip(x) = \widehat{ESS}(2 - x^2)^{3/2} a(4 - 4v^2)/3E \quad (4.6)$$

where a denotes the half-width of the ESS profile length. E and ν are Young's modulus and Poisson's ratio of the rock surrounding the fault, respectively. The solid curve and dots in Figure 4.4a represent the ESS distribution calculated by Equation 4.5 and the numerical model, respectively, at the onset of rupture. Figure 4.4b shows slip responses to the driving ESS profiles when the rupture is arrested and the system is once again in equilibrium.

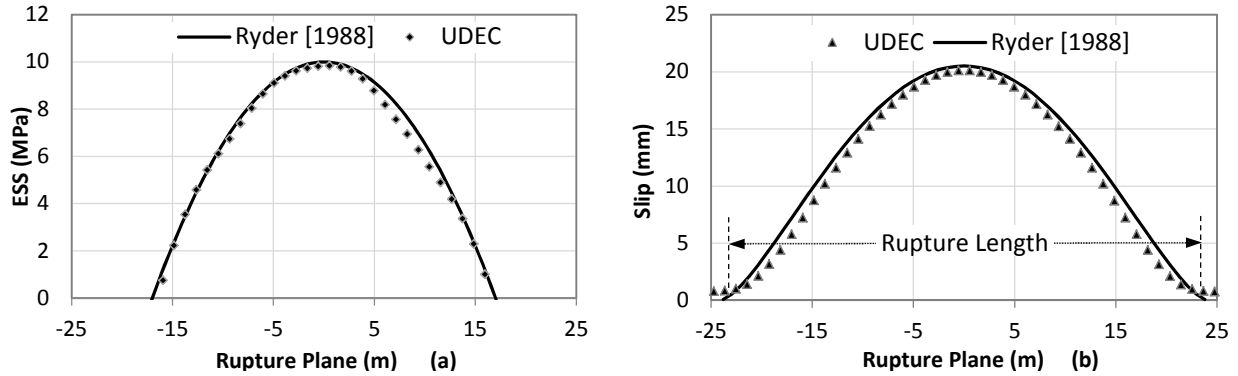


Figure 4.4 Comparison between analytical and numerical solutions for: (a) driving ESS profile; (b) analytical and numerical solutions for slip.

For the symmetrical ESS profile in Figure 4.4a, the seismic moment (M_0) and the radiated seismic energy are given respectively as

$$M_0 = 2.5 \widehat{ESS} \times a^2 \times l, \quad (4.7)$$

$$W_k = \frac{\overline{ESS} \times M_o}{2G}, \quad (4.8)$$

where l is the strike length and equals one as the analysis is two dimensional and \overline{ESS} is the average value of the distributed ESS along the fault (Ryder, 1988). Table 4.2 shows results of the calibration process and compares numerical results with analytical solutions for rupture length, average slip, seismic moment, and seismic energy. The numerical seismic moment is obtained as the product of the calculated rupture length, average slip, and rock shear modulus. The numerical results are within 5% of the analytical solutions. It is possible that the difference between the ESS profile developed by the numerical model and analytical functions in Figure 4.4a causes this 5% error.

Table 4.2 Comparison between Analytic and UDEC Results of Rupture Simulation.

Methods	\widehat{ESS}	\overline{ESS}	Average Slip	Half-width (a)	Rupture Length	Seismic Moment		Seismic Energy	
ESS method	10 MPa	6.5 MPa	12.9 mm	17 m	44.2 m	$2.5 \widehat{ESS} \times a^2 \times l$	7.2 GJ	$\frac{\overline{ESS} \times M_o}{2G}$	1.9 MJ
UDEC results	10 MPa	6.6 MPa	12.3 mm	16.9 m	45 m	$G \times A \times d$	6.9 GJ	-	1.8 MJ
Difference	-	2%	5%	0.5%	2%	4%		4%	

Figure 4.4b and Table 4.2 provide the final state of the faulting once rupture is arrested but do not reflect the rupture nucleation patch and the pattern of energy radiation on each patch or source of energy. A study on the spatial-temporal distribution of rupture and radiated energy can provide a further insight on the rupture initiation and propagation. Figure 4.5a shows the rupture initiation and part of its progression over time. The rupture initiates from the one-element long patch and spreads outwards.

The contours of slip show some fluctuation, indicating that after each rise in the slip magnitude, there is a period in which the slip magnitude stays constant before rising again. This fluctuation can be also observed in Figure 4.5b that represents cumulative seismic energy radiated from each patch along the fault. The radiated energy distribution is obtained using the GRC concept and shear stress-slip curve on each patch as explained in Figure 4.2a.

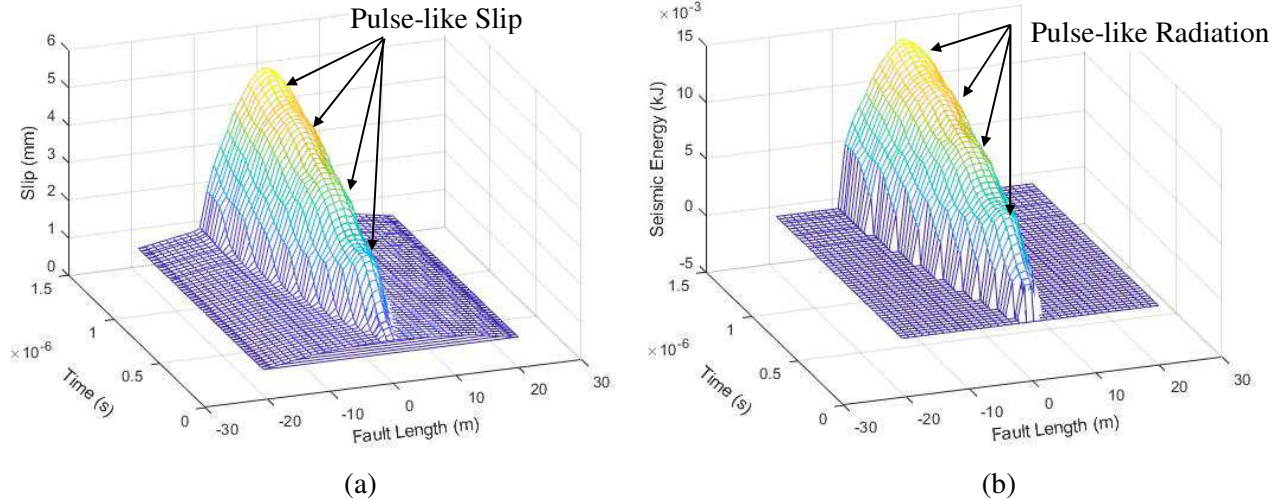


Figure 4.5 Spatial and temporal distribution of: (a) the rupture propagation; (b) energy radiation along the strike-slip fault for a fraction of the rupture duration.

The energy contours show periods where there is near-zero radiation following periods with high radiation of seismic energy. This fluctuation in both slip and radiated energy counters imply pulse-like rupture propagation that is consistent with observational and theoretical studies discussed by Bizzarri (2010) and Hiroo Kanamori and Anderson (1975). The pulse-like propagation suggests that only a small part of the fault ruptures at a given instant. The origin of the pulse-like behavior is mostly attributed to the heterogeneity of frictional properties (Das and Aki, 1977), strong rate-weakening behavior (Heaton, 1990), and stress distribution inhomogeneity (Beroza and Mikumo, 1996). Because this study excludes modeling frictional heterogeneity and rate-dependent friction laws, it is possible that the pulse-like behavior in Figure 4.5 is originated from the inhomogeneity in the stress distributions (Figure 4.4a).

4.4.2.2 Calibrating Damping Constant

For calibrating models in UDEC, we need to make results of the fault simulation independent of the damping constant. Figure 4.6 shows effects of different damping constants on the variability of radiated seismic energy and the maximum slip along the simulated fault. With zero damping constant, the radiated seismic energy is 0.65 MJ while the maximum slip on the fault reaches 39 mm.

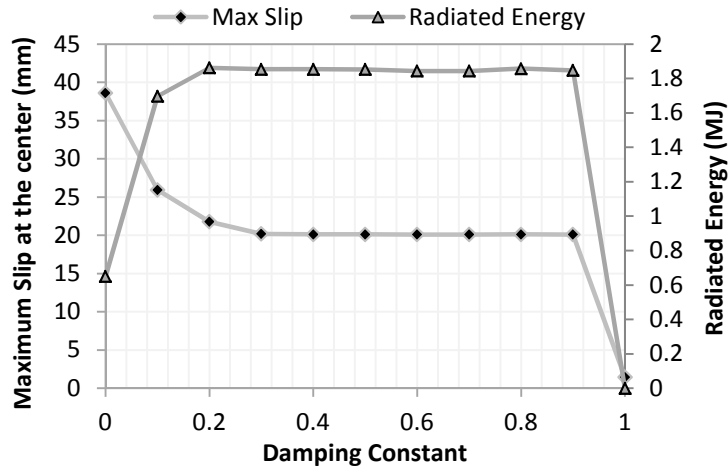


Figure 4.6 Sensitivity of radiated energy and maximum slip to the damping constant.

With 100% damping, the whole available kinetic energy is drawn out of the system so there is near-zero slip and radiated energy. Otherwise, a damping constant between 0.3 and 0.9 can sufficiently ensure the independence of results. For all simulations in this study, we use a damping constant of 0.8.

We calibrated the modeling approach for simulating dynamic rupture of a strike-slip fault and showed relative consistency between the analytical and numerical results in Table 4.2. We also showed the sensitivity of results to different damping constants and justified the use of 0.8 as the damping constant in simulations. The calibration process allows further studies on relationships between elements driving a rupture. As an example of methodology applications for quantifying relationships between elements contributing to the intensity of an event, we conduct a series of parametric tests on the characteristic distance of the slip-weakening law and rigidity of the surrounding rock, simulating events with high and low radiated seismic energy magnitudes.

4.5 Parametric Studies

This section discusses the capability of the proposed numerical methodology in studying the earthquake mechanics on geologic scales. In sections 4.4.1.1, we showed that the fault slip-weakening behavior, shear stress drop, and loading system stiffness control the stability of slip in a direct shear test configuration. Here, the same approach is extended to examine relationships between seismic energy magnitudes, average slip, and rupture lengths while different slip-weakening responses under various loading stiffness values are tested. Natural variations in the slip-weakening behavior of faults and loading system stiffnesses help explain why certain geological structures are more seismically active than others. At this stage, there is no analytic solution for verifying modeling results, but we can compare them to

existing field studies on variations of radiated seismic energy with the seismic moment for shallow earthquakes (depth < 70 km). This is because we directly obtain the seismic energy radiated from a rupture by the developed numerical methodology. Once directly calculated, seismic energy can be compared with other estimates of a seismic event size such as the seismic moment rather than being dependent on them. Many researchers have provided globally recorded seismic data relating directly measured seismic energy to seismic moment for shallow, strike-slip earthquakes (Kanamori, 1994; Choy and Boatwright, 1995; Stein and Wysession, 2003). Considering geometric spreads of the seismic energy and moment variations in different studies, Equation 4.9 gives upper and lower bounds of scaled energy (E_{sc}), the ratio of radiated seismic energy to seismic moment, for the shallow, strike-slip earthquakes.

$$2.1 \times 10^{-5} < E_{sc} < 6.6 \times 10^{-4} \quad (4.9)$$

where the bounds accommodate 95% of the collected data for E_{sc} . Hereafter, we examine the consistency between the globally recorded range of E_{sc} in Equation 4.9 and numerically calculated E_{sc} for each simulation.

4.5.1 Characteristic Distances

This section provides insights into how the rupture length, average slip, and radiated seismic energy change with D_c . We use the same initial and residual friction strengths as used in Figure 4.2b to simulate four cases of fault responses while the rock rigidity is kept constant at 12.5 GPa. Different cases are simulated by assigning 1, 2, 4, 5 mm joint roughness values to the CY constitutive model, resulting in characteristic distances of 8, 13, 18, and 23 mm, respectively.

Solid curves in Figure 4.7a show the shear stress and slip recorded on the element at the center of the rupture plane for each case. The characteristic distance of 8 mm is shown in Figure 4.7, indicating that the lowest characteristic distance simulates the most abrupt stress drop. Approximated GRCs for different responses are also included in Figure 4.7a to provide insight to the reasoning behind changes in radiated seismic energy while D_c varies. Dashed lines in Figure 4.7a suggest approximated GRCs with slopes ranging from 0.5 to 0.7 MPa/mm. GRCs here are approximated because referring to Equation 4.4, the rupture length is in a direct relationship with the GRC slope (loading system stiffness).

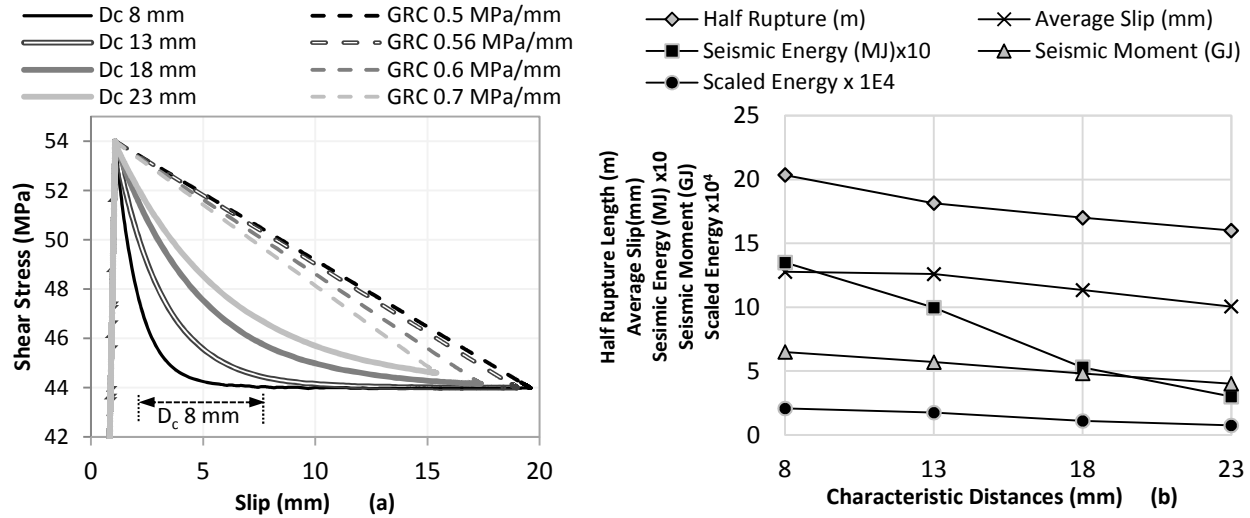


Figure 4.7 Role of D_c in rupture characteristics: (a) Shear stress versus slip curves recorded at the center of the rupture plane for responses with different D_c ; (b) Role of D_c in radiated seismic energy, slip, and rupture length.

Figure 4.5 showed that the rupture has a progressive nature, meaning that the total rupture length increases as the localized rupture propagates. Therefore, the incremental rupture length progressively decreases the GRC slope. However, for a rough illustration of changes in energy components, we ignore the progressive decay of GRC slopes and approximate GRCs as lines connecting initial and final states of the rupture. That is, the slope of GRCs for each element is approximated as the ratio of the stress drop to the slip along the element. Dieterich and Kilgore (1996) used a similar linear approximation for obtaining the loading system stiffness.

The rupture along the fault in the cases of D_c being 18 and 23 mm are arrested before the stress level reaches the residual strength of 44 MPa. This is because W_p , the area below the stress-slip curves in these cases, is relatively high and consumes most of $W + \Delta U$, the area below respective GRCs, and result in immature rupture arrests. That is, the rupture is terminated before the slip reaches the characteristic distance D_c and relatively insignificant energy is radiated. By contrast, cases with 8 and 13 mm D_c show a mature rupture where W_p is much lower than $W + \Delta U$, allowing a full drop of the shear stress from 54 to 44 MPa along with a significant seismic energy radiation.

Figure 4.7b shows that the lowest characteristic distance of 8 mm gives highest seismic energy magnitude of 1.35 MJ. Linearly decreasing the characteristic distance from 23 mm to 8 mm increases the seismic energy magnitude from 0.3 to 1.35 MJ (350% increase). If one establishes a level of radiated energy of, for example, 0.7 MJ for demarcating an aseismic limit, it can be inferred from Figure 4.7b that natural variations of D_c can rapidly turn a rupture into an aseismic slip. The average slip, rupture length,

and seismic moment increase from 10 to 12.8 mm, from 32 to 40.6 m, and from 4 to 6.5 GJ (65% increase), respectively, with decreasing the characteristic distance from 23 to 8 mm. This means that variations in D_c have more profound effects on the rupture length than the slip magnitude. The significant difference between 63% increase of seismic moment and 350% increase of radiated seismic energy with decreasing D_c implies the ineffectiveness of the seismic moment as a measure of the intensity of a rupture. Note that the strain energy U_i , the model dimensions, and the rigidity of rock are all the same for the four cases of fault responses but the average slip, rupture length, and seismic energy vary between cases. That is, rupture characteristics in Figure 4.7b are not defined by U_i but dictated by W_p or more specifically by fracture energy magnitudes. For all cases, scaled energy E_{sc} stays within the range of the field observations in Equation 4.9.

4.5.2 Loading System Stiffness

We showed in section 4.4.1.1 that rigidity of the rock surrounding the interface in the direct shear test is one of the elements impacting the loading system stiffness or the slope of GRCs and accordingly the magnitude of radiated seismic energy. Using frictional properties with $D_c=8$ mm, we simulate a rupture and study variations of the rupture length, average slip, seismic moment, and seismic energy magnitude with different loading system stiffness values. Values of the loading system stiffness are varied by changing the rock rigidity while the fault characteristic distance of 8 mm is kept constant between simulations. Figure 4.8a plots shear stress-slip curves along the fault surrounded by rocks with rigidity values of 10, 20, 30, and 40 GPa, yielding loading system stiffness values of 0.5, 1, 1.5, and 2 MPa/mm, respectively. With the same reasoning that was provided in the previous section, we plot the approximated GRCs in Figure 4.8a. As shown for the case with rigidity 10 GPa, the loading system stiffness values dictate GRC slopes.

Figure 4.8b satisfies the expected decreasing trend of radiated seismic energy as the loading system stiffens. The average slip decays almost exponentially from 14 to 4 mm while rupture length reduces almost linearly from 36 to 32 m with increasing the loading system stiffness. This means that variations in loading system stiffness have more profound effects on the slip magnitudes than on the rupture length. For the stiff system with the rigidity of 40 GPa, less energy can be stored as U_i so less energy is available for overcoming W_p , leading to an immature rupture and relatively insignificant radiated seismic energy.

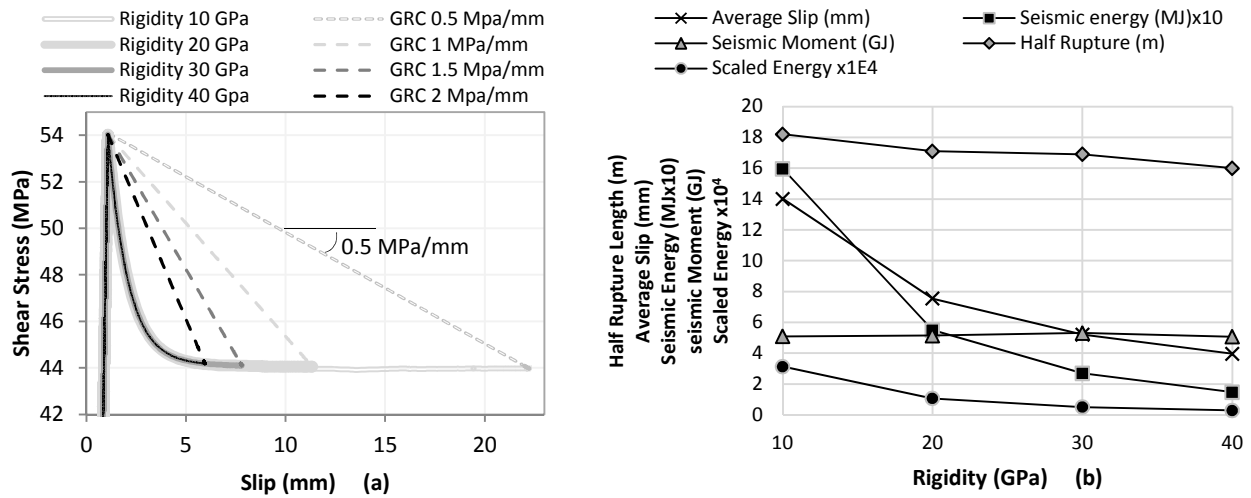


Figure 4.8 Role of rock rigidity in: (a) slip and GRC recorded at the fault center; (b) rupture length, average slip, seismic moment, and seismic energy.

For soft systems, relatively higher strain energy accumulated in the rock is enough to overcome W_p , drive the slip, and radiate significant seismic energy. With increasing the rigidity from 10 to 40 GPa, the seismic energy decreases from 1.6 to 0.15 MJ while the seismic moment stays almost constant. As a result, the seismic moment fails to represent rupture intensity or the seismic energy magnitude between cases because the moment does not account for all elements contributing to the slip instability, including stress drop and characteristic distances. The scaled energy for simulations in Figure 4.8b are again found to be within the range provided by Equation 4.9.

4.6 Discussions

The main contribution of this chapter was to develop a numerical methodology for modeling dynamic rupture and considering the energy transfer as a means for studying seismic events. Through this process, we were able to also evaluate relationships between the main geological parameters that play role in slip instability. By modeling idealized rupture progressions, we showed that different combinations of slip-weakening behavior, stress drop, loading system stiffness, and loading conditions can result in rupture evolution and arrest. Natural variations in the loading system stiffness and characteristic distance can help understand why in some geologic areas creep occurs along a fault and in others, high magnitude events are observed. Although the required conditions for instability may change between geologic settings, the significant radiation of seismic energy stays as a common signature for seismicity.

Studying changes in seismic moments and radiated seismic energy in Figures 4.7b and 4.8b, we showed that seismic moment may not be an effective representative of the rupture intensity although the

scaled energy calculated from the modeling results were in the range proposed by Equation 4.9. The inconsistency between changes in seismic moment and energy in different cases is more obvious in Figure 4.8b where seismic energy decays with increasing the rock rigidity while seismic moment remains constant.

In this chapter, we used a slip-weakening constitutive law which was necessary for energy conservation in the faulting system. We defined an initial shear strength based on a prescribed initial friction coefficient. Once the stress on the fault reached this initial strength, slip started to increase from zero while the shear strength reduced to the residual strength defined by a prescribed residual friction coefficient. Although the friction coefficients were priori constraints, the initial and residual strengths were free to change based on variations in normal stresses during loading and faulting. One of the main improvements that can be made to this chapter is to apply the slip-rate dependent laws for studying earthquake cycles. Future studies are required to define the change in the strength as a function of both slip and slip velocity. Slip along the fault accelerates as the rupture initiates. Once slip is larger than the slip-weakening distance D_c , the slip velocity starts reducing and becoming the dominant parameter that controls the friction. This means, reducing the slip velocity increases the shear strength and charge the fault for the next slip (Madariaga et al., 1998). This way energetics of cyclic earthquakes can be simulated and investigated in detail.

4.7 Conclusions

An energy-based numerical methodology is developed for dynamic modeling of rupture triggered by a slip-weakening fault response. An idealized strike-slip fault model is activated and rupture energetics and characteristics are shown to be within 1 to 5% error of available analytic solutions. We show the pulse-like behavior of slip and energy radiated from each energy source by using the instability concept. The globally recorded variations of scaled energy for shallow earthquakes also confirm the numerical calculation of radiated seismic energy. Parametric studies on the simulated fault show that the developed methodology is capable of differentiating rupture from aseismic slip events and that different combinations of the shear stress drop, characteristic distance, and loading system stiffness result in a rupture characterized by a significant release of seismic energy. While this combination may vary between geological settings, we show that the radiated seismic energy remains as a common signature of seismic events. The developed approach for modeling rupture shows that once the quasi-static shear stress on the nucleation zone exceeds the initial frictional strength on one patch, external loading of the fault is no longer needed to drive a rupture if conditions for instability emerge. Rupture evolution and arrest are then governed by magnitudes of available energy for the rupture and energy consumed during the faulting. The inconsistency between the seismic moment and seismic energy variations in parametric

studies suggests that seismic moment may not be a representative measure for rupture intensity. The methodology provides a useful framework for studying variations of radiated seismic energy with slip velocity, rupture length, slip magnitudes, and seismic moment in more detail. Given the verification examples provided in the present chapter, one can simulate fault zones with heterogeneous fault frictional behaviors and rock properties for assessing seismic hazards by relying on the proposed seismic energy calculation.

4.8 Reference

- Andrews, D.J., 1985. Dynamic plane-strain shear rupture with a slip-weakening friction law calculated by a boundary integral method. *Bull. Seismol. Soc. Am.* 75, 1–21.
- Andrews, D.J., 1976. Rupture velocity of plane strain shear cracks. *J. Geophys. Res.* 81, 5679–5687. <https://doi.org/10.1029/JB081i032p05679>
- Archambeau, C.B., 1968. General theory of elastodynamic source fields. *Rev. Geophys.* 6, 241. <https://doi.org/10.1029/RG006i003p00241>
- Barton, C.A., Zoback, M.D., Moos, D., 1995. Fluid flow along potentially active faults in crystalline rock. *Geology* 23, 683–686. [https://doi.org/10.1130/0091-7613\(1995\)023<0683:FFAPAF>2.3.CO](https://doi.org/10.1130/0091-7613(1995)023<0683:FFAPAF>2.3.CO)
- Beeler, N.M., 2001. Stress drop with constant, scale independent seismic efficiency and overshoot. *Geophys. Res. Lett.* 28, 3353–3356. <https://doi.org/10.1029/2001GL012906>
- Beroza, G.C., Mikumo, T., 1996. Short slip duration in dynamic rupture in the presence of heterogeneous fault properties. *J. Geophys. Res. Solid Earth* 101, 22449–22460. <https://doi.org/10.1029/96JB02291>
- Bizzarri, A., 2010. Pulse-like dynamic earthquake rupture propagation under rate-, state- and temperature-dependent friction. *Geophys. Res. Lett.* 37, n/a-n/a. <https://doi.org/10.1029/2010GL044541>
- Bouchon, M., 1997. The state of stress on some faults of the San Andreas System as inferred from near-field strong motion data. *J. Geophys. Res. Solid Earth* 102, 11731–11744. <https://doi.org/10.1029/97JB00623>
- Brune, J.N., 1970. Tectonic stress and the spectra of seismic shear waves from earthquakes. *J. Geophys. Res.* 75, 4997–5009. <https://doi.org/10.1029/JB075i026p04997>
- Choy, G.L., Boatwright, J.L., 1995. Global patterns of radiated seismic energy and apparent stress. *J. Geophys. Res. Solid Earth* 100, 18205–18228. <https://doi.org/10.1029/95JB01969>
- Cohee, B.P., Beroza, G.C., 1994. Slip distribution of the 1992 Landers earthquake and its implications for earthquake source mechanics. *Bull. Seismol. Soc. Am.* 84, 692–712.
- Cook, N.G.W., 1966. The design of underground excavations, in: *Eighth Symposium on Rock Mechanics, University of Minnesota, in Failure and Breakage of Rock.* pp. 167–193.
- Cook, N.G.W., 1965. A note on rockbursts considered as a problem of stability. *J. South African Inst. Min. Metall.* 65, 437–446.
- Cotton, F., Campillo, M., 1995. Frequency domain inversion of strong motions: Application to the 1992 Landers earthquake. *J. Geophys. Res. Solid Earth* 100, 3961–3975. <https://doi.org/10.1029/94JB02121>
- Cundall, P.A., Lemos, J., 1990. Rockbursts and seismicity in mines, in: *Numerical Simulation of Fault Instabilities with the Continuously-Yielding Joint Model.* pp. 379–387.

- Das, S., Aki, K., 1977. Fault plane with barriers: A versatile earthquake model. *J. Geophys. Res.* 82, 5658–5670. <https://doi.org/10.1029/JB082i036p05658>
- Day, S.M., Yu, G., Wald, D.J., 1998. Dynamic stress changes during earthquake rupture. *Bull. Seismol. Soc. Am.* 88, 512–522.
- Dieterich, J.H., 1979. Modeling of rock friction: 1. Experimental results and constitutive equations. *J. Geophys. Res.* 84, 2161. <https://doi.org/10.1029/JB084iB05p02161>
- Dieterich, J.H., 1978. Time-dependent friction and the mechanics of stick-slip. *Pure Appl. Geophys. PAGEOPH* 116, 790–806. <https://doi.org/10.1007/BF00876539>
- Dieterich, J.H., Kilgore, B., 1996. Implications of fault constitutive properties for earthquake prediction. *Proc. Natl. Acad. Sci. U. S. A.* 93, 3787–94.
- Duvall, W.I., Stephenson, D.E., 1965. Seismic energy available from rockbursts and underground explosions. *Trans. Soc. Min. Eng.* 232, 235–240.
- Favreau, P., Archuleta, R.J., 2003. Direct seismic energy modeling and application to the 1979 Imperial Valley earthquake. *Geophys. Res. Lett.* 30, n/a-n/a. <https://doi.org/10.1029/2002GL015968>
- Gheibi, A., Hedayat, A., 2018. Ultrasonic investigation of granular materials subjected to compression and crushing. *Ultrasonics* 87, 112–125. <https://doi.org/10.1016/j.ultras.2018.02.006>
- Goodman, R.E., Sundaram, P.N., 1978. Fault and system stiffness and stick-Slip phenomena. *Pure Appl. Geophys.* 116, 871–887.
- Haeri, S.M., Hosseini, A.M., Shahrabi, M.M., Soleymani, S., 2015. Comparison of Strength Characteristics of Gorgan Loessial Soil Improved by Nano- Silica, Lime and Portland Cement, in: 15th Pan American Conference on Soil Mechanics and Geotechnical Engineering.
- Haskell, N.A., 1964. Total energy and energy spectral density of elastic wave radiation from prom propagating faults. *Bull. Seismol. Soc. Am.* 54, 1811–1841.
- Heaton, T.H., 1990. Evidence for and implications of self-healing pulses of slip in earthquake rupture. *Phys. Earth Planet. Inter.* 64, 1–20. [https://doi.org/10.1016/0031-9201\(90\)90002-F](https://doi.org/10.1016/0031-9201(90)90002-F)
- Ida, Y., 1972. Cohesive force across the tip of a longitudinal-shear crack and Griffith's specific surface energy. *J. Geophys. Res.* 77, 3796–3805. <https://doi.org/10.1029/JB077i020p03796>
- Ide, S., 2002. Estimation of radiated energy of finite-source earthquake models. *Bull. Seismol. Soc. Am.* 92, 2994–3005.
- Ide, S., Takeo, M., 1997. Determination of constitutive relations of fault slip based on seismic wave analysis. *J. Geophys. Res. Solid Earth* 102, 27379–27391. <https://doi.org/10.1029/97JB02675>
- Itasca, 2016. Background - The 2D Distinct Element Method, UDEC Manual.
- Jaeger, J.C., Cook, N.G.W., 1976. *Fundamentals of rock mechanics*. Chapman and Hall LTD.
- Kanamori, H., 1994. Mechanics of earthquakes. *Annu. Rev. Earth Planet Sci.* 22, 207–237.
- Kanamori, H., Anderson, D.L., 1975. Theoretical basis of some empirical relations in seismology. *Bull. Seismol. Soc. Am.* 65, 1073–1095.
- Kaneko, Y., Shearer, P.M., 2015. Variability of seismic source spectra, estimated stress drop, and radiated energy, derived from cohesive-zone models of symmetrical and asymmetrical circular and elliptical ruptures. *J. Geophys. Res. Solid Earth* 120, 1053–1079. <https://doi.org/10.1002/2014JB011642>
- Karner, S.L., Marone, C., 2000. Effects of loading rate and normal stress on stress drop and stick-slip recurrence interval. *American Geophysical Union*, pp. 187–198.

<https://doi.org/10.1029/GM120p0187>

- Khademian, Z., Nakagawa, M., Garvey, R., Ozbay, U., 2017. Role of fluid injection pressure in inducing seismicity, in: Proceedings of the 42nd Workshop on Geothermal Reservoir Engineering. p. 10.
- Kostrov, V. V., 1974. Seismic moment and energy of earthquakes, and seismic flow of rock. *Earth Phys.* 1, 23–40.
- Lockner, D.A., Beeler, N.M., 1999. Premonitory slip and tidal triggering of earthquakes. *J. Geophys. Res. Solid Earth* 104, 20133–20151. <https://doi.org/10.1029/1999JB900205>
- Ma, S., Archuleta, R.J., 2006. Radiated seismic energy based on dynamic rupture models of faulting. *J. Geophys. Res. Solid Earth* 111, n/a-n/a. <https://doi.org/10.1029/2005JB004055>
- Madariaga, R., 1976. Dynamic of an expanding circular fault. *Bull. Seismol. Soc. Am.* 66.
- Madariaga, R., Olsen, K., Archuleta, R., 1998. Modeling dynamic rupture in a 3D earthquake fault model. *Bull. Seismol. Soc. Am.* 88, 1182–1197.
- Madariaga, R., Olsen, K.B., 2000. Criticality of rupture dynamics in 3-D. *Pure appl. Geophys* 157.
- Madariaga, R., Olsen, K.B., 1997. Earthquake dynamics, in: *Earthquake Dynamics*. pp. 0–12.
- Olsen, K.B., Matarese, J.R., Archuleta, R.J., 1997. Three-dimensional dynamic simulation of the 1992 Landers earthquake. *Science* (80-.). 270, 1628–1632. <https://doi.org/10.1126/science.270.5242.1628>
- Peyrat, S., Olsen, K., Madariaga, R., 2001. Dynamic modeling of the 1992 Landers earthquake. *J. Geophys. Res. Solid Earth* 106, 26467–26482. <https://doi.org/10.1029/2001JB000205>
- Prieto, G.A., Florez, M., Barrett, S.A., Lopez, G.A., Beroza, G.C., 2012. Earthquake source scaling, stress drops and seismic efficiency of intermediate-depth earthquakes. *Geophys. Res. Abstr. EGU Gen. Assem.* 14, 2012–5287.
- Rice, J.R., 1983. Constitutive relations for fault slip and earthquake instabilities. *Pure Appl. Geophys.* 121, 443–475. <https://doi.org/10.1007/BF02590151>
- Ruina, A., 1983. Slip instability and state variable friction laws. *J. Geophys. Res. Solid Earth* 88, 10359–10370. <https://doi.org/10.1029/JB088iB12p10359>
- Ryder, J. a., 1988. Excess shear stress in the assessment of geologically hazardous situations. *J. South African Inst. Min. Metall.* 88, 27–39.
- Salamon, M.D.G., 1984. Energy considerations in rock mechanics: fundamental results 84, 233–246.
- Salamon, M.D.G., 1974. Rock mechanics of underground excavations. *Advances in Rock Mechanics*, in: 3rd Cong Int Soc Rock Mech. pp. 951–1099.
- Sato, T., Hirasawa, T., 1973. Body wave spectra from propagating shear cracks. *J. Phys. Earth* 21, 415–431. <https://doi.org/10.4294/jpe1952.21.415>
- Savage, J.C., 1966. Radiation from a realistic model of faulting. *Bull. Seismol. Soc. Am.* 56, 577–592.
- Stein, S., Wysession, M., 2003. *An introduction to seismology, earthquakes, and earth structure.* Blackwell Pub.
- Wald, D.J., Heaton, T.H., 1994. Spatial and temporal distribution of slip for the 1992 Landers, California earthquake. *Bull. Seismol. Soc. Am.* 84, 668–691.
- Wong, T.-F., 2013. On the normal stress dependence of the shear fracture energy. *American Geophysical Union*, pp. 1–11. <https://doi.org/10.1029/GM037p0001>

CHAPTER 5

MODELING INJECTION-INDUCED SEISMICITY THROUGH CALCULATION OF RADIATED SEISMIC ENERGY

A manuscript published in the *Journal of Natural Gas Science and Engineering*

Zoheir Khademian, Masami Nakagawa, and Ugur Ozbay

5.1 Abstract

Seismicity induced by the injection of fluid into the fractured ground is one of the most challenging issues facing geothermal and deep wastewater disposal industries. This chapter extends the developed framework to simulate injection-induced seismicity and study roles of injection pressure in triggering rupture (seismic slip) along preexisting faults. The framework uses the Universal Distinct Element Code (UDEC) with its quasi-static and dynamic schemes and calculates the total seismic energy radiated by a rupture when more energy is made available in the system than can be stored or consumed. We study the effects of fluid injection on rupture dynamics by pressurizing a single fault surrounded by impermeable rock, representing a simplified analogy for the injection process in deep wastewater disposal and geothermal activities. Along with developing the methodology, we study effects of raising the fluid pressure on initiating rupture over well-oriented (or critically loaded) and misoriented faults. Results show that fluid injection can trigger a rupture along both well-oriented and misoriented faults although the notion of seismicity may be observed along the well-oriented fault as early as the beginning of the injection process. The well-oriented fault generates higher seismic energy magnitude as more energy is available for rupture due to the higher peak shear stress and stress drop on the fault. Making simplifying assumptions, this study also found that fluid can be injected under a high-pressure increment before and after the fault initial activation while the radiated seismic energy remains relatively insignificant. However, gradually increasing the fluid pressure at the onset of rupture reduces the radiated seismic energy by 30%. Comparing the seismic moment and radiated seismic energy for each event reveals that while radiated seismic energy varies between different values of pressure increment, the calculated seismic moment stays constant, showing the possible ineffectiveness of the seismic moment in representing the intensity of injection-induced ruptures.

5.2 Introduction

Fluid injection into deep underground formations can be followed by seismic events characterized by a significant release of the strain energy stored in the rock. Hydraulic fracturing in unconventional hydrocarbon reservoirs (Rutqvist et al., 2013), enhanced geothermal systems (Majer et al., 2007), and deep wastewater injection fields (Zhang et al., 2013) have been shown to contribute to the recent rise in the number and magnitude of seismic events in the US. Figure 5.1 shows reported injection-induced events with their maximum magnitudes in wastewater disposal, enhanced geothermal, and hydraulic fracturing projects. In this figure, the wastewater disposal sites are shown to be associated with highest-magnitude events.

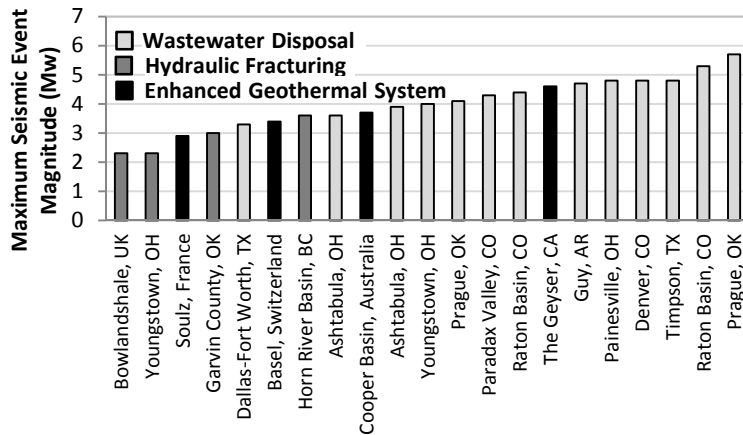


Figure 5.1 Maximum magnitudes of seismic events related to different fluid injection settings (BC Oil and Gas Commission, 2012; Cladouhos et al., 2010; Frohlich et al., 2008; Keranen et al., 2013; Majer et al., 2007; McClure and Horne, 2014; McGarr, 2014; Richards et al., 1994; Shapiro et al., 2007).

Injection-induced events mainly occur due to the activation of preexisting faults. One of the main fault activation mechanisms is the loss of fault confinement (or effective normal stress) caused by the elevated pressure between fault planes (Ellsworth, 2013). Fluid pressure increases between fault plates if the fault and surrounding rock formations with relatively low permeability do not accommodate the injected fluid volume. The elevated fluid pressure within the fault re-distributes in-situ stresses in a way that reduces the capacity of the surrounding rockmass in storing strain energy. Slip (cumulative shear displacement discontinuity) on the fault is a way to dissipate the excess strain energy that becomes available but cannot be stored in the rock. The stimulated slip can occur either in a violent mode (seismic slip or rupture) that results in radiating seismic energy or in non-violent mode (aseismic or stable slip) in which the excess strain energy is fully consumed during the faulting.

The challenge is to utilize mechanical modeling to anticipate the evolution of a rupture while injecting fluid underground and to understand how the operational variables such as injection pressure can be adjusted to minimize the intensity of the induced rupture. Mechanical modeling of rupture demands relying on a measure that reflects the rupture intensity. Selecting a representative measure requires an understanding of conditions under which seismicity emerges. Attempts have been made to study conditions leading to a slip, to identify a seismic slip or rupture, and to estimate the timing and magnitude of these unstable failures. Dieterich (1979) and Rice (1983) used a box-spring system with one degree of freedom and showed that slip along a discontinuity is aseismic for a sufficiently stiff spring and is seismic for spring with stiffness less than a critical one. Ryder (1988) studied several possible distributions of the Excess Shear Stress (ESS), the difference between the shear stress and the dynamic strength, along a preexisting fault. Board (1996) numerically implemented the ESS concept and used the ESS as an estimate of the seismic potential of a fault. Khademian et al. (2018) used a numerical direct shear test simulated by a distinct element code (UDEC) and exemplified a stable slip with a high ESS, showing that high ESS may not necessarily lead to seismicity. Modeling fractures by the displacement discontinuity method, Baisch et al. (2010) simulated fracture zones as individual patches which can slip independently. In this method, seismicity is assumed to occur whenever the shear stress on a patch exceeds its initial shear strength. However, Bourouis and Bernard (2007), Cornet et al. (1997), and Guglielmi et al. (2017) showed that shear slip along a fault cannot be the only indicator for instability as it is unable to explain the aseismic slip observed in injection fields.

Zoback et al., 2012 performed a series of rate and state friction experiments and showed that lack of clay and kerogen within discontinuity plates reduces the characteristic distance and leads to a rupture. Khademian et al. (2018, 2017) used the instability notion developed by Rice (1983) and numerically showed examples of aseismic slip and rupture along a discontinuity with relatively short characteristic distance. They concluded that slip-weakening characteristics of a discontinuity contribute to the instability of the slip only if the loading system stiffness is low enough. They showed that loading system stiffness is in a direct relationship with the rock shear modulus, and in an inverse relationship with the slip area. The fault orientation has been also proposed as one of the elements contributing to the instability of a slip (Zoback et al., 2012). A fault that is not oriented in favor of a shear slip, with respect to principal stress directions, is called a misoriented fault while critically stressed faults are referred to as well-oriented faults. Zoback et al. (2012) conducted research on the mechanism of aseismic shear slips during hydraulic fracturing stimulation and argued that injection can only induce aseismic slip if the fault is misoriented.

McClure and Horne (2011) modeled induced seismicity along a single discontinuity during high-pressure fluid injection which was simulated by unsteady-state mass balance equations. They used a rate- and-state dependent constitutive law and defined a seismic slip whenever the slip velocity exceeds 5 m/s. The seismic moment (product of the slip area, average slip, and rock shear modulus) was then used as the measure for the rupture intensity. Rutqvist et al. (2013) conducted numerical simulation studies to assess the potential for injection-induced rupture and notable seismic events associated with shale-gas hydraulic fracturing operations. They modeled injection process under different injection rate, simulated by unsteady-state fluid flow equations. They assumed a seismic slip occurs when the shear stress exceeds the shear strength of the fault and a sudden discontinuous dislocation is observed. They relied on the seismic moment for estimating the intensity of a seismic slip.

Results of modeling rupture progression in chapter 4 showed that different combinations of fault slip-weakening characteristics, the initial shear strength of the fault, shear stress drop, loading system stiffness, and loading conditions can result in the seismic slip evolution and propagation. It was also shown that although this specific combination may change between geologic settings, the significant radiation of seismic energy stays as a common signature for seismicity (Khademian et al., 2018, 2017, 2016). The main objective of this chapter is to develop numerical methodologies to explore injection-induced rupture by investigating the state of energy before and after a shear slip. As a result, this work excludes studying the significant roles of different fault slip-weakening behaviors and system loading stiffness values in the intensity of a rupture. Instead, we exemplify injection-induced ruptures to show the possible application of the developed methodology and its capability in investigating underlying mechanisms of an induced event. Contrary to the widely used seismic moment, we directly estimate radiated seismic energy as a measure of the rupture intensity and show the ineffectiveness of the seismic moment as an intensity estimate of induced events.

We first simulate strike-slip fault activation and calibrate the mesh geometry and loading conditions by checking the results against analytical solutions with respect to the rupture length, average slip, radiated seismic energy, and seismic moment. The methodology and modeling approach are then further extended for exploring injection-induced seismicity along well-oriented and misoriented faults simulated by a Mohr-Coulomb friction law with residual strength. We assume the elastic rock matrix is impermeable and different fluid injection patterns can be simulated by steady-state pressure increments. Simulating different injection patterns with these simplifying assumptions reduces the natural complexity of induced seismicity and allows better understanding the instability notion and mechanics of the injection-induced rupture.

5.3 Methodology

The total energy available for a slip is distributed between radiated energy, and the sum of energy that is dissipated or stored within the source by processes, mainly including frictional heating and fracturing. Increasing the energy dissipation in the source will decrease the amount of radiated energy (Prieto et al., 2012), a concept that this chapter numerically translates to a methodology for obtaining the magnitude of the radiated energy.

5.3.1 Balance of Energy Transfer

Gravitational and remotely applied tectonic loading are the major external forces that generate the steady deformation of rockmass, resulting in accumulating the strain energy (U_i) prior to the slip. The active external forces can also produce the external work (W) as the slip occurs. The work done by the fluid pressure (W_{inj}) within the affected fault re-distributes local stresses, and reduces the energy storing capacity of rocks surrounding the fault. A slip along the fault can release the excess strain energy that becomes available but cannot be stored in the rock. Slip does not necessarily lead to a complete exhaustion of the stored energy and some residual strain energy (U_r) may remain in the fault system (Brune, 1970). The triggered slip can accompany dissipative energy terms of plastic work (W_p) and radiated seismic energy (W_k). W_p is generated by the friction work and inelastic deformation of the surrounding rock. If the partial release of the strain energy is fully consumed by W_p the slip is aseismic and thus near zero W_k is radiated. However, in the course of a seismic slip, the strain energy release is not completely exhausted by W_p but is released in the form of radiated seismic energy W_k (Salamon 1970; Rice 1983). The transfer of energy can be summarized by an energy balance as shown in Equation 5.1 where the left-hand side shows the state of energy before slip and right-hand side represents the post-slip state of energy.

$$W + U_i + W_{inj} = W_p + U_r + W_k \quad (5.1)$$

Rearranging the energy balance, we can calculate the seismic energy radiated from a slip as

$$W_k = W + \Delta U + W_{inj} - W_p \quad (5.2)$$

where ΔU is the strain energy release, the difference between U_i and U_r . The mechanical damping of the Distinct Element Method (DEM) scheme in UDEC also allows dynamic calculations of radiated seismic energy. In order to reach a solution of static equilibrium for each dynamic system, UDEC extracts a fraction of the kinetic energy of the system at each time step and cumulatively records them as damped

work (W_D). The remaining kinetic energy (U_k) in the system is zero as the model reaches equilibrium and is high during the simulation of a dynamic response (Poeck et al., 2016). The radiated seismic energy calculation based on the kinetic terms in the system is governed by Equation 5.3 (Itasca, 2016).

$$W_k = U_k + W_D \quad (5.3)$$

Chapters 4 and 2 showed that the radiated seismic energy calculated by the dynamic approach of Equation 5.3 is in agreement with results of Equation 5.2 and those of analytical solutions provided by Duvall and Stephenson (1965), Salamon (1984), and Cook (1966). We hesitate to provide approximations for energy terms in Equations 5.1-3 as they depend on various parameters, including the fault frictional properties, geological features, the rigidity or shear modulus of rock formations, in-situ stress magnitudes and directions at the time of slip, fault development, injection depths, and fluid injection patterns. For this reason, the best way of estimating the radiated seismic energy magnitude is deterministic or probabilistic (depending on the data acquisition uncertainties) numerical modeling of an injection field. The numerical modeling also allows adjusting operational parameters like injection well location, injection rate, and downhole pressure in order to minimize the potentials for high-magnitude rupture events. Note that depending on the capability of numerical modeling tools, radiated seismic energy can be calculated by either Equation 5.2 or 5.3. This chapter first simulates a fault activation, without fluid injection, and calibrates the rupture model mesh geometry and loading conditions by comparing the results with analytical solutions given by Ryder (1988). Then, we further develop the methodology to study seismicity induced by fluid injection onto a preexisting fault.

5.3.2 Calibrating Dynamic Rupture Model

Most large seismic events occur along preexisting faults but rupture is finite and does not involve the entire fault area (Fukuyama, 2009). Finite rupture can be simulated on a thoroughgoing fault surrounded by rocks such that rupture is terminated once the driving energy of ΔU dissipates and W fails to overcome the shear strength of the unloaded segments. However, loading conditions and mesh geometry of the fault model need a careful calibration. Fault loading conditions define shear and normal stress distributions along the simulated fault and drive the rupture initiation location, rupture length, and the magnitude of seismic energy radiated by the rupture. The mesh geometry along the fault also affects the shear slip localization and thus the rupture initiation location (Madariaga et al., 1998). In order for calibrating the fault model in terms of mesh geometry and loading conditions, we employ analytical solutions derived by Ryder (1988) for fault activation. Ryder (1988) developed analytical functions for possible shear stress distributions along a fault. The shear stress distribution is defined by Excess Shear

Stress (ESS) that is the difference between the fault shear stress and the fault dynamic strength. For calibration process, we use the symmetrical ESS distribution that is defined as a function of the \widehat{ESS} peak value, given as

$$ESS(x) = \widehat{ESS} (1 - x^2) \quad (5.4)$$

where x denotes a dimensionless function variable changing between -1 and 1. The ESS profile drives the slip distribution along the fault as

$$Ride(x) = \widehat{ESS}(2 - x^2)^{1.5} a \sqrt{4(1 - \nu^2)}/3E \quad (5.5)$$

where a is the half-width of the ESS profile length. E denotes Young's modulus and ν is the Poisson ratio of the rock surrounding the fault. For the symmetrical ESS profile in Equation 5.4, Ryder (1988) approximated the seismic moment and radiated seismic energy, respectively, as

$$M_o = 2.5 \widehat{ESS} \times a^2 \times l \quad (5.6)$$

$$W_k = \frac{\overline{ESS} \times M_o}{2G} \quad (5.7)$$

where l is the strike length of the fault, which equals 1 as the analysis is two dimensional. \overline{ESS} is the average value of the distributed ESS along the fault. We simulate a fault with a strike-slip focal mechanism (Figure 5.2) and calibrate the loading condition and mesh geometry such that modeling results match the symmetrical distributions in Equations 5.4 and 5.5. The choice of strike-slip focal mechanism is for the purpose of modeling simplifications without loss of generality. Based on the recorded depth of the recent induced events in Oklahoma, USA (Earthquaketrack, 2017; U.S. Department of Energy, 2017), we assume an average depth of 3.6 km for in-situ stress calculations. Assuming that the fault focal mechanism is strike-slip, a constant normal stress of 90 MPa is applied over the fault. The fault is assigned an initial friction coefficient of 0.6 that is the commonly observed lower limit value for the laboratory samples of most common rocks and is also confirmed by field observations (Barton et al., 1995).

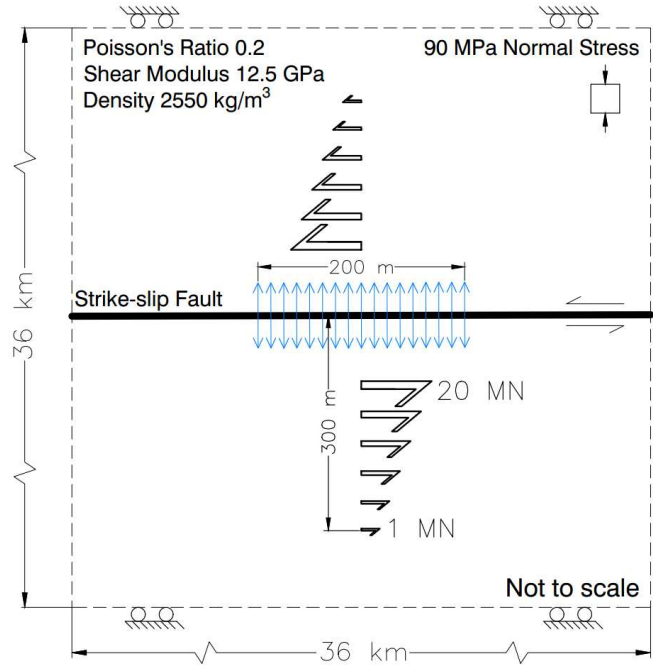


Figure 5.2 Schematic plan view of the strike-slip fault model domain with initial and boundary conditions. Blue arrows represent the pressurized domain along the 200 m length of the fault.

Dynamic and residual friction coefficients are assumed 0.49 that falls within ranges of both dynamic and residual friction coefficients reported by laboratory observations (Beeler, 2001; Karner and Marone, 2000; Lockner and Beeler, 1999; Wong, 2013). Figure 5.3 suggests the frictional behavior assigned to each element along the fault. Assuming the 0.6 and 0.49 initial and residual friction coefficients, initial and residual fault strengths equal 54 and 44 MPa, respectively.

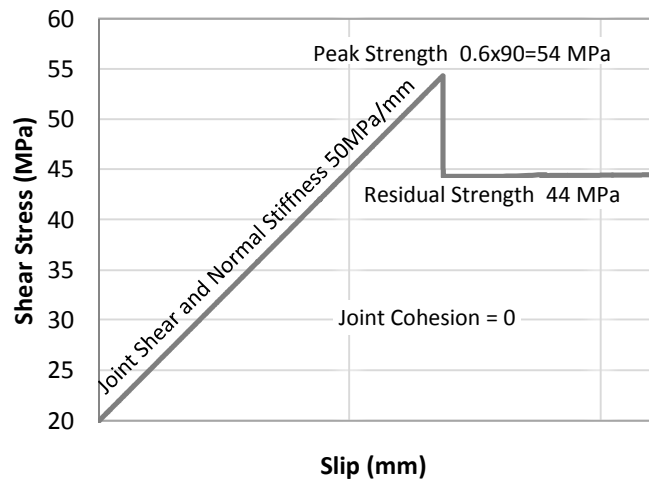


Figure 5.3 Frictional properties assigned to each element along the fault.

The calibration process excludes injection pressure and the fault is activated by a quasi-static increase of the local shear stresses applied over the fault. Distributed or concentrated couples can be applied to the model for developing local shear stress along the fault. A non-uniformly distributed couple following the pattern shown in Figure 5.2 with a mesh geometry following the maximum mesh size to rupture length ratio of 1:40 are found to match the symmetrical ESS distribution proposed by Equation 5.4. The fault is activated by a quasi-static increase in the magnitude of the distributed couple forces. Until local slip initiates, the magnitude of the couple forces increases and then remains constant. However, the rupture propagates since the release of the stored strain energy is large enough to continue supporting the slip propagation.

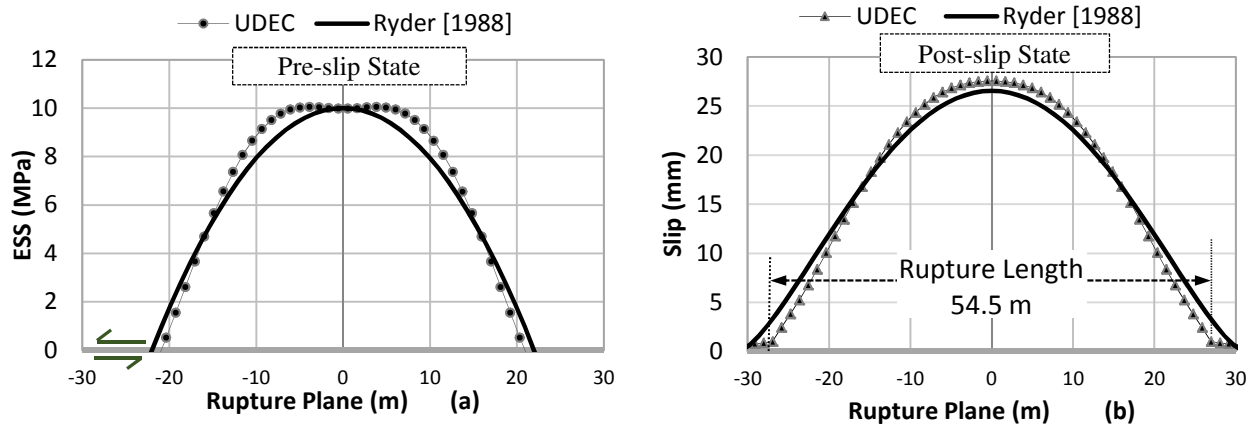


Figure 5.4 Comparison between analytical and numerical solutions for: (a) ESS profile; (b) slip along the fault.

Figure 5.4a suggests ESS or the shear stress distribution on the fault at the onset of slip while Figure 5.4b represents the slip distribution along the fault after rupture is arrested. The solid curves in Figures 5.4a and b represent the ESS and slip profiles obtained by Equations 5.4 and 5.5, respectively, while the dots are results of the simulated rupture in UDEC. Note that Equation 5.4 is normalized by the half width of the ESS profile (a), so for maintaining consistency between results in Figure 5.4a, the analytically calculated ESS is plotted against the width of the ESS profile obtained from UDEC. Table 5.1 shows the comparison between rupture modeling results and Ryder's calculations for rupture length, average slip, seismic moment, and radiated seismic energy.

Table 5.1 Comparison between Analytic Calculations by Ryder (1988) and UDEC Results.

Methods	\overline{ESS}	\overline{ESS}	Average slip	Half-width	Rupture length	Seismic moment	Radiated seismic energy
Ryder's method	10 MPa	7. MPa	16.6 mm	22. m	58. m	12.1 GJ	3.2 MJ
UDEC results	10 MPa	7.4 MPa	17.6 mm	20.6 m	54.5 m	12 GJ	3.4 MJ
Difference	0%	6%	6%	6%	6%	1%	6%

Note that the numerical seismic moment is based on the product of the rupture length, slip averaged along the rupture length, and shear modulus of the rock. The results of the maximum and average ESS, average slip, rupture length, and seismic energy are within 6% of the analytical solutions. The insignificant mismatching between the ESS obtained by analytical and UDEC calculations are the cause of the error because ESS profiles in Figure 5.4a drive the slip distributions in Figure 5.4b. The calibrated model allows a study on the triggering role of fluid pressure within well-oriented and misoriented faults with respect to the rupture energetics.

5.3.3 Energetics of Rupture

This section briefly provides some insight into the transfer of energy during the course of a rupture. Figure 5.5 shows the curve of the fault shear stress - slip averaged over the 54.5 m rupture length (Figure 5.4b) at each time step. Figure 5.5 also marks the pre- and post-slip states, corresponding to pre- and post-slip states of the stress and slip in Figures 5.4a and b, respectively.

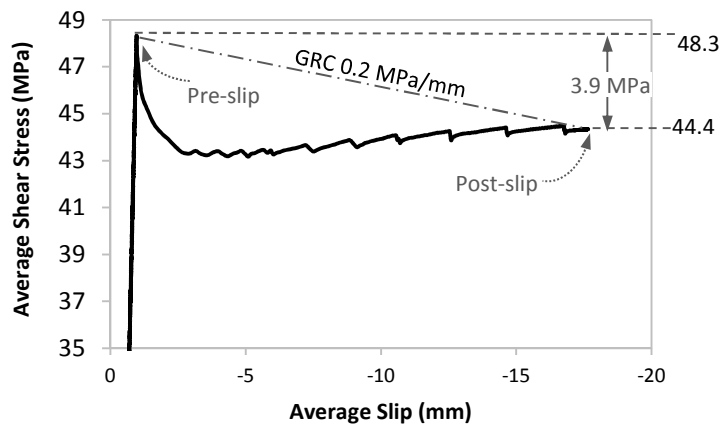


Figure 5.5 Average shear stress and slip showing the pre-slip and post-slip stress states. The shear stress and slip are averaged along the 54.5 m rupture length.

As shown in Figure 5.3, a stress drop of 10 MPa is assigned to each element on the fault; however, the average stress drop in Figure 5.5 is found to be about 4 MPa followed by some fluctuations. The fluctuations in the post-peak curve and the reduction in the stress drop originate from the averaging process and the progressive nature of a rupture. The first localized rupture occurs on the patch where the peak stress exceeds the fault shear strength of 54 MPa. However, the shear stress averaged over the rupture length denotes a peak of 48.3 MPa as other patches on the fault have not reached their peak stress of 54 MPa yet. The continued progression of the rupture activates neighboring patches while the pioneer ones are already at their post-peak state (Beroza and Mikumo, 1996; Khademian et al., 2018). Therefore, while we average shear stress and slip during the rupture, this incremental rupture results in a reduction in the average stress drop and fluctuations in the curve in Figure 5.5. Note that different averaging method may result in curves with different peak and residual stresses.

The concept of energy transfer during a rupture is shown by an estimated Ground Reaction Curve (GRC) in Figure 5.5. The GRC reflects the change in the shear stress within the rock surrounding a fault as slip occurs on the fault. The GRC for each element along a fault can be different, depending on the spatiotemporal order of rupture. However, an average GRC can be approximated by a linear extrapolation between initial and residual shear strength of the fault (Dieterich and Kilgore, 1996; Khademian et al., 2018) as shown in Figure 5.5. According to the instability notion by Rice (1983), and Salamon (1974, 1984), energy terms in Equation 5.2 can be quantified by comparing the shear stress-slip curve with the GRC. The area below the GRC in Figure 5.5 is $W + \Delta U$ and represents the energy density available for the rupture. The surrounding rock is assumed elastic, so there is no energy consumption due to rock fracturing and W_p is only attributed to the frictional slip. W_p is dictated by the fault slip-weakening behavior (which is not applied in these simulations) and stress drop and can be approximated by calculating the area below the post-peak curve of average shear stress-slip, multiplied by the rupture length. According to Equation 5.2, the area between the solid curve and GRC in Figure 5.5 represents W_k . Khademian et al. (2017, 2016) constructed an idealized model of rupture and showed that the magnitude of seismic energy radiated by a rupture depends on the slope of GRC, stress drop, slip-weakening rate, rock shear modulus, and the fault initial shear strength. Discussing these elements is outside the scope of this chapter but we use the concept of GRC for interpreting effects of fault orientations and injection pressure on the radiated seismic energy magnitude.

5.4 Modeling Injection-Induced Rupture

This section describes rupture induced by pressurizing the strike-slip fault. Here, we assume that the surrounding rock matrix is impermeable. Thus, the fluid leak-off into the surrounding rock formation

is not considered in the model, so the pressure buildup within the fault is the root cause of instability. That is, the reduction in effective stress (σ_{eff}), with associated loss of shear resistance, is assumed the main mechanism leading to the fault activation. The fluid pressure felt by the fault (P) counteracts the fault normal stress (σ_n) and thus reduces the effective stress on the fault. As shown by Equations 5.8 and 5.9, assuming the fault initial (φ_i) and residual (φ_r) friction angles stay unaffected, any decrease in σ_{eff} reduces the fault initial (τ_i) and residual (τ_r) shear strengths, respectively.

$$\tau_i = (\sigma_n - P) \times \tan(\varphi_i) = \sigma_{\text{eff}} \times \tan(\varphi_i) \quad (5.8)$$

$$\tau_r = (\sigma_n - P) \times \tan(\varphi_r) = \sigma_{\text{eff}} \times \tan(\varphi_r) \quad (5.9)$$

Fluid pressure reduces τ_i to the level of the local shear stress (τ) on the fault, resulting in a local rupture. According to Equation 5.9, the reduction in σ_{eff} also decreases τ_r . Knowing that τ on each contact element remains constant during the injection process, shear stress drop is mainly controlled by the reduced τ_r , as shown by

$$\Delta\tau = \tau - \tau_r \quad (5.10)$$

where $\Delta\tau$ is the shear stress drop. This means the reduction in τ_i activates the fault while degrading the residual strength governs the shear stress drop. The stress drop determines the area below the GRC as shown in Figure 5.5 and therefore controls the radiated seismic energy magnitude. Note that from an energy perspective, the capacity of rock for storing initial and residual strain energy reduces with decreasing τ_i and τ_r , respectively. The reduction in the initial energy storage capacity leads to rupture initiation. The reduction in the residual energy storage capacity dictates the magnitude of the radiated seismic energy because higher $\Delta\tau$ provides a larger gap between GRCs and post-peak curves. This section studies how relationships between the pressure buildup and stress drop play a role in triggering a rupture and radiating seismic energy. We discuss different pressure buildup patterns for which we need to make assumptions that are, to some extent, consistent with field observations.

Injection field observations show that fluid differential pressures in an injection borehole can be as high as several hundreds of megapascal while the pressure buildup in the fault zone in a close proximity to the well can be as low as several megapascals (Zoback and Harjes, 1997). Instead of modeling fluid pressure inside the injection borehole, we simulate fluid pressure experienced by the fault through applying incremental, uniform pressure loading (blue arrows in Figure 5.2) on both plates of the fault. A target fluid pressure of 15 MPa is defined for pressurizing well-oriented and misoriented faults.

We simulate three pressure increment patterns, each of which reaches the target fluid pressure within the fault through various increments: increasing the fluid pressure by three MPa per increment (5 increments), one MPa per increment (15 increments), and 0.10 MPa per increment (150 increments). For each pattern, the time step is adjusted to accommodate the pressure increments. The model configuration is the same as Figure 5.2 and fault properties follow the frictional behavior in Figure 5.3. Pressurization is performed over a 200 m long domain, centered in the middle of the fault as shown in Figure 5.2. After pressurizing the fault at each increment, the model is allowed to reach equilibrium so once the rupture is triggered, the model is stepped with dynamic scheme until the rupture is terminated. Then, the following pressure increment is applied to the fault plate. The next section simulates the three increment patterns for both well-oriented and misoriented faults.

5.4.1 Well-oriented Faults

For simulating well-oriented faults, fault planes are initially loaded to an average shear stress of 48.25 MPa, just below the average initial shear strength of 48.30 MPa shown in Figure 5.5. That is, we load the fault just below its initial shear strength so a critical pressure of 0.10 MPa is enough to sufficiently reduce the effective stress and trigger a rupture. During the pressurization process, the shear stress and slip on each element are averaged along the final rupture length. The curves in Figure 5.6 represent the average shear stress versus slip for 150-increment, 15-increment, and 5-increment patterns.

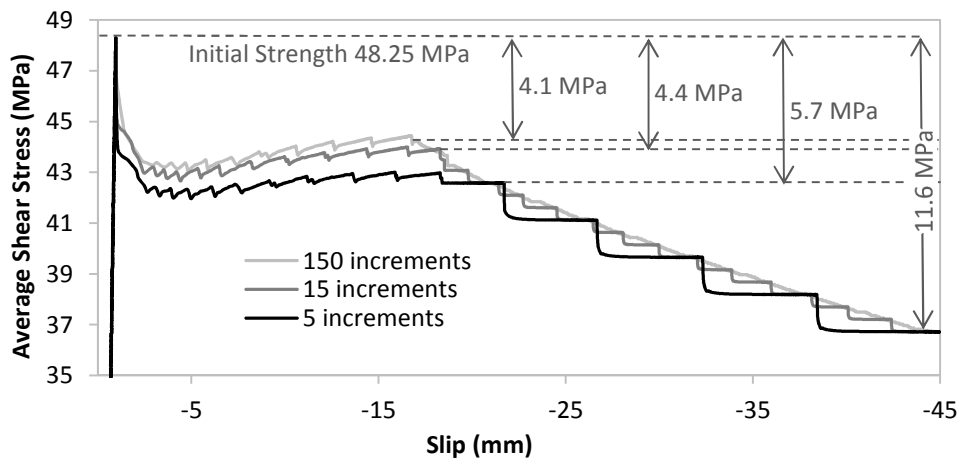


Figure 5.6 Average shear stress and slip along the well-oriented fault during the pressurization process.

For each pattern, after the initial rupture is arrested, remaining increments further reduce the effective stress and thus support secondary ruptures. For example, the stair-step drops of the stress in the

5-increment pattern in Figure 5.6 show that the first increment activates the fault and then the four next increments further rupture additional parts of the fault. The drops are less obvious for the 150-increment pattern as they occur in a more gradual manner.

The final stress drop is 11.6 MPa for all patterns because the target fluid pressure and thus the level of effective stress remain the same at the end of all patterns. However, Figure 5.6 suggests that stress drops for initial ruptures vary between pressure increment patterns. The 5-increment pattern triggers the highest initial stress drop of 5.70 MPa while the 15- and 150-increment cases cause lower initial drops of 4.40 and 4.10 MPa, respectively. The slight difference between the stress drop in Figure 5.5 and the initial rupture curve for the 150-increment case in Figure 5.6 suggests that a pressure increment as low as 0.10 MPa is enough to reduce the initial strength from 48.30 to 48.25 MPa and trigger the rupture. However, the first increment in the 15-increment pattern provides one MPa fluid pressure that reduces both average initial and residual strengths by 0.3 MPa. The three MPa fluid pressure introduced by the first increment in the 5-increment pattern results in the highest drop of 1.60 MPa in its average initial and residual strengths. The fault is already loaded to 48.25 MPa so the average stress drops, which are the difference between the average shear stress of 48.25 MPa and residual strengths, increase from 4.10 MPa to 4.40 and from 4.10 MPa to 5.70 for the 15- and 5-increment patterns, respectively.

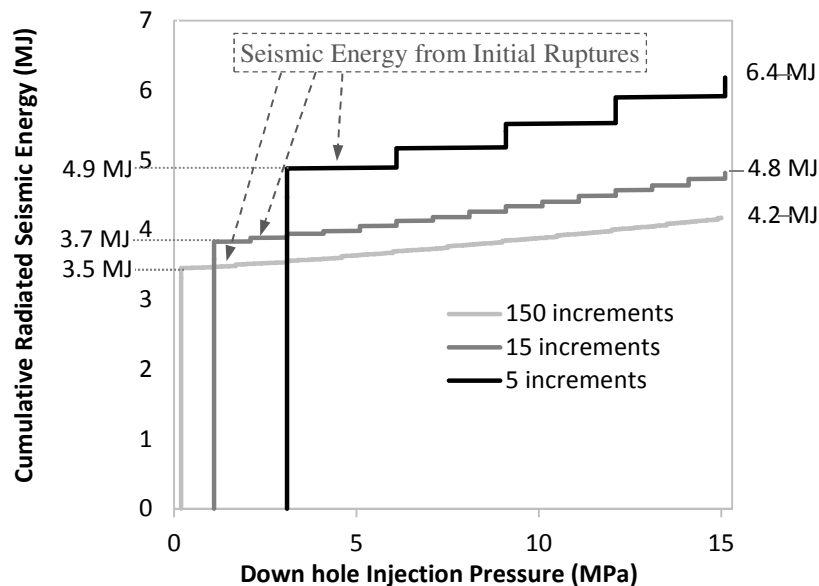


Figure 5.7 Effects of pressure increments on the magnitude of the seismic energy radiated by the well-oriented fault activation.

Figure 5.7 shows the role of different increment patterns in the magnitude of seismic energy radiated from the activation process. The magnitude of the radiated seismic energy inversely correlates

with the number of increments such that radiated seismic energy increases by 50% from 4.20 to 6.40 MJ with increasing the pressure from 0.10 to three MPa per increment. As shown in Figure 5.7, the main source of radiated seismic energy is the initial rupture, which is controlled by the pressure increment value and stress drop. The initial rupture in 150-, 15-, and 5-increment cases generate 4.90, 3.70 and 3.50 MJ radiated seismic energy magnitude, suggesting that gradually increasing the pressure at the onset of rupture suppresses the radiated seismic energy by about 30% from 4.90 to 3.50 MJ.

After the initial rupture, the continuing pressure increment stimulates secondary ruptures featured by a sharp stress drop, developed by the sudden loss of confinement. As can be found in Figure 5.7, the largest secondary ruptures occur in the 5-increment pattern, each radiating 0.30 MJ seismic energy that is only 6% of the energy radiated from the initial rupture. This shows that secondary ruptures make a less significant contribution to the intensity of the simulated injection-induced rupture.

5.4.2 Misoriented Faults

Misoriented faults can be modeled by decreasing average shear stresses acting on the fault before pressurization. In this section, a misoriented fault is modeled by reducing pre-pressurization shear stresses by 10%, from 48.30 to 43.60 MPa. Since the fault is not critically loaded for slip, rupture initiates once the pressure within the fault is equal or higher than a 9.10 MPa critical pressure.

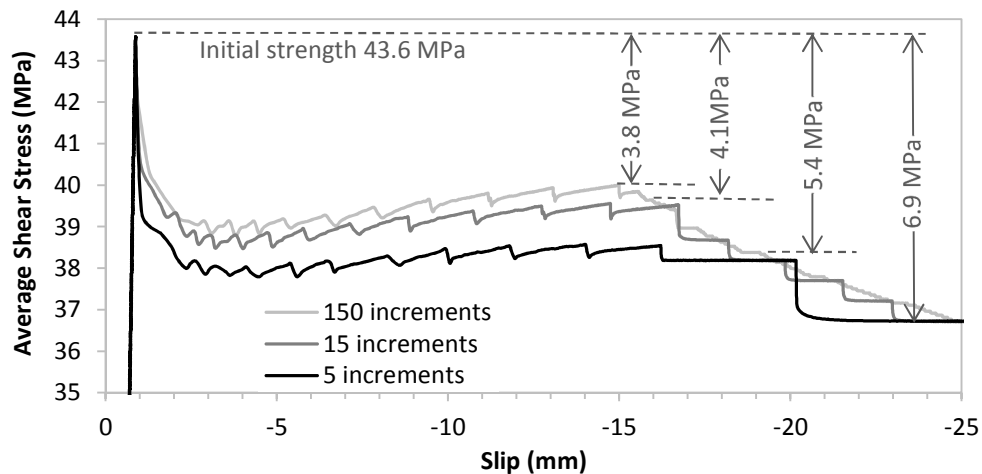


Figure 5.8 Average shear stress and slip along the misoriented fault during the pressurization process.

The average shear stress and slip along the misoriented fault are recorded and shown in Figure 5.8 for 150-, 15-, and 5-increment patterns. The fault is activated after 91, 10, and 4 pressure increments in the 150-, 15-, and 5-increment patterns, respectively. Since the target pressure of 15 MPa is the same,

the ultimate stress drop in all patterns is 6.90 MPa but the stress drop in initial ruptures differs between the patterns. In the 150-increment case, the initial rupture occurs when the fluid pressure is reached 9.10 MPa, providing enough reduction in the effective stress to induce the rupture with the minimal initial stress drop of 3.8 MPa. For the 15-increment case, the next increment after meeting nine MPa pressure totals ten MPa of the fluid pressure, 0.90 MPa more than the critical pressure. Thus, as shown in Figure 5.8, the initial rupture occurs when the residual strength is decreased by 0.30 MPa, leading to a stress drop of 4.1 MPa. For the 5-increment pattern, the pressure has to reach 12 MPa for exceeding the 9.10 MPa critical pressure and triggering the initial rupture. Therefore, the residual strength reduces by 1.60 MPa as rupture propagates, leading to the highest 5.40 MPa initial stress drop. After initial ruptures, secondary ruptures are driven by the continuing reduction in the effective stress until the target pressure of 15 MPa is reached.

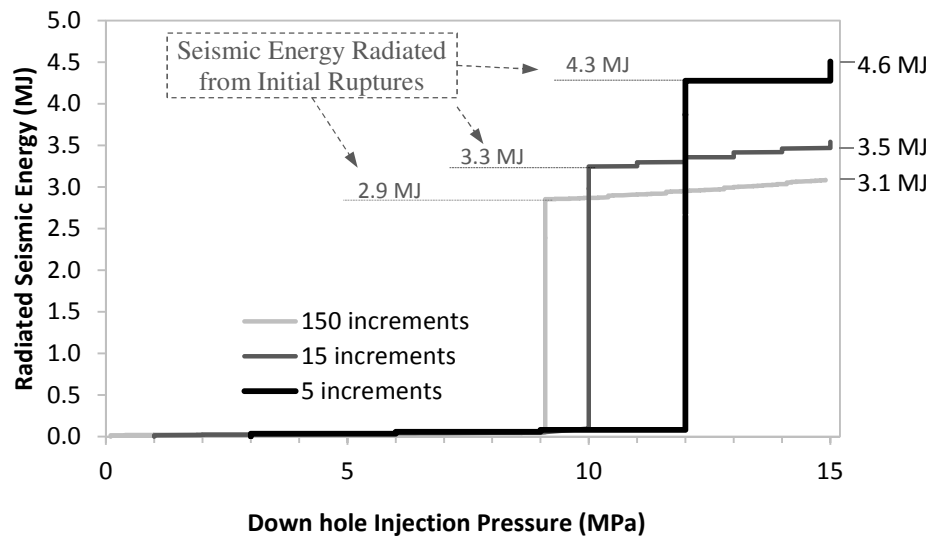


Figure 5.9 Effects of pressure increments on the magnitude of the seismic energy radiated by the activation of the misoriented fault.

Figure 5.9 shows the magnitude of the seismic energy radiated from the activation process through the three increment patterns. The pressure increment value does not affect the radiated seismic energy until the fluid pressure exceeds the critical 9.10 MPa pressure and rupture initiates. Once initiated, the rupture is affected by the pressure increment value such that radiated seismic energy increases by 50% from 3.10 to 4.60 MJ with increasing the pressure increment value from 0.10 to three MPa. As shown in Figure 5.9, the highest magnitude event is generated by the 5-increment pattern that also causes the highest stress drop during the initial rupture in Figure 5.7. Predictably, secondary ruptures in all patterns

construct repeated smaller events, showing that after initial ruptures, the pressure increment plays a less significant role in the overall intensity of seismic events.

5.5 Seismic Moment and Radiated Seismic Energy

The seismic moment is commonly used as a measure of rupture intensity in seismic hazard studies. In this work, we directly obtain the seismic energy radiated from a rupture by the developed methodology and modeling approach. Once directly calculated, the radiated seismic energy can be compared to the seismic moment, rather than being dependent on it. Knowing that the seismic moment is a function of rupture length and average slip, this section explores impacts of increment patterns and fault orientations on the slip distribution and rupture length along the activated faults in section 5.4. Figure 5.10 compares the slip distribution over the 200 m long pressurization domain of the well-oriented and misoriented faults. For comparison, Figure 5.10 also includes the slip distribution along the fault activated by the gradual increase of the local shear stress (Figure 5.4b).

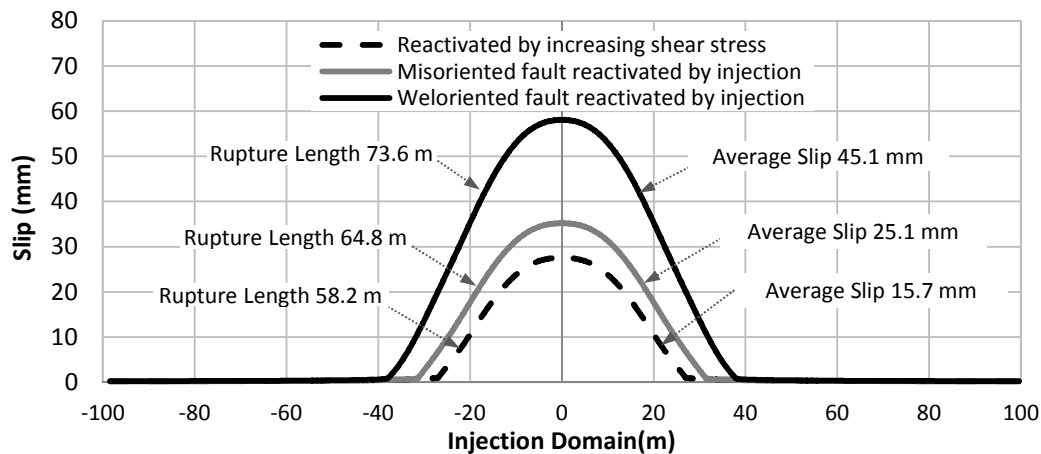


Figure 5.10 Slip distribution along the pressurization domain.

The curves for different pressure increment patterns coincide such that solid black and gray curves represent slip distributions for all increment patterns along the well-oriented and misoriented faults, respectively. The coincidence of the curves of different patterns implies that the target pressure and fault orientation control the slip distribution and thus rupture length. The constant values of the rupture length and average slip between different patterns suggest that the resulting seismic moment stays constant while the radiated seismic energy varies relatively significantly with increment patterns. This is confirmed by the illustration of seismic moment and radiated seismic energy in Figure 5.11.

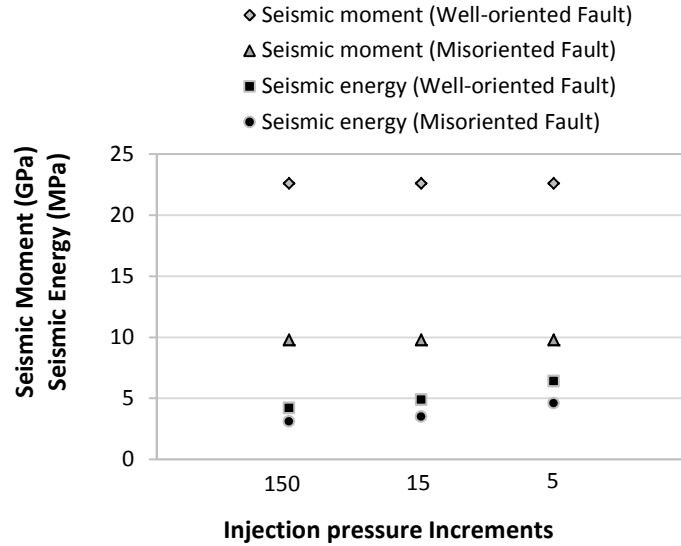


Figure 5.11 Changes in radiated seismic energy and moment with pressure increment patterns and fault orientations.

Regardless of injection pattern, seismic moments of ruptures along the well-oriented and misoriented faults equal 23 and 10 GPa, respectively. However, radiated seismic energy increases by 50% in both fault orientations when increasing the pressure increment from 0.10 MPa to three MPa. This means when the rupture initiation mechanism is the fault unloading by injection pressure, the seismic moment may not represent the intensity of a seismic event.

5.6 Discussion

Defining conditions leading to a seismic event is a challenge for induced-earthquake hazard studies. We show that numerically studying the energetics of a rupture can be a promising framework for studying elements contributing to the intensity of injection-induced seismic events. The methodology shows that misoriented faults may be capable of sliding in a violent manner and radiating significant magnitudes of seismic energy although rupture along a well-oriented fault can generate 30 to 40% more radiated seismic energy, depending on injection patterns. This is because the stress drop and initial shear stress dictate the magnitude of energy available for rupture ($W + \Delta U$) and thus the magnitude of the radiated seismic energy. There is a 7% difference between stress drops of the well-oriented and misoriented faults in different injection patterns. The level of shear stress to which the well-oriented fault is loaded exceeds that of the misoriented fault by 10%. For these reasons, the 30-40% discrepancy is observed between the seismic energy radiated from ruptures in well-oriented and misoriented faults.

Studying patterns of pressure increment within well-oriented and misoriented faults show that the pressure increment value that triggers a local rupture plays a significant role in the magnitude of an injection-induced event. Unless the fault initial strength is in the proximity of the local shear stress on the fault, fluid can be injected under a high-pressure increment. Secondary ruptures generate relatively lower-magnitude events, depending on the pressure increment value, such that the highest magnitude event by a secondary rupture generates radiated seismic energy that is 6% of the energy radiated by the respective initial rupture. That is, pressure increment can be once again high after the initial rupture arrest yet there is no significant impact on the overall radiated seismic energy.

As mentioned before, the seismic moment is commonly used as a measure of rupture intensity. We calculated the seismic energy and moment for different patterns of pressure within well-oriented and misoriented faults. While radiated seismic energy increases by 50% with increasing the pressure increment from 0.10 to three MPa, seismic moments stay constant in both fault orientations. This is mainly because the seismic moment does not account for the initial stress drop while in injection-induced seismicity increment patterns govern initial stress drop and therefore influence the radiated seismic energy. Therefore, seismic moments may not be an effective representative of seismic events triggered by fluid injection.

One of the main improvements that can be made to the modeling approach in this chapter is the inclusion of leakoff in the fluid injection process. Excluding leakoff effects, we directly related the fluid injection rate to the linearly incremental pressure within the fault planes. However, the loss of fluid to the formation adjacent to the fracture controls the pressure within the fault plates (Howard and Fast, 1957; Nolte, 1979; Mayerhofer et al., 1993). Craig et al. (2000) and Liu and Ehlig-Economides (2015) showed that depending on leakoff behaviors, formation pressure can significantly vary with the bottomhole pressure, resulting in an additional component of the poroelastic stress perturbation within the affected zone. Moreover, seismic response of material surrounding a fault should be considered because it can affect potential damages due to the induced rupture (Ghayoomi et al., 2017; Khosravi et al., 2016; Mirshekari and Ghayoomi, 2017a, 2017b).

Another limitation of this study is associated with the assumption of the constant rock temperature during the injection as Blanpied et al. (1995) and McClure and Horne (2014) showed that rock formation temperature change has a role in triggering seismicity. In this work, we develop the methodology by making simplifying assumptions. This reduces the complexity of instability concepts, allows intuitive interpretation of results, and helps better understand the injection role in triggering a rupture. Future studies are required for simulating fully coupled hydro-Thermo-mechanical models

accounting for the transient fluid flow, formation leakoff behaviors and interactions with the rock temperature. Finally, we use UDEC for the method development and calibration but the developed framework can be implemented into any numerical modeling tool capable of simulating discontinuous displacements along a plane of weakness.

5.7 Conclusions

The focus of this chapter is to extend the developed framework to study injection-induced seismicity. We also provide some examples of ruptures induced by different injection scenarios. We show that monitoring injection pressure may be a way to control the magnitude of induced events during operations in deep wastewater disposal and geothermal reservoirs. Making simplifying assumptions, we suggest that the injection pressure can be as high as three MPa per increment before and after the initial rupture with no significant impacts on the magnitude of radiated seismic energy. However, the low-pressure increment of 0.10 MPa per increment in the proximity of rupture initiation can suppress the radiated seismic energy by about 30%. Results also show that misoriented faults may not be necessarily bound to aseismic slips. Ruptures can occur along a misoriented fault once the conditions for instability emerge. The comparison between seismic moments and radiated seismic energy shows that while seismic energy represents effects of the pressure increment on the rupture intensity, seismic moments stay constant. This suggests that seismic moment may not be an effective measure for studying intensity of seismic events triggered by fluid injection. The developed methodology is shown to be a useful framework for studying induced seismic potentials in an area and exploring strategies for minimizing the intensity of these events.

5.8 References

- Baisch, S., Os, R., Rothert, E., Stang, H., Jung, R., Schellschmidt, U., 2010. A numerical model for fluid injection induced seismicity at Soultz-sous-Forêts. *Int. J. Rock Mech. Min. Sci.* 47. <https://doi.org/10.1016/j.ijrmms.2009.10.001>
- Barton, C.A., Zoback, M.D., Moos, D., 1995. Fluid flow along potentially active faults in crystalline rock. *Geology* 23, 683–686. [https://doi.org/10.1130/0091-7613\(1995\)023<0683:FFAPAF>2.3.CO](https://doi.org/10.1130/0091-7613(1995)023<0683:FFAPAF>2.3.CO)
- BC Oil and Gas Commission, 2012. Investigation of observed seismicity in the Horn River Basin -August 2012.
- Beeler, N.M., 2001. Stress drop with constant, scale independent seismic efficiency and overshoot. *Geophys. Res. Lett.* 28, 3353–3356. <https://doi.org/10.1029/2001GL012906>
- Beroza, G.C., Mikumo, T., 1996. Short slip duration in dynamic rupture in the presence of heterogeneous fault properties. *J. Geophys. Res. Solid Earth* 101, 22449–22460. <https://doi.org/10.1029/96JB02291>
- Blanpied, M.L., Lockner, D.A., Byerlee, J.D., 1995. Frictional slip of granite at hydrothermal conditions. *J. Geophys. Res. Solid Earth* 100, 13045–13064. <https://doi.org/10.1029/95JB00862>

- Board, M., 1996. Numerical examination of mining-induced seismicity, in: ISRM International Symposium - EUROCK 96. International Society for Rock Mechanics and Rock Engineering, Turin, Italy, pp. 1469–86.
- Bourouis, S., Bernard, P., 2007. Evidence for coupled seismic and aseismic fault slip during water injection in the geothermal site of Soultz (France), and implications for seismogenic transients. *Geophys. J. Int.* 169, 723–732. <https://doi.org/10.1111/j.1365-246X.2006.03325.x>
- Brune, J.N., 1970. Tectonic stress and the spectra of seismic shear waves from earthquakes. *J. Geophys. Res.* 75, 4997–5009. <https://doi.org/10.1029/JB075i026p04997>
- Cladouhos, T., Petty, S., Foulger, G., Julian, B., Fehler, M., 2010. Injection induced seismicity and geothermal energy. *GRC Trans.* 34.
- Cook, N.G.W., 1966. The design of underground excavations, in: Eighth Symposium on Rock Mechanics, University of Minnesota, in Failure and Breakage of Rock. pp. 167–193.
- Cook, N.G.W., 1965. A note on rockbursts considered as a problem of stability. *J. South African Inst. Min. Metall.* 65, 437–446.
- Cornet, F.H., Helm, J., Poitrenaud, H., Etchecopar, A., 1997. Seismic and aseismic slips induced by large-scale fluid injections. *Pure appl. Geophys* 150, 563–583.
- Craig, D.P., Odegard, C.E., Pearson, W.C., Schroeder, J.E., 2000. Case History: Observations from diagnostic injection tests in multiple pay sands of the Mamm Creek Field, Piceance Basin, Colorado, in: SPE Rocky Mountain Regional/Low-Permeability Reservoirs Symposium and Exhibition. Society of Petroleum Engineers. <https://doi.org/10.2118/60321-MS>
- Dieterich, J.H., 1979. Modeling of rock friction: 1. Experimental results and constitutive equations. *J. Geophys. Res.* 84, 2161. <https://doi.org/10.1029/JB084iB05p02161>
- Dieterich, J.H., Kilgore, B., 1996. Implications of fault constitutive properties for earthquake prediction. *Proc. Natl. Acad. Sci. U. S. A.* 93, 3787–94.
- Duvall, W.I., Stephenson, D.E., 1965. Seismic energy available from rockbursts and underground explosions. *Trans. Soc. Min. Eng.* 232, 235–240.
- EarthquakeTrack, 2017. Recent earthquakes near Oklahoma, United States [WWW Document]. URL <http://earthquakeTrack.com/p/united-states/oklahoma/recent>
- Ellsworth, W.L., 2013. Injection-induced earthquakes. *Science* (80-.). 341.
- Frohlich, C., Hayward, C., Stump, B., Potter, E., 2008. The Dallas-Fort Worth earthquake sequence: October 2008 through May 2009. *Bull. Seismol. Soc. Am.* 101, 327–340. <https://doi.org/10.1785/0120100131>
- Fukuyama, E., 2009. Introduction: Fault-zone properties and earthquake rupture dynamics, 1st ed, International Geophysics. Elsevier Inc. [https://doi.org/10.1016/S0074-6142\(08\)00001-6](https://doi.org/10.1016/S0074-6142(08)00001-6)
- Ghayoomi, M., Suprunenko, G., Mirshekari, M., 2017. Cyclic Triaxial Test to Measure Strain-Dependent Shear Modulus of Unsaturated Sand. *Int. J. Geomech.* 17, 4017043. [https://doi.org/10.1061/\(ASCE\)GM.1943-5622.0000917](https://doi.org/10.1061/(ASCE)GM.1943-5622.0000917)
- Guglielmi, Y., Cappa, F., Avouac, J.-P., Henry, P., Elsworth, D., 2017. Seismicity triggered by fluid injection–induced aseismic slip.
- Howard, G.C., Fast, C.R., 1957. Optimum fluid characteristics for fracture extension, in: American Petroleum Institute.
- Itasca, 2016. Background - The 2D Distinct Element Method, UDEC Manual.

- Karner, S.L., Marone, C., 2000. Effects of loading rate and normal stress on stress drop and stick-slip recurrence interval. *American Geophysical Union*, pp. 187–198.
<https://doi.org/10.1029/GM120p0187>
- Keranen, K.M., Savage, H.M., Abers, G.A., Cochran, E.S., 2013. Potentially induced earthquakes in Oklahoma, USA: Links between wastewater injection and the 2011 Mw 5.7 earthquake sequence. *Geology* 41, 699–702. <https://doi.org/10.1130/G34045.1>
- Khademian, Z., Nakagawa, M., Garvey, R., Ozbay, U., 2017. Role of fluid injection pressure in inducing seismicity, in: *Proceedings of the 42nd Workshop on Geothermal Reservoir Engineering*. p. 10.
- Khademian, Z., Nakagawa, M., Ozbay, U., 2018. Modeling earthquake rupture propagation based on calculations of energy components. *Manuscr. Submitt. Publ.*
- Khademian, Z., Ozbay, U., 2018. A numerical modeling methodology for assessing rock failure stabilities, in: *Third International Conference on Rock Dynamics & Applications*. Trondheim, Norway.
- Khademian, Z., Poeck, E., Garvey, R., Ozbay, U., 2016. Studies of seismicity generated by unstable failures around circular excavations, in: *50th U.S. Rock Mechanics/Geomechanics Symposium*. American Rock Mechanics Association, Houston, Texas.
- Khosravi, A., Gheibi, A., Rahimi, M., McCartney, J.S., Haeri, S.M., 2016. Impact of void ratio and state parameters on the small strain shear modulus of unsaturated soils. *Japanese Geotech. Soc. Spec. Publ.* 2, 241–246. <https://doi.org/10.3208/jgssp.IRN-03>
- Liu, G., Ehlig-Economides, C., 2015. Comprehensive global model for before-closure analysis of an injection falloff fracture calibration test, in: *SPE Annual Technical Conference and Exhibition*. Society of Petroleum Engineers. <https://doi.org/10.2118/174906-MS>
- Lockner, D.A., Beeler, N.M., 1999. Premonitory slip and tidal triggering of earthquakes. *J. Geophys. Res. Solid Earth* 104, 20133–20151. <https://doi.org/10.1029/1999JB900205>
- Madariaga, R., Olsen, K., Archuleta, R., 1998. Modeling dynamic rupture in a 3D earthquake fault model. *Bull. Seismol. Soc. Am.* 88, 1182–1197.
- Majer, E.L., Baria, R., Stark, M., Oates, S., Bommer, J., Smith, B., Asanuma, H., 2007. Induced seismicity associated with Enhanced Geothermal Systems. *Geothermics* 36, 185–222.
<https://doi.org/10.1016/J.GEOTHERMICS.2007.03.003>
- Mayerhofer, M.J., Economides, M.J., Leoben, M.U., 1993. Permeability estimation from fracture calibration treatments. *West. Reg. Meet.* 26–28.
- McClure, M.W., Horne, R.N., 2014. Correlations between formation properties and induced seismicity during high pressure injection into granitic rock. *Eng. Geol.* 175, 74–80.
<https://doi.org/10.1016/J.ENGGEOL.2014.03.015>
- McClure, M.W., Horne, R.N., 2011. Investigation of injection-induced seismicity using a coupled fluid flow and rate/state friction model, in: *Thirty-Sixth Workshop on Geothermal Reservoir Engineering* Stanford University. Stanford.
- McGarr, A., 2014. Maximum magnitude earthquakes induced by fluid injection. *J. Geophys. Res. Solid Earth* 119, 1008–1019. <https://doi.org/10.1002/2013JB010597>
- Mirshekari, M., Ghayoomi, M., 2017a. Centrifuge tests to assess seismic site response of partially saturated sand layers. *Soil Dyn. Earthq. Eng.* 94, 254–265.
<https://doi.org/10.1016/J.SOILDYN.2017.01.024>
- Mirshekari, M., Ghayoomi, M., 2017b. Simulating Seismic Response of Unsaturated Sand Layers inside a

Geotechnical Centrifuge. Proc. 19th ISSMGE Conf. 1–6.

- Nolte, K.G., 1979. Determination of fracture parameters from fracturing pressure decline, in: SPE Annual Technical Conference and Exhibition. Society of Petroleum Engineers.
<https://doi.org/10.2118/8341-MS>
- Poeck, E., Khademian, Z., Garvey, R., Ozbay, U., 2016. Modeling unstable rock failures in underground excavations, in: 2016 ISRM International Symposium, 2016 (Ed.), Rock Mechanics and Rock Engineering: From the Past to the Future. CRC Press, Ürgüp-Nevşehir, Turkey, pp. 505–509.
<https://doi.org/10.1201/9781315388502-86>
- Prieto, G.A., Florez, M., Barrett, S.A., Lopez, G.A., Beroza, G.C., 2012. Earthquake source scaling, stress drops and seismic efficiency of intermediate-depth earthquakes. *Geophys. Res. Abstr. EGU Gen. Assem.* 14, 2012–5287.
- Rice, J.R., 1983. Constitutive relations for fault slip and earthquake instabilities. *Pure Appl. Geophys.* 121, 443–475. <https://doi.org/10.1007/BF02590151>
- Richards, H.G., Parker, R.H., Green, A.S.P., Jones, R.H., Nicholls, J.D.M., Nicol, D.A.C., Randall, M.M., Richards, S., Stewart, R.C., Willis-Richards, J., 1994. The performance and characteristics of the experimental hot dry rock geothermal reservoir at Rosemanowes, Cornwall (1985–1988). *Geothermics* 23, 73–109. [https://doi.org/10.1016/0375-6505\(94\)90032-9](https://doi.org/10.1016/0375-6505(94)90032-9)
- Rutqvist, J., Rinaldi, A.P., Cappa, F., Moridis, G.J., 2013. Modeling of fault reactivation and induced seismicity during hydraulic fracturing of shale-gas reservoirs. *J. Pet. Sci. Eng.* 107, 31–44.
<https://doi.org/10.1016/j.petrol.2013.04.023>
- Ryder, J. a., 1988. Excess shear stress in the assessment of geologically hazardous situations. *J. South African Inst. Min. Metall.* 88, 27–39.
- Salamon, M.D.G., 1984. Energy considerations in rock mechanics: fundamental results 84, 233–246.
- Salamon, M.D.G., 1974. Rock mechanics of underground excavations. *Advances in Rock Mechanics*, in: 3rd Cong Int Soc Rock Mech. pp. 951–1099.
- Salamon, M.D.G., 1970. Stability, instability and design of pillar workings. *Int. J. Rock Mech. Min. Sci.* 7, 613–631. [https://doi.org/10.1016/0148-9062\(70\)90022-7](https://doi.org/10.1016/0148-9062(70)90022-7)
- Shapiro, S.A., Dinske, C., Kummerow, J., 2007. Probability of a given-magnitude earthquake induced by a fluid injection. *Geophys. Res. Lett.* 34, L22314. <https://doi.org/10.1029/2007GL031615>
- U.S. Department of Energy, 2017. Induced seismicity [WWW Document]. URL http://esd1.lbl.gov/research/projects/induced_seismicity/
- Wong, T.-F., 2013. On the normal stress dependence of the shear fracture energy. *American Geophysical Union*, pp. 1–11. <https://doi.org/10.1029/GM037p0001>
- Zhang, Y., Person, M., Rupp, J., Ellett, K., Celia, M.A., Gable, C.W., Bowen, B., Evans, J., Bandilla, K., Mozley, P., Dewers, T., Elliot, T., 2013. Hydrogeologic controls on induced seismicity in crystalline basement rocks due to fluid injection into Basal reservoirs. *Groundwater* 51, 525–538.
- Zoback, M.D., Harjes, H.-P., 1997. Injection-induced earthquakes and crustal stress at 9 km depth at the KTB deep drilling site, Germany. *J. Geophys. Res. Solid Earth* 102, 18477–18491.
<https://doi.org/10.1029/96JB02814>
- Zoback, M.D., Kohli, A., Das, I., McClure, M., 2012. The importance of slow slip on faults during hydraulic fracturing stimulation of shale gas reservoirs. *Am. Unconv. Resour. Conf.* 5–7.

CHAPTER 6

GENERAL CONCLUSION

6.1 Research Originality

Earthquake occurs as a result of a sudden release of large amount of energy stored underground. The actual earthquake damage depends on the nature of the medium where the suddenly released energy is transmitted. Seismologists have largely approached earthquakes as a subject of complex natural factors. However, the recent tremors in the mid-US, a region featured by low levels of natural seismic activity, attracted attention on the possibility of triggering earthquakes by human activities.

Unlike the recent earthquakes in the mid-US, man-made tremors are not a new phenomenon in mining activities where unstable rock failure is observed and is shown to create an earthquake-like seismic event. Since the 1940s, attempts have been made in mining engineering to understand the mechanisms of these failures by viewing them as a problem of instability. Although the mechanisms of natural earthquakes and mining-induced seismicity are similar in many aspects, fields of earthquake seismology and mining engineering have rarely intersected because of the difference in perspectives. The intersection laid out in this dissertation is the key to better understanding natural earthquakes and controlling the power humans have of disturbing the seismic environment in different rock engineering activities.

The main original contribution of this dissertation lies in translating the failure instability concept, mostly developed in mining engineering, into a computational framework for studying the occurrence and intensity of natural and induced seismicity. Computational methods provide useful means for exploring large-scale phenomena like induced seismicity that cannot be exposed by laboratory experiments. This framework presents ways to study how the stored energy is released and helps quantify correlations of the surrounding rock mechanical properties, the activated fault frictional properties, and *in-situ* stress patterns with earthquake source parameters and intensity. This computational framework can help open a new field in earthquake studies for geoengineering this previously called natural phenomenon.

The developed computational framework includes methodologies and modeling approaches for identifying a seismic event and assessing their intensity. The instability concept is used for identifying a seismic event and techniques are provided for explicitly calculating the radiated seismic energy, the component that is mainly responsible for the event intensity. Seismic moment is a commonly used estimate of the earthquake intensity but this dissertation shows that seismic moment is not necessarily

correlated with the intensity of events. Possible applications of the framework in studying natural earthquakes and seismicity induced by mining, tunneling, deep wastewater disposal, and geothermal activities are included and results are checked against available analytical solutions and field data. This study shows how the developed framework can help assess and then minimize seismic hazard potentials in different rock engineering activities.

6.2 Summary of Accomplishments

A computational modeling framework is developed to study the relationship between unstable failure and seismicity. Under this framework, the following specific cases are investigated: unstable failure induced by tunneling, shaft-boring, and mining activities; rupture on a strike-slip fault activated by tectonic moments; and injection-induced rupture on a strike-slip fault.

For induced seismicity in tunneling and shaft-boring activities, this dissertation shows that unstable failure occurs due to complex combinations of components, mainly including the rock brittleness, *in-situ* stresses, loading system stiffness, rock compressive strength, frictional properties of fault zones, failure zone extent, and excavation geometry. Cases are discussed where empirical criteria partially using these components could result in unrealistic estimates of magnitudes of seismic events. For instance, brittle rock failure around an excavation in relatively highly stressed regions may not necessarily result in an unstable failure if the loading system is stiff enough. Also, high *in-situ* stresses may not be also necessary for triggering an unstable slip on neighboring faults if the stiffness of the loading system is low enough. Variations of geologic settings add to the complexity of identifying an unstable failure and assessing magnitudes of resulting seismic events based on the influential elements. This study shows that estimating the radiated seismic energy can be a promising way of studying seismic events because a significant radiation of seismic energy remains a common signature for the expression of unstable failures and magnitudes of induced seismic events. Once reliably estimated during the exploration stage of an underground facility project, the expected magnitudes of induced events can help adopt cost-effective and safe measures for mitigating possible damages during the operation phase.

For the mining-induced seismic events, the challenge is to design mining layouts that minimize the magnitudes of possible induced seismic events. Support systems need to be also designed based on the estimates of magnitudes of possible seismic events induced by the mining operation. The developed computational framework can be used to address these challenges by assessing potentials for occurrence and magnitudes of the induced events. Mining-induced unstable failures due to loading in compression are discussed by modeling a tabular opening supported by a single pillar. Dynamic calculations of seismic energy radiated from these models are shown to be within 3% error of values from static energy

component calculations. An idealized fault is then modeled and activated for exploring unstable slip triggered by mining activities. Computational results of the fault rupture length, slip magnitude, and radiated seismic energy are found within 6% of the analytic solution. Given the verification examples provided, the shear- and compressive-type seismic event potentials in various mining layouts within complex fracture networks can be assessed through the proposed computational framework. Support systems can then be designed based on the estimates of magnitudes of possible seismic events.

For extending the framework to studying injection-induced seismicity, this dissertation first explores the mechanics of rupture induced by tectonic forces and verifies results of energy calculations and rupture characteristics by checking them against existing analytical solutions, globally recorded earthquake seismic data, and other rupture simulators. The advantage of the developed framework over the common rupture simulators is its capability to avoid prescribing rupture length and rupture initiation areas. This allows studying variations of the earthquake intensity with rupture lengths, slip distribution, and seismic moments in detail. The introduced modeling approach for simulating an earthquake rupture allows studying stick-slip mechanisms and their implications for seismic energy radiation. The rupture model is calibrated in terms of loading conditions, mesh size, and damping constant. The rupture energetics and characteristics in the calibrated model are shown to be within 1 to 5% error of available analytic solutions. The calibrated model is then used for simulating injection-induced rupture.

Regarding injection-induced seismicity, the common computational tools rely on the seismic moment as a representative measure for the seismic potentials in a modeled injection site. This dissertation shows the ineffectiveness of the seismic moment as a measure to suggest strategies for minimizing magnitudes of seismic events. As one of the framework applications, it is shown that monitoring injection pressure is a promising way to control the magnitude of induced events during operations in deep wastewater disposal and geothermal reservoirs.

6.3 Future Research

This dissertation established a useful framework for studying induced seismic potentials and exploring strategies for minimizing magnitudes of these events; however, simplifying assumptions were made for calibration and verification purposes. The following improvements are suggested for future research following this dissertation.

Unless mechanics of a phenomenon in two-dimensional analyses is interpreted, the three-dimensional analyses may not be of great use. This work used plane strain analyses for two-dimensional modeling of induced events, assuming the third direction has an infinite length. Three-dimensional

analyses can follow this work and provide more applicable results although introducing further complications. In the case of mining pillar failures, effects of stress patterns in the third direction can be explored. For rupture simulation, slip distribution and stick-slip mechanisms in an earthquake rupture plane can be correlated with tempo-spatial patterns of radiated seismic energy. This enables studying effects of fault plane orientation and spatial variability of fault frictional properties on earthquake rupture occurrence and intensity. Similar calibration and verification processes as performed in this dissertation is required for the three-dimensional modeling of unstable failures in compression and shear slip.

This study assumed isotropic and homogenous rock properties for modeling induced seismicity. Random variability of mechanical properties of rocks need to be considered in models so their effects on induced seismic events can be investigated. Frictional properties can also vary along a fault, indicating heterogeneous fault properties. Considering effects of anisotropy and heterogeneity on occurrence and intensity of induced seismic events can lead to a more realistic estimate of seismic hazards in different rock engineering activities. Unstable compressive failure of intact rock and unstable slip on a discontinuity are separately investigated in this study for proving the concept of instability and showing the method application. However, rock mass models comprising both discontinuity sets and intact rock help better understand seismic event mechanisms when they occur.

This dissertation discusses slip on a single fault for providing verification examples. However, one of the advantages of adopting UDEC in this study is the capability of this code in modeling complex fracture networks. Modeling fault systems and investigating the interaction of faults with different geometry, morphology, and properties are of great significance since slip on a fault may either trigger slip on neighboring faults or further stabilize them. The triggering mechanism may be static due to the steady-state alteration of stresses or dynamic due to interaction of seismic waves with nearby faults. Conditions leading to multiple fault activation can be studied by the developed framework for a more reliable estimate of seismic potentials in different rock engineering projects.

Others have performed laboratory experiments exploring rate-, slip-, and state-dependent frictional properties of faults. Scaling these frictional properties to faults on geologic scales remains as a challenge in this field. Friction constitutive laws accounting for rate-, slip-, and state-dependent frictional properties of faults need to be developed for relating laboratory experiments to large scale faults. Cyclic natural and induced seismicity can be also simulated by rate-, slip-, and state- constitutive laws to faults modeled in the developed framework.

This study calculates radiated seismic energy at the source as a measure of earthquake intensity. However, due to natural damping mechanisms of rock formations, the seismic energy that is recorded on the surface may be tremendously attenuated. The damping process mainly depends on depth of earthquake source, types of geological structures, and mechanical properties of rock layers. The developed framework can be equipped with techniques for attenuating radiated seismic energy, leading to improvements to seismic hazard estimates.

In the case of simulating natural earthquake rupture, this study showed that with decreasing shear modulus of rock surrounding a fault the radiated seismic energy increases almost exponentially. An extensive, non-dimensional parametric study can follow this work for quantifying relationships between the rock mechanical properties, fault frictional variations, rupture length, slip distribution, and the intensity of earthquakes.

With respect to injection-induced seismicity, it was assumed that the rock matrix is impermeable and rock temperature is constant. Poroelastic stresses due to normal and abnormal fluid leakoff can significantly disturb the pattern of *in-situ* stresses around the injection area. Effects of the poroelastic stresses on inducing seismicity can be studied by the developed framework. Given that UDEC is not specifically designed for computing pore pressure diffusion, commercially available codes, including TOUGH2 and COMSOL may be coupled with UDEC to perform hydro-mechanical modeling. This study assumed that fluid injection can be simulated by the steady-state pressurizing of the fault plane. The mentioned coupling allows for real-time study of injection process, stress re-distribution, and rupture propagation using unsteady-state mass balance equations.

The increasing demand for deeper underground rock engineering works requires an understanding of rock mass behavior under high temperatures. Rock mechanical properties and fault frictional features can vary with rock temperature. Carefully designed experiments are needed to explore effects of temperature on the elastic modulus, Poisson's ratio, permeability, thermal expansion coefficient, and compressive strength of rock mass. In addition, there is a need to study effects of rock temperature on fault frictional properties, including initial friction, residual friction, characteristic distance, and rate-dependent friction. The developed framework can be used for investigating roles of the temperature dependence in inducing seismicity.

For method development, this study excluded thermal stress components from the calculations but they need to be considered for assessing seismic hazard potentials caused by injecting cold fluid into high-temperature fault zones. Thermal stress may play a significant role in seismicity induced by the

forced fluid circulation in geothermal reservoirs. Thermal stresses may also help understand some of the questions remained as a challenge in the field of seismicity in geothermal reservoirs. It has been reported that the location of large-magnitude seismic events in geothermal reservoirs mostly migrates away from the injection points with time. Altering pore pressure within the reservoir may be a reason behind the continued seismicity but pore pressure elevation is expected to decay as it spreads away from the injection point. Thermally effected zones, however, can grow and affect a larger area even long after the shot-in. The growing temperature alteration may be the underlying cause of migrating seismicity but proving this hypothesis requires accounting for thermal stresses in the developed framework.

APPENDIX A

SUPPLEMENTAL ELECTRONIC FILES FOR CHAPTER 2

This appendix includes database, UDEC fish codes, and spreadsheets for modeling compressive- and shear-type unstable failures in tunneling and shaft-boring configurations.

Data Files for Rock Burst Simulation in Tunneling and Shaft-boring	Files containing UDEC fish codes for constructing verification problems and simulating compressive- and shear-type rock burst during tunneling and shaft-boring operations.
Duall_Stephenson.dat	Folder name: Figure 2.1 The dat file named "Dual-Stephenson" contains codes for modeling the problem that was analytically solved by Duvall & Stephenson (1965). The sav file named "final_duall" refers to the UDEC output of the modeling.
Salamon.dat	Folder name: Figure 2.2 The dat file named "Salamon" contains codes for modeling the problem that was analytically solved by Salamon (1984). The sav file named "final_salamon" refers to the UDEC output of the modeling.
Tabular.dat	Folder name: Figure 2.3 The dat file named "Tabular" contains codes for modeling the problem that was analytically solved by Cook (1966).
Figure 2.4 and 2.5.xlsx	Folder name: Figures 2.4 and 2.5 Data for brittle pillar and semi-brittle pillar failures in Figures 2.4 and 2.5
Energetics of shear test.xlsx	Folder name: Figure 2.7 The spreadsheet named "Energetics of shear test" provides data for Figure 2.7
_input.dat	Folder name: Figures 2.8 and 2.9 This folder contains code for plotting Figures 2.8 and 2.9. The dat file named "_input" needs to be called for Parametric studies on brittle failure of rock surrounding a circular excavation. Young's modulus of surrounding rock is kept constant at 10 GPa but the k ratio changes between simulations. The sav files are named by the assigned properties: Fi= final simulation file pw= Pillar Width MD= External Boundary Diameter ra: Tunnel Radius dist= distance between the tunnel and the fault, if there is a fault B= the indicator of using Boundary Element Boundary. If zero, means BEM is not

	<p>used.</p> <p>K= k ratio</p> <p>ExR= width of each mining slices.</p> <p>E= Young's modulus of the rock surrounding the pillar which is 10 GPa for this simulation</p> <p>P= constitutive law used for simulating pillar failure: 1: Mohr Coulomb; 0 : Elastic; 2: Strain Softening</p> <p>Fric= initial friction angle for the pillar</p>
main-without.dat	<p>Folder name: Figures 2.8 and 2.9</p> <p>This dat file contains codes for running the parametric study in Figures 2.8 and 2.9</p>
Setup.dat	<p>Folder name: Figures 2.8 and 2.9</p> <p>This dat file defines the names for the sav files.</p>
FZone.dat	<p>Folder name: Figures 2.8 and 2.9</p> <p>This dat file gives the number of failed element in a model. This file should be called after restoring the sav files for each case.</p>
_input.dat	<p>Folder name: Figures 2.10 and 2.11</p> <p>This folder contains code for plotting Figures 2.10 and 2.11. The dat file named "_input" needs to be called for Parametric studies on brittle failure of rock surrounding a circular excavation. The k ratio is kept constant at 0.45 but Young's modulus of surrounding rock changes between simulations. The sav files are named by the assigned properties. E in the file names stand for Young's modulus and is different for each file.</p>
main-without.dat	<p>Folder name: Figures 2.10 and 2.11</p> <p>This dat file contains codes for running the parametric study in Figures 2.8 and 2.9</p>
Setup.dat	<p>Folder name: Figures 2.10 and 2.11</p> <p>This dat file defines the names for the sav files.</p>
FZone.dat	<p>Folder name: Figures 2.10 and 2.11</p> <p>This dat file gives the number of failed element in a model. This file should be called after restoring the sav files for each case.</p>
_input.dat	<p>Folder name: Figures 2.13 and 2.14</p> <p>This folder contains code for plotting Figures 2.13 and 2.14. The dat file named "_input" needs to be called for Parametric studies on slip on a fault next to a circular excavation. Young's modulus of surrounding rock is kept constant at 10 GPa but the k ratio changes between simulations. The sav files are named by the assigned properties. The k ratio is different for each file.</p>
main.dat	<p>Folder name: Figures 2.13 and 2.14</p> <p>This dat file contains codes for running the parametric study in Figures 2.8 and 2.9</p>

Setup.dat	Folder name: Figures 2.13 and 2.14 This dat file defines the names for the sav files.
_input.dat	Folder name: Figures 2.15 and 2.16 This folder contains code for plotting Figures 2.15 and 2.16. The dat file named "_input" needs to be called for Parametric studies on slip on a fault next to a circular excavation. The k ratio is kept constant at 0.45 but Young's modulus of surrounding rock changes between simulations. The sav files are named by the assigned properties. E in the file names stand for Young's modulus and is different for each file.
main.dat	Folder name: Figures 2.15 and 2.16 This dat file contains codes for running the parametric study in Figures 2.8 and 2.9
Setup.dat	Folder name: Figures 2.15 and 2.16 This dat file defines the names for the sav files.

APPENDIX B

SUPPLEMENTAL ELECTRONIC FILES FOR CHAPTER 3

This appendix includes the database, UDEC fish codes, and spreadsheets for modeling compressive- and shear-type violent failures.

Data Files for Rock Burst Simulation in Mining	Files containing UDEC fish codes for constructing verification problems and simulating compressive- and shear-type rock burst during mining operations.
Figures 3.2, 3.3, 3.4, and 3.5.xlsx	The spreadsheet summarized the analyses included in Figures 3.2, 3.3, 3.4, and 3.5.
Softening parameters.xlsx	Folder name: Figure 3.2 Softening Parameters used for the Mohr Coulomb Strain Softening Constitutive Law for the single pillar in Figure 3.2
_input.dat	Folder name: Figure 3.4 Each folder provides codes for simulating pillar failure under different loading systems: for example "Rock15GPaP10GPa" contains fish codes for simulating pillar failure while Young's modulus of the pillar is 10 GPa and that of the surrounding rock is 15 GPa. The dat file named "_input.dat" needs to be called for starting the simulation.
Results.dat	Folder name: Figure 3.4 "Results.dat" file should be called after solving the model or restoring the sav file. This dat file provides stress-convergence curves.
Energy_verification; Figure 3.6.xlsx	Folder name: Figure 3.6 This folder includes data for Figure 3.6 for energy calculation verification
shear_test.dat	Folder name: Figure 3.9 Sub folder: Figure 3.9 a This folder includes codes for developing fault models. Data for creating models and generating different parts of Figure 3.9a are included. The txt files show data extracted from UDEC sav files for ESS distribution. The file named "shear_test" should be called for starting simulation. The sav file "ESS" gives the model right before slip initiation.
Setup.dat	Folder name: Figure 3.9 Sub folder: Figure 3.9 a The dat file "Setup" will be automatically called when the user calls "shear_test.dat". This dat file defines the input parameters for the model.
_input.dat	Folder name: Figure 3.9

	<p>Sub folder: Figure 3.9 a</p> <p>The dat file “_input” will be automatically called when the user calls “shear_test.dat”. This dat file provides the input properties for the model, including geometrical parameters, mechanical properties, and fault friction features.</p>
_properties.dat	<p>Folder name: Figure 3.9</p> <p>Sub folder: Figure 3.9 a</p> <p>The dat file "_properties" will be automatically called when the user calls “shear_test.dat”. This dat file provides the input geometrical parameters.</p>
_initial.dat	<p>Folder name: Figure 3.9</p> <p>Sub folder: Figure 3.9 a</p> <p>The dat file "_initial" will be automatically called when the user calls “shear_test.dat”. This dat file builds the initial geometry of the model.</p>
_history.dat	<p>Folder name: Figure 3.9</p> <p>Sub folder: Figure 3.9 a</p> <p>The dat file "_history" will be automatically called when the user calls “shear_test.dat”. This dat file records history for model-defined parameters.</p>
_Lateral_loading.dat	<p>Folder name: Figure 3.9</p> <p>Sub folder: Figure 3.9 a</p> <p>The dat file "_Lateral_loading" will be automatically called when the user calls “shear_test.dat”. This dat file provides the shear stress on the fault.</p>
_Normal_loading.dat	<p>Folder name: Figure 3.9</p> <p>Sub folder: Figure 3.9 a</p> <p>The dat file "_Normal_loading" will be automatically called when the user calls “shear_test.dat”. This dat file provides the normal stress on the fault.</p>
ESS_plotter.dat	<p>Folder name: Figure 3.9</p> <p>Sub folder: Figure 3.9 a</p> <p>The dat file "ESS_plotter" should be called after the simulation. This dat file provides the data for plotting ESS along the fault</p>
shear_test.dat	<p>Folder name: Figure 3.9</p> <p>Sub folder: Figure 3.9 b</p> <p>This folder includes codes for developing the fault model. Data for creating models and generating different parts of Figure 3.9b are included. The txt files show data extracted from UDEC sav files for Slip distribution. The dat file named "shear_test" should be called for starting the simulation. The sav file “Arrested Rupture” gives result of running the simulation until rupture is terminated.</p>
Setup.dat	<p>Folder name: Figure 3.9</p>

	<p>Sub folder: Figure 3.9 b</p> <p>The dat file "Setup" will be automatically called when the user calls "shear_test.dat". This dat file defines the input parameters for the model.</p>
_input.dat	<p>Folder name: Figure 3.9</p> <p>Sub folder: Figure 3.9b</p> <p>The dat file "_input" will be automatically called when the user calls "shear_test.dat". This dat file provides the input properties for the model, including geometrical parameters, mechanical properties, and fault friction features.</p>
_properties.dat	<p>Folder name: Figure 3.9</p> <p>Sub folder: Figure 3.9 b</p> <p>The dat file "_properties" will be automatically called when the user calls "shear_test.dat". This dat file provides the input geometrical parameters.</p>
_initial.dat	<p>Folder name: Figure 3.9</p> <p>Sub folder: Figure 3.9 b</p> <p>The dat file "_initial" will be automatically called when the user calls "shear_test.dat". This dat file builds the initial geometry of the model.</p>
_history.dat	<p>Folder name: Figure 3.9</p> <p>Sub folder: Figure 3.9 b</p> <p>The dat file "_history" will be automatically called when the user calls "shear_test.dat". This dat file records history for model-defined parameters.</p>
_Lateral_loading.dat	<p>Folder name: Figure 3.9</p> <p>Sub folder: Figure 3.9 b</p> <p>The dat file "_Lateral_loading" will be automatically called when the user calls "shear_test.dat". This dat file provides the shear stress on the fault.</p>
_Normal_loading.dat	<p>Folder name: Figure 3.9</p> <p>Sub folder: Figure 3.9 b</p> <p>The dat file "_Normal_loading" will be automatically called when the user calls "shear_test.dat". This dat file provides the normal stress on the fault.</p>
Slip_plotter.dat	<p>Folder name: Figure 3.9</p> <p>Sub folder: Figure 3.9 b</p> <p>The dat file "Slip_plotter" should be called after the simulation. This dat file provides the data for plotting Slip along the fault</p>
Figure 3.9a and b.xlsx	<p>Folder name: Figure 3.9</p> <p>This spreadsheet provides data for Figure 3.9 parts a and b</p>

Figure 3.9c and d.xlsx	Folder name: Figure 3.9. This spreadsheet provides data for Figure 3.9 parts c and d
------------------------	---

APPENDIX C

EQUATIONS FOR MECHANICAL DAMPING IN UDEC

For implementing the local damping, velocity of gridpoint i ($\dot{u}_i^{(t+\Delta t/2)}$) at each half timestep ($\Delta t/2$) is calculated from $F_i^{(t)}$, the unbalance force at gridpoint i , at the t^{th} timestep:

$$\dot{u}_i^{(t+\Delta t/2)} = \dot{u}_i^{(t-\Delta t/2)} + \left(F_i^{(t)} - \alpha \left| F_i^{(t)} \right| \text{sgn} \left(\dot{u}_i^{(t-\Delta t/2)} \right) \right) \frac{\Delta t}{m_i}, \quad (\text{C. 1})$$

where m_i is the nodal mass and α stands for the damping constant. Unbalance force includes contributions from resulting applied loads and body forces, e.g. gravity, at each gridpoint. The damped work over the t^{th} timestep at a gridpoint i is:

$$W_{Di}^t = \alpha \left| F_i^{(t)} \right| \text{sgn} \left(\dot{u}_i^{(t-\Delta t/2)} \right) \dot{u}_i^{(t-\Delta t/2)} \Delta t, \quad (\text{C. 2})$$

where function sgn yields the sign of the velocity at each gridpoint. W_{Di}^t can be also obtained as a fraction of current kinetic energy at gridpoint i over the t^{th} timestep as

$$U_{Ki}^t = \frac{1}{2} m_i \left(\dot{u}_i^{(t-\Delta t/2)} \right)^2, \quad (\text{C. 3})$$

and then W_{Di}^t is calculated as:

$$W_{Di}^t = 2\alpha \Delta t U_{Ki}^t \quad (\text{C. 4})$$

Therefore, the damped work and kinetic energy are related by the damping constant. The total damped work is a cumulative term, the sum of all gridpoints and timesteps:

$$W_D = \sum_{t=1}^{nt} \sum_{i=1}^{ngp} W_{Di}^t, \quad (\text{C. 5})$$

where nt is the number of timesteps and ngp is the number of gridpoints. Total current kinetic energy is not cumulative and is the sum of all gridpoints at each timestep as:

$$U_K^t = \sum_{i=1}^{ngp} U_{Ki}^t, \quad (\text{C. 6})$$

and finally, radiated seismic energy can be calculated at the end of a simulation as:

$$W_k = W_D + U_K^t \quad (\text{C. 7})$$

APPENDIX D

SUPPLEMENTAL ELECTRONIC FILES FOR CHAPTER 4

This appendix includes database, UDEC fish codes, and spreadsheets for modeling rupture propagation and calculation of energy components.

Data Files for Simulating Earthquake Rupture	Files containing UDEC fish codes for constructing verification problems and simulating rupture propagation and arrest.
Energy_verification; Figure 2.xlsx	Folder name: Figure 2 Fish codes for modeling the direct shear tests with $D_c=0$, $D_c=\text{inf}$, and $D_c=0.45$ mm are included here. The procedure for driving GRCs are also included. "Shear test Results-Dc0.45mm.sav" represents results for the test with $D_c=0.45$ mm; "Shear test Results-Dc0mm.sav" represents results for the test with $D_c=0$; The data file named "shear_test" should be called for starting the simulation.
ESS_Driver.dat	Folder name: Figure 4 This folder includes codes for developing the fault model. Data for creating models and generating different parts of Figure 4.4 are included. The txt files show data extracted from UDEC sav files for ESS distribution. The dat file named "shear_test" should be called for starting the simulation. The sav file "_ESS" gives the fault model right before the slip initiation.
Setup.dat	Folder name: Figure 4 The dat file "Setup" will be automatically called when the user calls "shear_test.dat". This dat file defines the input parameters for the model.
_input.dat	Folder name: Figure 4 The dat file "_input" will be automatically called when the user calls "shear_test.dat". This dat file provides the input properties for the model, including geometrical parameters, mechanical properties, and fault friction features.
_properties.dat	Folder name: Figure 4 The dat file "_properties" will be automatically called when the user calls "shear_test.dat". This dat file provides the input geometrical parameters.
_initial.dat	Folder name: Figure 4 The dat file "_initial" will be automatically called when the user calls "shear_test.dat". This dat file builds the initial geometry of the model.
_history.dat	Folder name: Figure 4 The dat file "_history" will be automatically called when the user calls "shear_test.dat". This dat file records history for model-defined parameters.

_Lateral_loading.dat	Folder name: Figure 4 The dat file "_Lateral_loading" will be automatically called when the user calls "shear_test.dat". This dat file provides the shear stress on the fault.
_Normal_loading.dat	Folder name: Figure 4 The dat file "_Normal_loading" will be automatically called when the user calls "shear_test.dat". This dat file provides the normal stress on the fault.
Slip_Driver.dat	Folder name: Figure 4 The dat file named " Slip_Driver " should be called after calling "ESS_Driver.dat" for restoring the sav file "_ESS" and running the simulation until rupture is arrested. The sav file "_Slip" will be generated that gives the fault model after rupture arrest.
Slip Plotter.dat	Folder name: Figure 4 The dat file " Slip Plotter" should be called after the simulation. This dat file provides the data for plotting slip along the fault
ESS Plotter.dat	Folder name: Figure 4 The dat file " Slip Plotter" should be called after the simulation. This dat file provides the data for plotting ESS along the fault
Model Calibration; Figure 4 .xlsx	Folder name: Figure 4 This folder includes codes for developing the fault model; "_ESS.sav" represents results for the test with Dc=0; txt files show data extracted from UDEC sav file for ESS and slip distributions ; the dat file named "shear_test" should be called for starting the simulation.
Matlab Codes.txt	Folder name: Figure 5 Matlab file shows the final plot for Figure 4.5. "Matlab Codes.txt" shows the codes for Matlab plotting.
Exporting slip and radiated energy from UDEC.dat	Folder name: Figure 5 The dat file "Exporting slip and radiated energy from UDEC" includes codes for plotting slip and radiated energy over time. This dat file should be called after restoring the sav file "UDEC output.sav"
Sensitivity analyses on damping constant .dat	Folder name: Figure 6 This includes codes for the parametric study on damping constant; With changing damping constant , this part analyzes effects of damping on stability of rupture; dat file "Sensitivity analyses on damping constant" automatically produces different cases; damping constant from 0 to 100%. The UDEC output will be generated as .sav files for each case. For example, after calling the dat file "Sensitivity analyses on damping constant", "_resi_Damp10.sav" will represent results for the test with damping constant=10%;
Rupture and energy plotter.dat	After generating sav files, the dat file "Rupture and energy plotter" should be called to generate the txt files containing data on the rupture propagation and energy radiation over time on the fault.

Damping_Figure 6.xlsx	Folder name: Figure 6 This includes data extracted from UDEC sav files for Figure 4.6.
Sensitivity analyses on Dc.dat	Folder name: Figure 7 This dat file includes codes for the parametric study on characteristic distances with changing Dc of the slip-weakening behavior. This part analyzes effects of Dc on stability of rupture; dat file "Sensitivity analyses on Dc" automatically produces different cases with 8 to 23mm Dc. The UDEC output will be generated as .sav files for each case. For example, "_8mm.sav" represents results for the test with Dc=8 mm;
stress-slip plotter.dat	This dat files extracts data from UDEC sav files for plotting stress-slip curves
Rupture plotter.dat	This dat files extracts data from UDEC sav files for plotting rupture length and average slip.
Dc Parametric Study; Figure 7.xlsx	This spreadsheet shows data used for Figure 4.7
Shear_test.dat	Folder name: Figure 8 The dat file "shear_test" is for the parametric study on the loading system stiffness with changing the shear modulus of the rock; this part analyzes effects of loading system stiffness on stability of rupture for Figure 4.8. Shear modulus can be changed through changing the value in dat file named "shear_test" that should be called for each case of the parametric study. Other dat files will be automatically called and processed. The UDEC outputs are listed as .sav files for each case. For example, "_10GPa.sav" represents results for the test with G=10 GPa.
Setup.dat	Folder name: Figure 8 The dat file "Setup" will be automatically called when the user calls "shear_test.dat". This dat file defines the input parameters for the model.
_input.dat	Folder name: Figure 8 The dat file "_input" will be automatically called when the user calls "shear_test.dat". This dat file provides the input properties for the model, including geometrical parameters, mechanical properties, and fault friction features.
_properties.dat	Folder name: Figure 8 The dat file "_properties" will be automatically called when the user calls "shear_test.dat". This dat file provides the input geometrical parameters.
_initial.dat	Folder name: Figure 8 The dat file "_initial" will be automatically called when the user calls "shear_test.dat". This dat file builds the initial geometry of the model.
_history.dat	Folder name: Figure 8 The dat file "_history" will be automatically called when the user calls "shear_test.dat". This dat file records history for model-defined parameters.

_Lateral_loading.dat	<p>Folder name: Figure 8</p> <p>The dat file "_Lateral_loading" will be automatically called when the user calls "shear_test.dat". This dat file provides the shear stress on the fault.</p>
_Normal_loading.dat	<p>Folder name: Figure 8</p> <p>The dat file "_Normal_loading" will be automatically called when the user calls "shear_test.dat". This dat file provides the normal stress on the fault.</p>
Stress-Slip plotter.dat	<p>Folder name: Figure 8</p> <p>This dat files extracts data from UDEC sav files for plotting stress-slip curves</p>
Rupture plotter.dat	<p>Folder name: Figure 8</p> <p>This dat files extracts data from UDEC sav files for plotting rupture length and average slip.</p>
Rigidity Parametric Study; Figure 8.xlsx	<p>Folder name: Figure 8</p> <p>The spread sheet "Rigidity Parametric Study" provides Figure 4.8 for the parametric study on the loading system stiffness with changing the shear modulus of the rock.</p>

APPENDIX E

SUPPLEMENTAL ELECTRONIC FILES FOR CHAPTER 5

This appendix includes the database, UDEC fish codes, and spreadsheets for modeling injection-induced seismic events.

Data Files for Simulating Injection-Induced Seismicity	Files containing UDEC fish codes for constructing verification problems and simulating seismicity induced by deep wastewater disposal and geothermal reservoirs.
shear_test.dat	Folder name: Figure 5.4 Sub folder: Figure 5.4 a This folder includes codes for developing the fault model. Data for creating models and generating different parts of Figure 5.4a are included. The txt files show data extracted from UDEC sav files for ESS distribution. The dat file named "shear_test" should be called for starting the simulation. The sav file "ESS" gives the fault model right before the slip initiation.
Setup.dat	Folder name: Figure 5.4 Sub folder: Figure 5.4 a The dat file "Setup" will be automatically called when the user calls "shear_test.dat". This dat file defines the input parameters for the model.
_input.dat	Folder name: Figure 5.4 Sub folder: Figure 5.4 a The dat file "_input" will be automatically called when the user calls "shear_test.dat". This dat file provides the input properties for the model, including geometrical parameters, mechanical properties, and fault friction features.
_properties.dat	Folder name: Figure 5.4 Sub folder: Figure 5.4 a The dat file "_properties" will be automatically called when the user calls "shear_test.dat". This dat file provides the input geometrical parameters.
_initial.dat	Folder name: Figure 5.4 Sub folder: Figure 5.4 a The dat file "_initial" will be automatically called when the user calls "shear_test.dat". This dat file builds the initial geometry of the model.
_history.dat	Folder name: Figure 5.4 Sub folder: Figure 5.4 a The dat file "_history" will be automatically called when the user calls "shear_test.dat". This dat file records history for model-defined parameters.

_Lateral_loading.dat	<p>Folder name: Figure 5.4</p> <p>Sub folder: Figure 5.4 a</p> <p>The dat file "_Lateral_loading" will be automatically called when the user calls "shear_test.dat". This dat file provides the shear stress on the fault.</p>
_Normal_loading.dat	<p>Folder name: Figure 5.4</p> <p>Sub folder: Figure 5.4 a</p> <p>The dat file "_Normal_loading" will be automatically called when the user calls "shear_test.dat". This dat file provides the normal stress on the fault.</p>
ESS_plotter.dat	<p>Folder name: Figure 5.4</p> <p>Sub folder: Figure 5.4 a</p> <p>The dat file "ESS_plotter" should be called after the simulation. This dat file provides the data for plotting ESS along the fault</p>
shear_test.dat	<p>Folder name: Figure 5.4</p> <p>Sub folder: Figure 5.4 b</p> <p>This folder includes codes for developing the fault model. Data for creating models and generating different parts of Figure 5.4b are included. The txt files show data extracted from UDEC sav files for Slip distribution. The dat file named "shear_test" should be called for starting the simulation. The sav file "Arrested Rupture" gives result of running the simulation until rupture is terminated.</p>
Setup.dat	<p>Folder name: Figure 5.4</p> <p>Sub folder: Figure 5.4 b</p> <p>The dat file "Setup" will be automatically called when the user calls "shear_test.dat". This dat file defines the input parameters for the model.</p>
_input.dat	<p>Folder name: Figure 5.4</p> <p>Sub folder: Figure 5.4 b</p> <p>The dat file "_input" will be automatically called when the user calls "shear_test.dat". This dat file provides the input properties for the model, including geometrical parameters, mechanical properties, and fault friction features.</p>
_properties.dat	<p>Folder name: Figure 5.4</p> <p>Sub folder: Figure 5.4 b</p> <p>The dat file "_properties" will be automatically called when the user calls "shear_test.dat". This dat file provides the input geometrical parameters.</p>
_initial.dat	<p>Folder name: Figure 5.4</p> <p>Sub folder: Figure 5.4 b</p> <p>The dat file "_initial" will be automatically called when the user calls "shear_test.dat". This dat file builds the initial geometry of the model.</p>

_history.dat	Folder name: Figure 5.4 Sub folder: Figure 5.4 b The dat file "_history" will be automatically called when the user calls "shear_test.dat". This dat file records history for model-defined parameters.
_Lateral_loading.dat	Folder name: Figure 5.4 Sub folder: Figure 5.4 b The dat file "_Lateral_loading" will be automatically called when the user calls "shear_test.dat". This dat file provides the shear stress on the fault.
_Normal_loading.dat	Folder name: Figure 5.4 Sub folder: Figure 5.4 b The dat file "_Normal_loading" will be automatically called when the user calls "shear_test.dat". This dat file provides the normal stress on the fault.
Slip_plotter.dat	Folder name: Figure 5.4 Sub folder: Figure 5.4 b The dat file "Slip_plotter" should be called after the simulation. This dat file provides the data for plotting Slip along the fault
Figure 5.4a and b.xlsx	Folder name: Figure 5.4 This spreadsheet provides data for Figure 5.4 parts a and b
shear_test.dat	Folder name: Figure 5.5 This folder includes codes for developing the fault model. Data for creating models and generating different parts of Figure 5.5 are included. The txt files show data extracted from UDEC sav files for stress- slip curve. The dat file named "shear_test" should be called for starting the simulation. The sav file "Arrested Rupture" gives result of running the simulation until rupture is terminated.
Setup.dat	Folder name: Figure 5.5 The dat file "Setup" will be automatically called when the user calls "shear_test.dat". This dat file defines the input parameters for the model.
_input.dat	Folder name: Figure 5.5 The dat file "_input" will be automatically called when the user calls "shear_test.dat". This dat file provides the input properties for the model, including geometrical parameters, mechanical properties, and fault friction features.
_properties.dat	Folder name: Figure 5.5 The dat file "_properties" will be automatically called when the user calls "shear_test.dat". This dat file provides the input geometrical parameters.
_initial.dat	Folder name: Figure 5.5

	The dat file "_initial" will be automatically called when the user calls "shear_test.dat". This dat file builds the initial geometry of the model.
_history.dat	Folder name: Figure 5.5 The dat file "_history" will be automatically called when the user calls "shear_test.dat". This dat file records history for model-defined parameters.
_Lateral_loading.dat	Folder name: Figure 5.5 The dat file "_Lateral_loading" will be automatically called when the user calls "shear_test.dat". This dat file provides the shear stress on the fault.
_Normal_loading.dat	Folder name: Figure 5.5 The dat file "_Normal_loading" will be automatically called when the user calls "shear_test.dat". This dat file provides the normal stress on the fault.
stress-slip plotter.dat	Folder name: Figure 5.5 The dat file "stress-slip plotter" should be called after the simulation. This dat file provides the data for plotting stress-slip curve of the fault. The txt file named "_shear_stress_vs_slip" is the result and gives data needed for the spreadsheet named "figure 5.5".
Figure 5.5.xlsx	Folder name: Figure 5.5 This spreadsheet provides data for Figure 5.5
shear_test.dat	Folder name: Figure 5.6 and 5.7 Codes for running 150-, 15-, and 5-increment patterns of injection onto well-oriented faults are included in this folder. The dat file named "Shear_test" generates output for each case. The following sav file will be generated: "_well_5_inc" and "_well_15_inc" and "_well_150_inc". "well" stands for well-oriented fault and "inc" indicates the number of increments.
Setup.dat	Folder name: Figure 5.6 and 5.7 The dat file "Setup" will be automatically called when the user calls "shear_test.dat". This dat file defines the input parameters for the model.
_input.dat	Folder name: Figure 5.6 and 5.7 The dat file "_input" will be automatically called when the user calls "shear_test.dat". This dat file provides the input properties for the model, including geometrical parameters, mechanical properties, and fault friction features.
_properties.dat	Folder name: Figure 5.6 and 5.7 The dat file "_properties" will be automatically called when the user calls "shear_test.dat". This dat file provides the input geometrical parameters.
_initial.dat	Folder name: Figure 5.6 and 5.7 The dat file "_initial" will be automatically called when the user calls "shear_test.dat".

	This dat file builds the initial geometry of the model.
_history.dat	Folder name: Figure 5.6 and 5.7 The dat file "_history" will be automatically called when the user calls "shear_test.dat". This dat file records history for model-defined parameters.
_Lateral_loading.dat	Folder name: Figure 5.6 and 5.7 The dat file "_Lateral_loading" will be automatically called when the user calls "shear_test.dat". This dat file provides the shear stress on the fault.
_Normal_loading.dat	Folder name: Figure 5.6 and 5.7 The dat file "_Normal_loading" will be automatically called when the user calls "shear_test.dat". This dat file provides the normal stress on the fault.
stress-pressure plotter.dat	Folder name: Figure 5.6 and 5.7 The dat file "stress-slip plotter" should be called after each simulation. This dat file provides the data for plotting stress-slip and energy-pressure curves of the fault. The txt files like "_shear_stress_vs_slip_5increments" and "_seismic_vs_pressure_5increments". These txt files give data needed for figures 5.6 and 5.7, respectively. The former is the shear stress vs slip on the fault while the latter is the seismic energy radiated while the injection pressure increases continuously based on the number of increments.
Rupture plotter.dat	Folder name: Figure 5.6 and 5.7 The dat file "Rupture plotter" should be called after each simulation. This dat file provides the data for plotting slip along the fault generating txt file like "_Slip_15increments" which is the slip distribution for the 15-increment scenario.
Figure 5.6 and 5.7.xlsx	Folder name: Figure 5.6 and 5.7 Results of simulating 150-, 15-, and 5-increment patterns of injection onto well-oriented faults are included in this spreadsheet for Figures 5.6 and 5.7.
shear_test.dat	Folder name: Figure 5.8 and 5.9 Codes for running 150-, 15-, and 5-increment patterns of injection onto well-oriented faults are included in this folder. The dat file named "Shear_test" generates output for each case. The following sav file will be generated: "_miss_5_inc" and "_miss_15_inc" and "_miss_150_inc". "miss" stands for misoriented fault and "inc" indicates the number of increments.
Setup.dat	Folder name: Figure 5.8 and 5.9 The dat file "Setup" will be automatically called when the user calls "shear_test.dat". This dat file defines the input parameters for the model.
_input.dat	Folder name: Figure 5.8 and 5.9 The dat file "_input" will be automatically called when the user calls "shear_test.dat". This dat file provides the input properties for the model, including geometrical parameters, mechanical properties, and fault friction features.

_properties.dat	Folder name: Figure 5.8 and 5.9 The dat file "_properties" will be automatically called when the user calls "shear_test.dat". This dat file provides the input geometrical parameters.
_initial.dat	Folder name: Figure 5.8 and 5.9 The dat file "_initial" will be automatically called when the user calls "shear_test.dat". This dat file builds the initial geometry of the model.
_history.dat	Folder name: Figure 5.8 and 5.9 The dat file "_history" will be automatically called when the user calls "shear_test.dat". This dat file records history for model-defined parameters.
_Lateral_loading.dat	Folder name: Figure 5.8 and 5.9 The dat file "_Lateral_loading" will be automatically called when the user calls "shear_test.dat". This dat file provides the shear stress on the fault.
_Normal_loading.dat	Folder name: Figure 5.8 and 5.9 The dat file "_Normal_loading" will be automatically called when the user calls "shear_test.dat". This dat file provides the normal stress on the fault.
stress-pressure plotter.dat	Folder name: Figure 5.8 and 5.9 The dat file "stress-slip plotter" should be called after each simulation. This dat file provides the data for plotting stress-slip and energy-pressure curves of the fault. The txt files like "_shear_stress_vs_slip_5increments" and "_seismic_vs_pressure_5increments". These txt files give data needed for figures 5.6 and 5.7, respectively. The former is the shear stress vs slip on the fault while the latter is the seismic energy radiated while the injection pressure increases continuously based on the number of increments.
Rupture plotter.dat	Folder name: Figure 5.8 and 5.9 The dat file "Rupture plotter" should be called after each simulation. This dat file provides the data for plotting slip along the fault generating txt file like "_slip for 5 increments.txt" which is the slip distribution for the 5 increment scenario.
Figure 5.8 and 5.9.xlsx	Folder name: Figure 5.8 and 5.9 Results of simulating 150-, 15-, and 5-increment patterns of injection onto misoriented faults are included in this spreadsheet for Figures 5.8 and 5.9.
Figure 5.10 and 5.11.xlsx	Folder name: Figure 5.10 and 5.11 This folder contains the spreadsheet plotting Figures 5.10 and 5.11.

APPENDIX F

PUBLISHER COPYRIGHT PERMISSION FOR CHAPTER 5

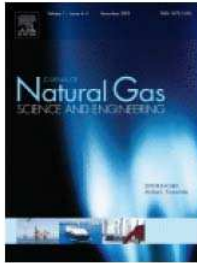
3/23/2018

Rightslink® by Copyright Clearance Center



RightsLink®

Home Create Account Help



Title: Modeling injection-induced seismicity through calculation of radiated seismic energy
Author: Zoheir Khademian, Masami Nakagawa, Ugur Ozbay
Publication: Journal of Natural Gas Science and Engineering
Publisher: Elsevier
Date: April 2018
Published by Elsevier B.V.

LOGIN
If you're a copyright.com user, you can login to RightsLink using your copyright.com credentials. Already a [RightsLink](#) user or want to [learn more?](#)

Please note that, as the author of this Elsevier article, you retain the right to include it in a thesis or dissertation, provided it is not published commercially. Permission is not required, but please ensure that you reference the journal as the original source. For more information on this and on your other retained rights, please visit: <https://www.elsevier.com/about/our-business/policies/copyright#Author-rights>

<https://www.elsevier.com/about/our-business/policies/copyright#Author-rights>

BACK

CLOSE WINDOW

Copyright © 2018 Copyright Clearance Center, Inc. All Rights Reserved. [Privacy statement](#). [Terms and Conditions](#). Comments? We would like to hear from you. E-mail us at customer@copyright.com